Plasma Physics Reports, Vol. 29, No. 9, 2003, pp. 727–739. From Fizika Plazmy, Vol. 29, No. 9, 2003, pp. 787–800.

STELLARATORS

Compact Torsatron with Improved α-Particle Confinement[1]

M. Yu. Isaev*, S. E. Grebenshchikov, S. V. Shchepetov**, J. Nührenberg***, and W. A. Cooper******

** Nuclear Fusion Institute, Russian Research Centre Kurchatov Institute, Moscow, Russia*

*** General Physics Institute of the Russian Academy of Sciences, Moscow, Russia*

**** Max-Planck-Institut für Plasmaphysik, Greifswald, FRG*

***** Centre de Recherches en Physique des Plasmas, EPFL, Lausanne, Switzerland*

Received December 26, 2002

Abstract—The compact conventional six-period torsatron L-V with an aspect ratio of $A = 3$ has been considered as a starting point for further computational optimization of the collisionless confinement of the guiding center orbits of fusion α particles. The configurations obtained possess improved neoclassical transport together with an equilibrium β limit at a level of $\langle\beta\rangle \approx 10\%$. The optimization of magnetohydrodynamic (MHD) stability and the coil design are underway. © *2003 MAIK "Nauka/Interperiodica".*

1. INTRODUCTION

In recent years, significant experimental results have been obtained using stellarators and in many cases a good understanding of their physical grounds has been reached. Nevertheless, experimental studies with sufficient heating power are necessary to verify a variety of physical concepts. In this connection, the search for an experimental device that will combine experimental flexibility and easy access to the plasma is of current interest. A design for building such a device has been developed at the Institute of General Physics (Moscow) [1] and named L-V. This configuration is a small (major radius ~1.1 m), compact (aspect ratio of helical winding ~2.5) conventional torsatron with $L = 2$, $N = 6$, where L and N are the multipolarity and the total number of helical magnetic field periods, respectively. Four pairs of axisymmetric compensating coils make it possible to produce a broad variety of vacuum magnetic configurations with different magnetic-surface shapes. Additional compensating helical windings allow the possibility of controlling the value of the magnetic field helical ripples.

The choice of the structure of the magnetic field strength, i.e., the functional form of the field strength B in magnetic coordinates, is the essential issue in determining the physical properties of a stellarator [2]. Good collisionless confinement is obtained for helical symmetry in B, i.e., quasi-helical symmetry [3] in toroidal configurations. The HSX device is based on this type of symmetry [4]. A second type of quasi-symmetry, quasi-axisymmetry [5], constitutes the basis of new stellarator projects NCSX [6, 7] and CHS-qa [8].

The third type of symmetry, poloidal symmetry, cannot be met in toroidally closed stellarator configurations, in particular, in a linear approximation with respect to the distance from the magnetic axis. As was shown during the Wendelstein 7-X optimization (see, e.g., [9]) and more rigorously formulated in [10], the improvement of collisionless particle confinement in systems attempting a nearly equivalent substitute for this quasi-symmetry can be achieved by optimizing the contours of the second adiabatic invariant

$$J(s,\theta) = \int v_{\parallel} dl = \sqrt{2\mu/m}\frac{I_p F_t' + I_t F_p'}{F_t'}\int\sqrt{\frac{B_{ref} - B}{B^2}}d\phi \quad (1)$$

to be constant on magnetic surfaces,

$$J(s,\theta) = J(s) \quad (2)$$

for deeply to moderately deeply trapped particles in configurations with a truly 3D structure of B (where B_{ref} is the normalized magnetic field strength at the reflection point). Because of the proximity of the particle drift motion to isodynamicity [11], this condition is called quasi-isodynamicity. Here s, θ, and ϕ are the magnetic coordinates; μ is the magnetic moment of a particle with mass m; and F_t, F_p, I_t, and I_p are toroidal and poloidal magnetic and current flux functions, respectively. As was demonstrated in [12], it is possible to extend the condition of quasi-isodynamicity to all reflected particles. Thus quasi-isodynamicity is a special case of quasi-omnigeneity (see e.g., [13], [14]) that corresponds to poloidal quasi-symmetry.

In a previous paper [15], it was shown that a quasi-omnigenous magnetic-field structure can be achieved also by the optimization of a conventional LHD-like ten-period heliotron/torsatron configuration with an

[1] This article was submitted by the authors in English.

1063-780X/03/2909-0727$24.00 © 2003 MAIK "Nauka/Interperiodica"

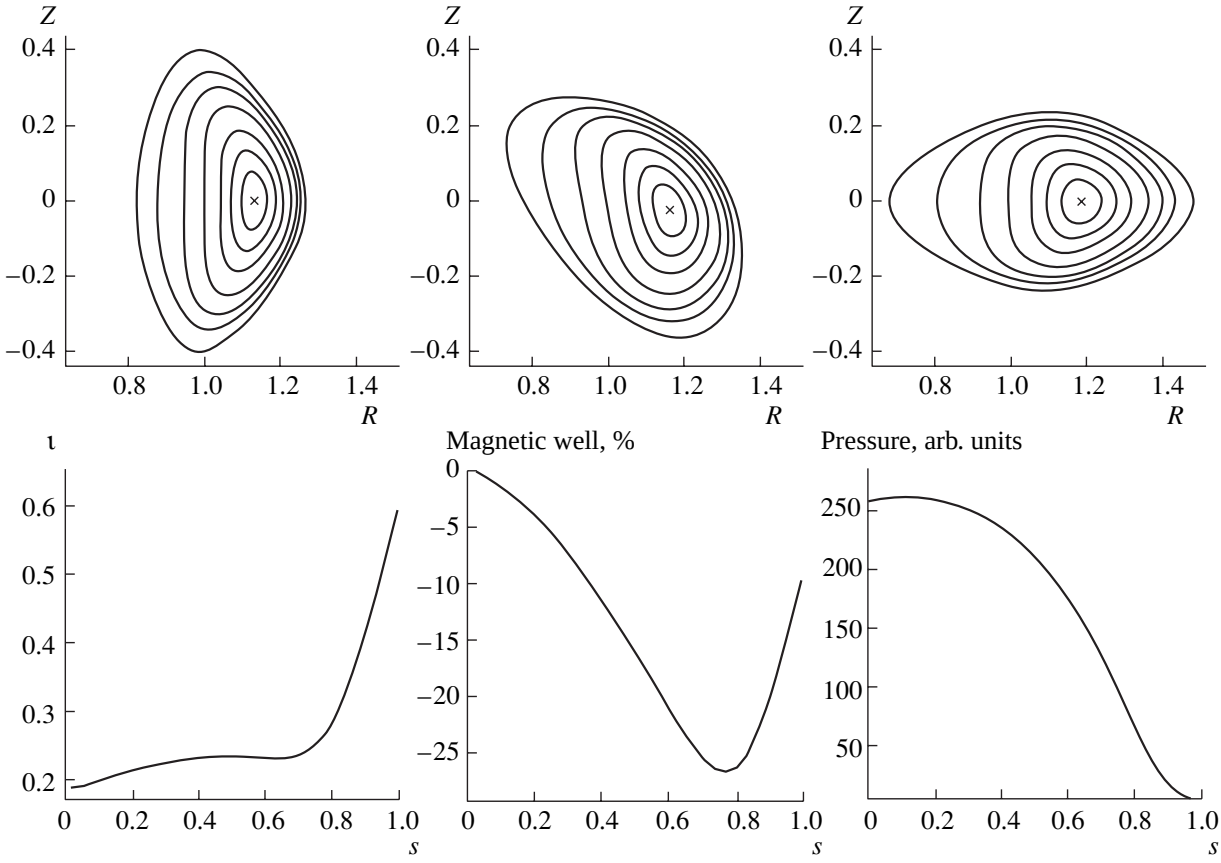

Fig. 1. Equilibrium profiles of the rotational transform, magnetic well, and plasma pressure and a view of the plasma surface cross sections at the beginning, at one-quarter, and in the middle of a field period in the L-V-TQ conventional heliotron/torsatron obtained with the equilibrium code VMEC, $\langle\beta\rangle = 2.38\%$.

inward shifted axis and an aspect ratio of $A = 6.5$ with the use of condition (2) expressed in a simple form

$$\sum_i \int \left(\frac{\partial J(i\Delta s, \theta)}{\partial \theta}\right)^2 d\theta, \qquad (3)$$

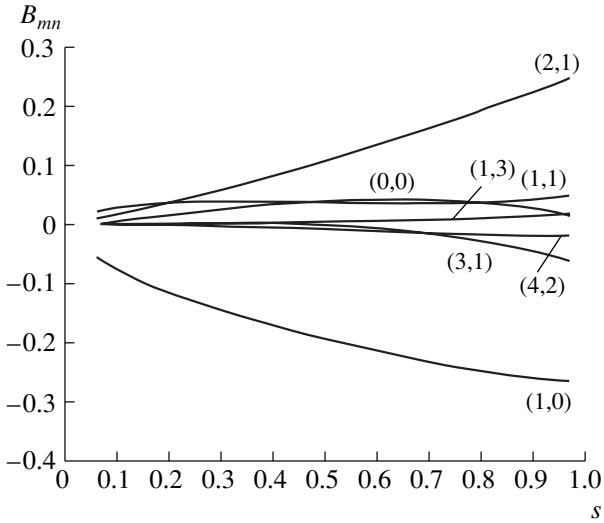

Fig. 2. Main components of the magnetic field strength spectrum in the L-V-TQ conventional heliotron/torsatron, $\langle\beta\rangle = 0.15\%$. Normalization: $B_{0,0}(0) = 1.00$.

where Δs is the spacing of the normalized-flux grid and i is the surface index, which becomes zero for deeply to moderately deeply trapped particles. For the $N = 10$ quasi-omnigenous configuration obtained, there are almost no lost α particles during the 0.05 s of their collisionless-flight time.

In the present paper, we perform the same optimization procedure for the compact $A = 3.3$ six-period stellarator L-V.

The paper is organized as follows. Section 2 describes the numerical tools used in the optimization. Section 3 presents the properties of the starting cases L-V-TQ and L-V-TUD. Section 4 shows the results of the optimization procedure, which yield two configurations, L-V-MI10 and L-V-MI14, and this is followed by a summary.

2. NUMERICAL TOOLS

3D numerical codes are an essential part of the stellarator theoretical achievements of recent years. The Wendelstein-7X stellarator [9] was designed with the help of a computational optimization package at IPP. In this work, a similar optimization package is applied.

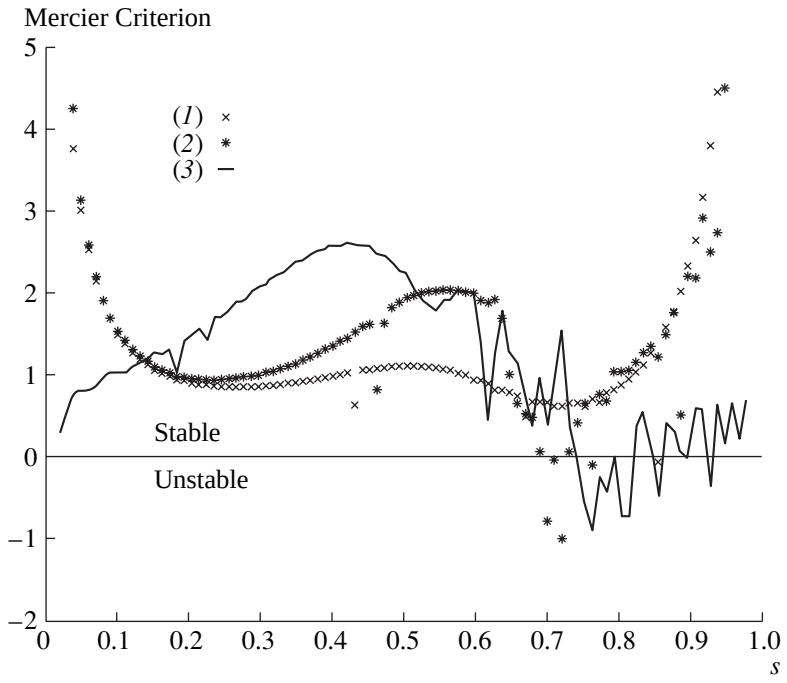

Fig. 3. TERPSICHORE calculations of the Mercier criterion in the L-V-TQ cases for ⟨β⟩ = (*1*) 1.49, (*2*) 2.31, and (*3*) 3.67%.

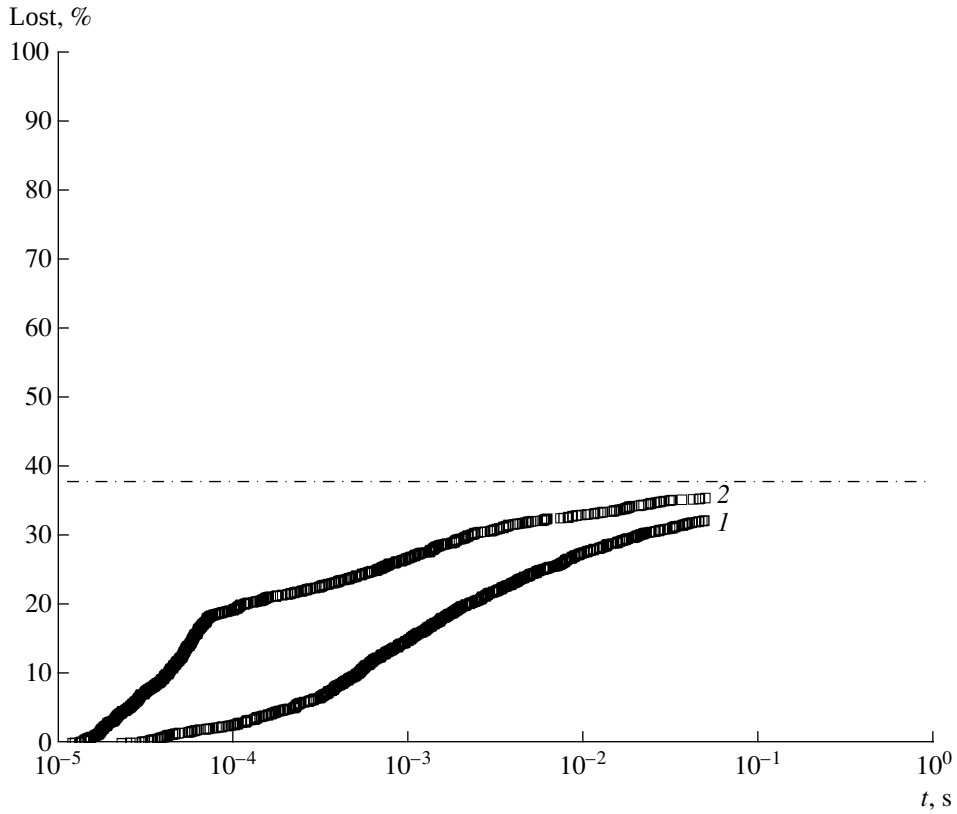

Fig. 4. Collisionless confinement of α particles in the L-V-TQ heliotron/torsatron, ⟨β⟩ = 3.8% calculated with the guiding-center orbit code MCT [20] with launching surfaces *s* = (*1*) 0.0625 and (*2*) 0.240. The dashed-and-dotted line shows the number of lost particles for surface *2*.

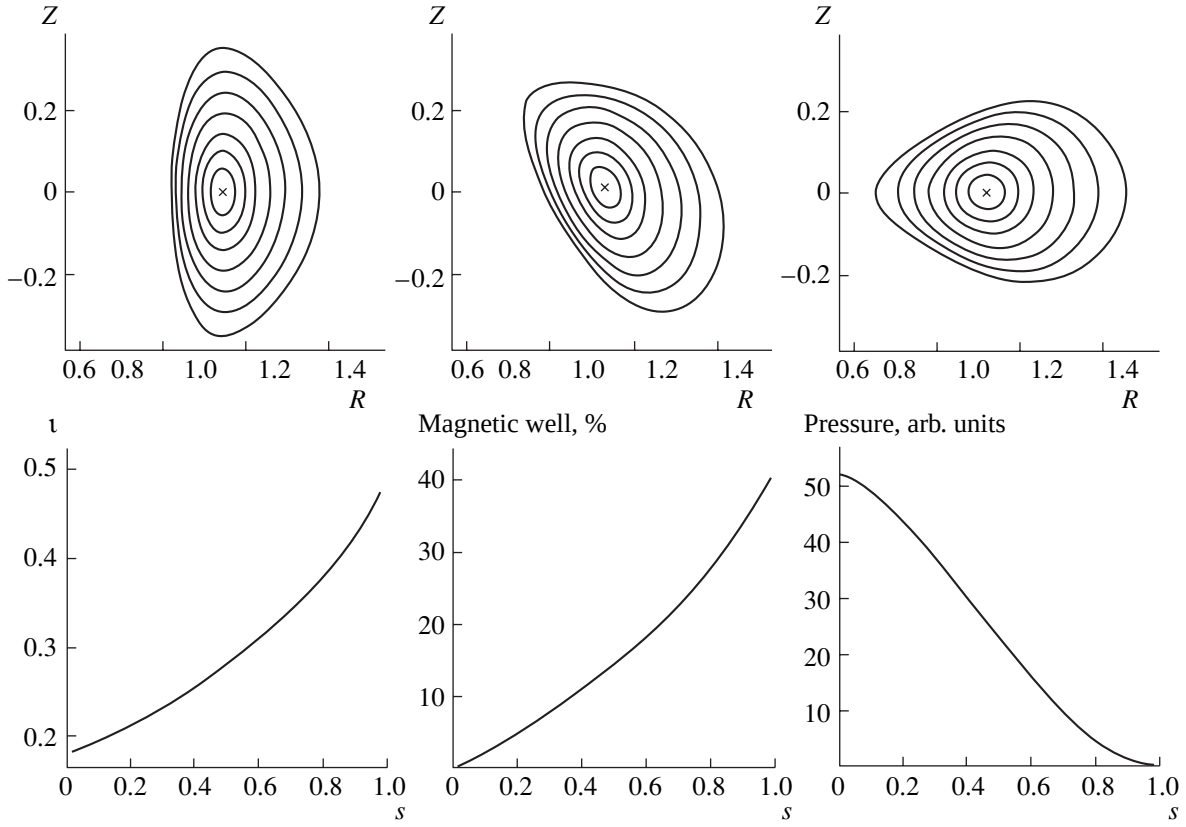

Fig. 5. Equilibrium profiles of the rotational transform, magnetic well, and plasma pressure and a view of the magnetic surface cross sections at the beginning, at one-quarter, and in the middle of a field period in the L-V-TUD configuration with $\langle\beta\rangle = 0.1\%$.

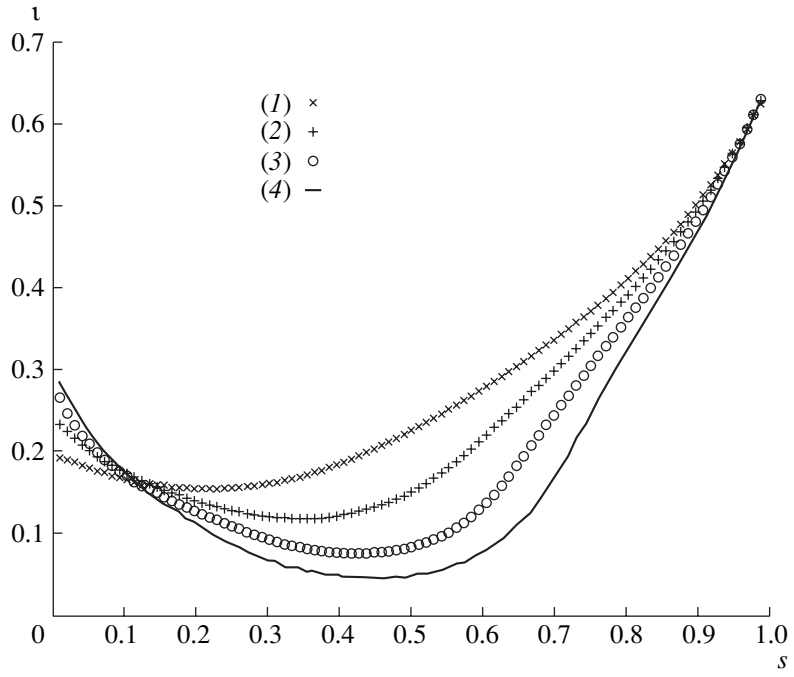

Fig. 6. VMEC equilibrium profiles of the rotational transform in L-V-TQ cases for $\langle\beta\rangle$ = (*1*) 0.46, (*2*) 0.96, (*3*) 1.49, and (*4*) 2.05%.

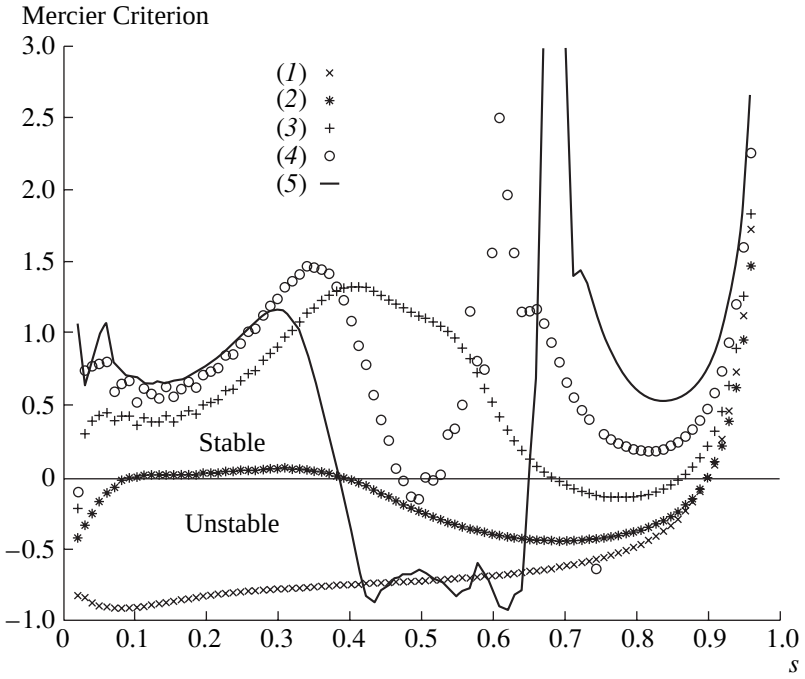

Fig. 7. TERPSICHORE calculations of the Mercier criterion in L-V-TUD cases for $\langle\beta\rangle$ = (*1*) 0.69, (*2*) 1.43, (*3*) 1.84, (*4*) 2.26, and (*5*) 2.67%.

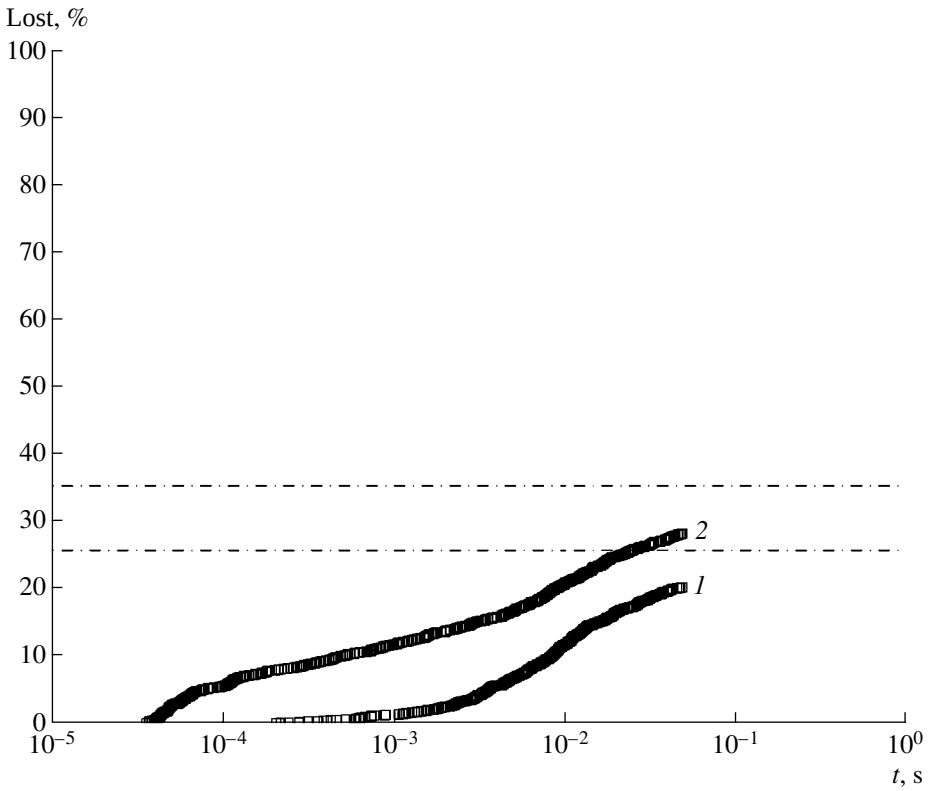

Fig. 8. Collisionless confinement of α particles in the L-V-TUD heliotron/torsatron, $\langle\beta\rangle$ = 1.4% calculated with the MCT guiding-center orbit code [20] with launching surfaces *s* = (*1*) 0.0625 and (*2*) 0.240. The lower and upper dashed-and-dotted lines show the number of lost particles for surfaces *1* and *2*, respectively.

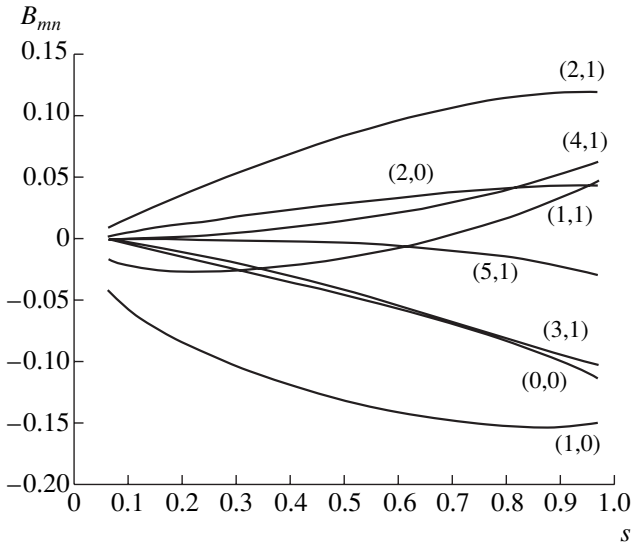

Fig. 9. Main components of the magnetic field strength spectrum in the L-V-TUD conventional heliotron/torsatron, $\langle\beta\rangle = 0.1\%$. Normalization: $B_{0,0}(0) = 1.00$.

The optimization framework is the NAG Fortran library E04UCF program [16]. This program is designed to minimize an arbitrary smooth function subject to constraints (which may include simple bounds on the variables, linear constraints and smooth nonlinear constraints) using a sequential quadratic programming method.

In the first step of our numerical calculations, we obtain the Fourier spectrum of the boundary magnetic surface from 50 magnetic field line tracing intersections with 16 toroidal cross sections using the DESCUR code [17].

For the calculation of 3D ideal MHD equilibria, the variables subject to change by the optimizer are the components R_{mn}, Z_{mn} of the plasma boundary magnetic surface defined in the cylindrical coordinates R, Z, ϕ by the relationships

$$\begin{aligned} R &= \sum R_{mn}\cos(m\vartheta - n\phi), \\ Z &= \sum Z_{mn}\sin(m\vartheta - n\phi), \end{aligned} \tag{4}$$

where ϑ is a poloidal parametrization determined to accelerate the convergence in the m-space of the Fourier series in (3) and m and n correspond to poloidal and toroidal indexes, respectively. These optimizer variables R_{mn}, Z_{mn}, together with the plasma pressure and net toroidal current profiles, are submitted as input to the equilibrium code in the IPP optimizer package : the 3D equilibrium VMEC code [18], which uses a gradient method to solve the ideal MHD inverse equilibrium equations. In this paper, we use the 5.20 version of the VMEC code, which is suitable for stellarator systems without a net toroidal current.

In these equilibrium calculations, 33 flux surfaces and 113 VMEC poloidal and toroidal Fourier components in the representation of equilibrium quantities are used.

The second code in the optimizer package, the JMC code [19], calculates the magnetic field strength B in so-called magnetic or Boozer coordinates. The maximum poloidal mode index in our runs is 9, and the maximum toroidal mode index is 8. The transformation from VMEC angular variables to magnetic coordinates is helpful because of the simplicity of the co- and contravariant magnetic field vector representations in Boozer coordinates. The Boozer magnetic field spectrum is used in almost all MHD stability and transport codes.

The third code in the optimizer package, JCONT, uses the Boozer components of the magnetic field strength to calculate the second adiabatic invariant (1) as a function of the flux surface, poloidal angle, and reflection value B_{ref}. The reflection value $B_{\mathrm{ref}} = 1.00$ was chosen to be equal to the normalized value of the magnetic field component B_{00} at the magnetic axis. The second adiabatic invariant $J(s, \theta)$ is used to calculate a so-called objective function in the optimizer, which should be minimized during the optimization.

To check the confinement properties of 3D configurations, the MCT code is used [20], which follows 1000 collisionless monoenergetic (3.5 MeV) α particle drift orbits during a typical confinement time of 0.05 s for a nominal reactor volume of 1000 m^3 and B_0 of 5 T and with a given Boozer spectrum of the magnetic field and given profiles of equilibrium flux quantities.

The optimization package is installed on the NEC-SX5 supercomputer at the Rechenzentrum Garching [21]. The NEC-SX5 is one of the top vector supercomputer machines with a peak performance on one processor near 4 gigaflops. The total computational time for one optimizer evaluation (VMEC + JMC + JCONT) is about one minute. If the plasma boundary has N mode components that can be varied, the optimizer will check the object function for all variables at each of the main steps of the minimization (no less than three), so that the total computational time of the optimization can be estimated as more than $3N$ min.

In addition to its evaluation in JMC, the Mercier stability criterion [22] is also calculated for the main L-V cases with the TERPSICHORE code [23], which reconstructs the equilibrium state in Boozer magnetic coordinates.

3. STARTING CASES

In this section, we briefly describe the coil system of the L-V device and the first results of the 3D calculation of certain properties of two basic cases of the L-V stellarator project, TQ and TUD. The use of four pairs of axisymmetric compensating coils makes it possible to produce a variety of vacuum magnetic surface shapes.

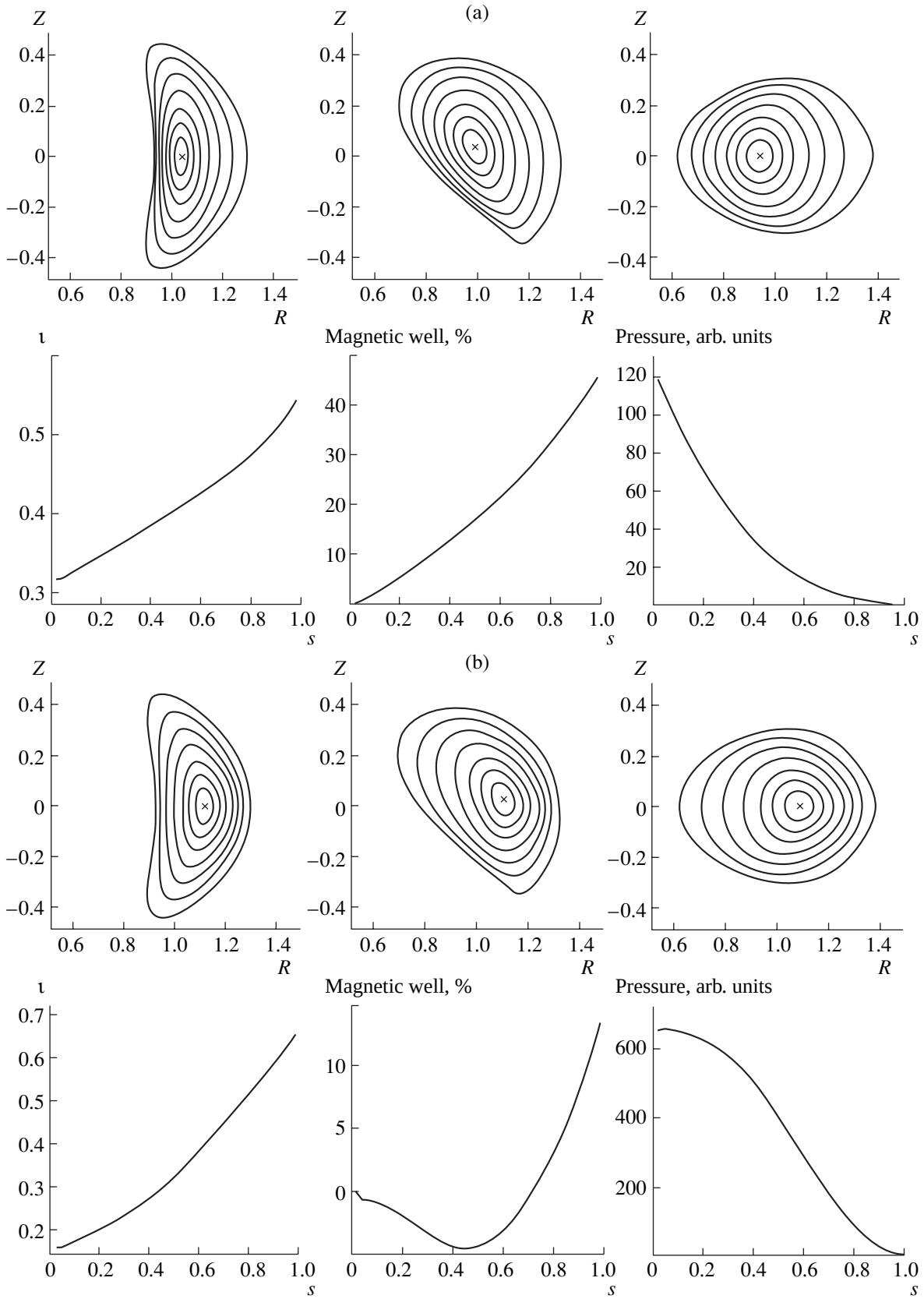

Fig. 10. Equilibrium profiles of the rotational transform, magnetic well, and plasma pressure and a view of the plasma surface cross sections at the beginning, at one-quarter, and in the middle of a field period in the L-V-MI10 configuration obtained with the VMEC equilibrium code, $\langle\beta\rangle$ = (a) 0.5 and (b) 5.6%.

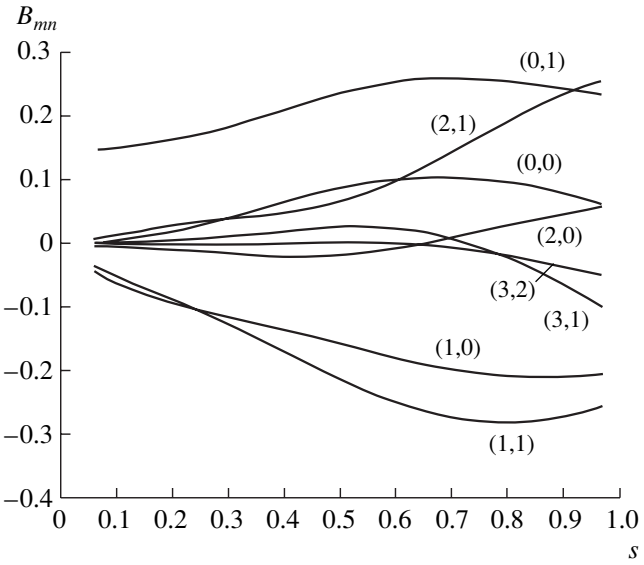

Fig. 11. Main components of the magnetic field strength spectrum in the L-V-MI10 configuration obtained, $\langle\beta\rangle$ = 0.56%. Normalization: $B_{0,0}(0) = 1.00$.

However, the simplest operation consists in the shifting of magnetic surfaces with the help of a vertical magnetic field. Shifting the magnetic surfaces outward, we obtain configurations with a deep vacuum magnetic well that is favorable for MHD stability. It is pertinent to note that in strongly outward-shifted vacuum configurations, the depth of the magnetic well may be on the order of ~15%. Shifting the magnetic configuration inwards improves neoclassical transport, but leads to the appearance of a vacuum magnetic hill. However, the average radius of the vacuum separatrix for strongly outward (inward) shifted configurations is visibly smaller than that for centered configurations due to the ergodization of the external magnetic surfaces. Therefore, two moderately shifted vacuum configurations were used for our analysis. The outward-shifted configuration (TQ) has a vacuum magnetic well. The TUD configuration obtained by shifting the magnetic surfaces inward uses an additional helical coil for ripple control.

Relevant profiles of the flux-surface quantities and the magnetic-surface cross sections computed with the VMEC code at $\beta = 2.38\%$ are shown in Fig. 1. Herein, β indicates the $\langle\beta\rangle$ value. The magnetic field spectrum in Boozer coordinates has two main components: (2,1) and (1,0) (Fig. 2). The L-V-TQ case was chosen as a case with a deepening vacuum magnetic well due to the finite-β effect, so that it is stable with respect to the Mercier criterion up to a level of $\beta = 2\%$ (Fig. 3). However, the history of collisionless α-particle loss starts

Comparison of L-V configurations

	TQ	TUD	MI10		MI14		
$\iota(0)$	0.19	0.18	0.33	0.18	0.40	0.34	0.19
$\iota(1)$	0.63	0.49	0.55	0.64	0.72	0.76	0.81
$\langle\beta\rangle$	2.4%	0.15%	0.15%	5.62%	0.15	5.5%	10.5%
Mercier stable	All S	S > 3/4	S > 3/4	No	S > 3/4	No	No
0.001s R0 = 1/4							
Lost	221	9	1	134	0	0	1
Trapped	313	264	528	451	491	422	305
0.01s R0 = 1/2							
Lost	294	85	23	102	0	0	16
Trapped	310	349	604	495	579	542	401
0.05s R0 = 1/4							
Lost	261	195	3	234	0	2	111
Trapped	313	264	524	451	491	422	305
0.05s R0 = 1/2							
Lost	302	306	59	203	5	8	155
Trapped	310	349	601	495	579	542	401
Main B_{mn}	2,1; 1,0	2,1; 1,0	0,1; 1.0; 1,1		2,1; 1,1		

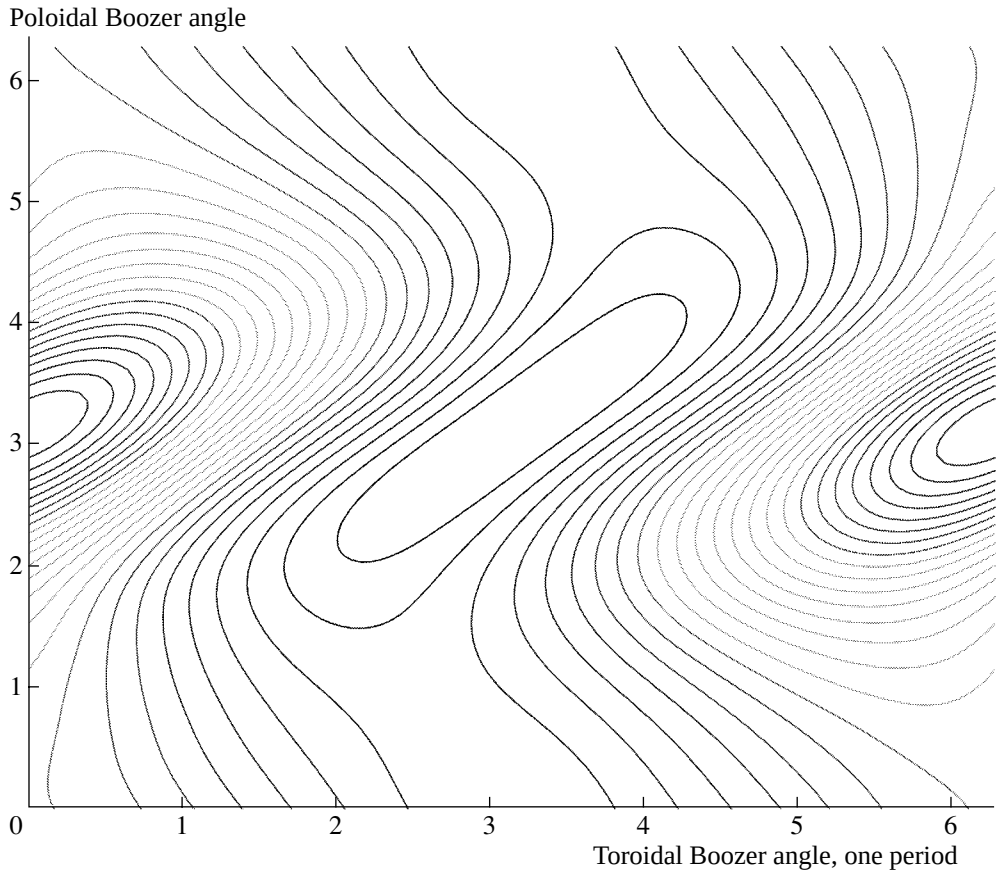

Fig. 12. Contours of the magnetic field strength at the magnetic surface $s = 8/33$ in the L-V-MI10 configuration obtained, $\beta = 0.56\%$.

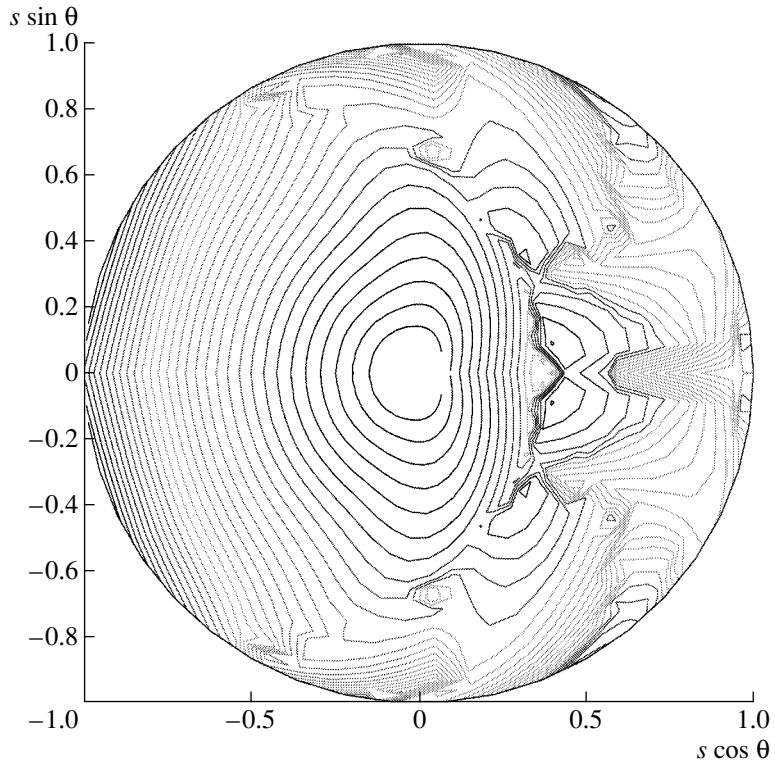

Fig. 13. Second adiabatic invariant contours for $B_{ref} = 1.00$ in the L-V-MI10 configuration obtained, $\langle\beta\rangle = 0.56\%$.

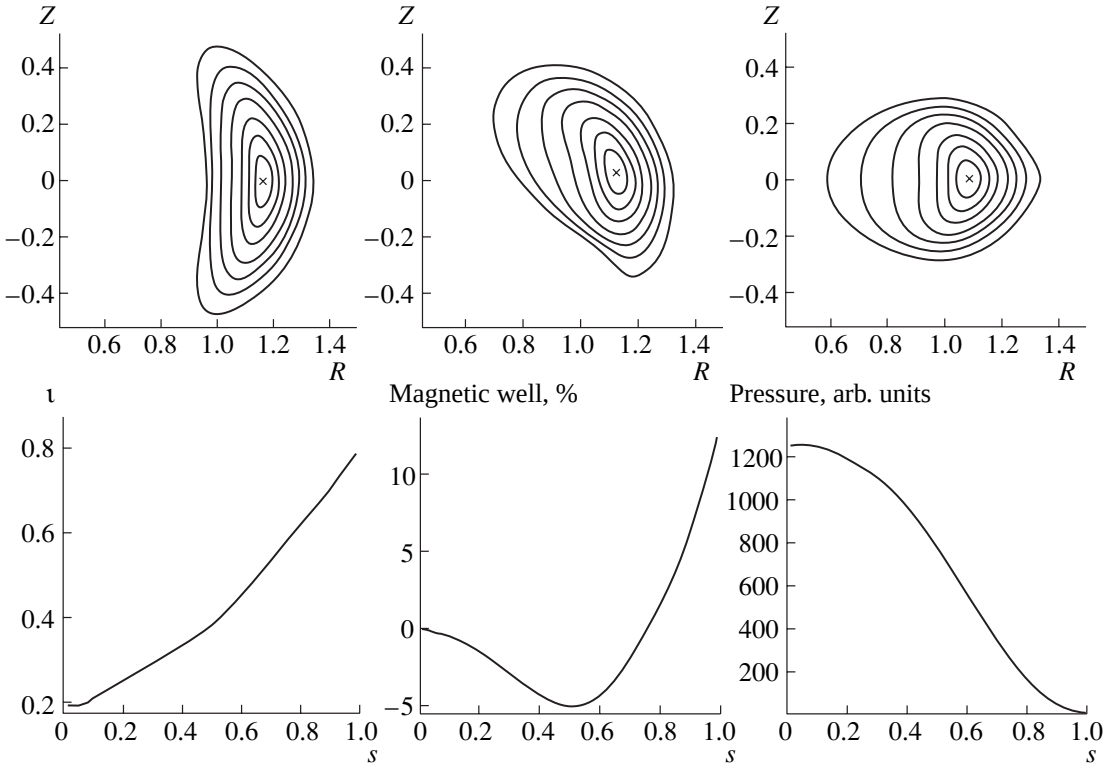

Fig. 14. Equilibrium profiles of the rotational transform, magnetic well, and plasma pressure and a view of the plasma surface cross sections at the beginning, at one-quarter, and in the middle of a field period in the L-V-MI14 configuration obtained with the equilibrium code VMEC, $\langle\beta\rangle = 10.5\%$.

already at small times of 10^{-5} s and almost all reflected particles are lost around 0.05 s (Fig. 4).

The L-V-TUD case is characterized by a vacuum magnetic hill (Fig. 5). Both L-V-TUD and L-V-TQ cases have quite a small value of the vacuum rotational transform on the axis (near 0.2). If the value of β is increased, the profile of the rotational transform develops a dangerously small value of $\iota = 0.10$ (Fig. 6). For such a small value of ι, the VMEC code demonstrates very poor convergence; this can indicate an equilibrium limit at a level of $\beta = 2$–3%. The Mercier criterion calculations for different values of β as a function of the flux label for L-V-TUD are presented in Fig. 7. For small $\beta = 0.69\%$, the case is unstable because of the vacuum magnetic hill. For larger values of $\beta = 1.43\%$ and $\beta = 1.84\%$, a small magnetic well appears near the axis and we see a stable Mercier mode region in the plasma core ($s < 0.5$). For β values greater than 2%, the L-V-TUD case is unstable around $s = 0.5$.

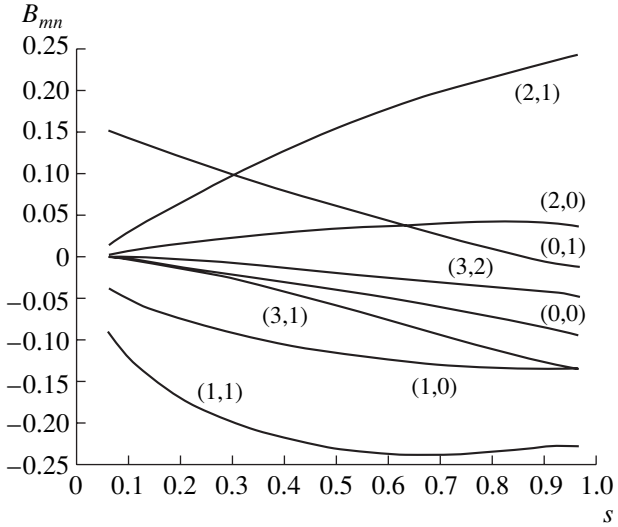

Fig. 15. Main components of the magnetic field strength spectrum in the L-V-MI14 configuration obtained, $\langle\beta\rangle = 0.56\%$. Normalization: $B_{0,0}(0) = 1.00$.

Collisionless losses in the L-V-TUD case are lower than in the L-V-TQ case (see Fig. 8). However, a large fraction of reflected α particles are still lost in 0.05 s. Figure 9 presents the main components of the magnetic field for the L-V-TUD case: $(m, n) = (0,0)$, (1,0), (1,1), (2,0), (2,1), (3,1), (4,1), and (5,1).

4. OPTIMIZATION RESULTS

The numerical optimization for the L-V stellarator is performed in several directions. The first goal is a vacuum rotational transform profile with significant shear and the ι on the axis at a level of 0.3. This can

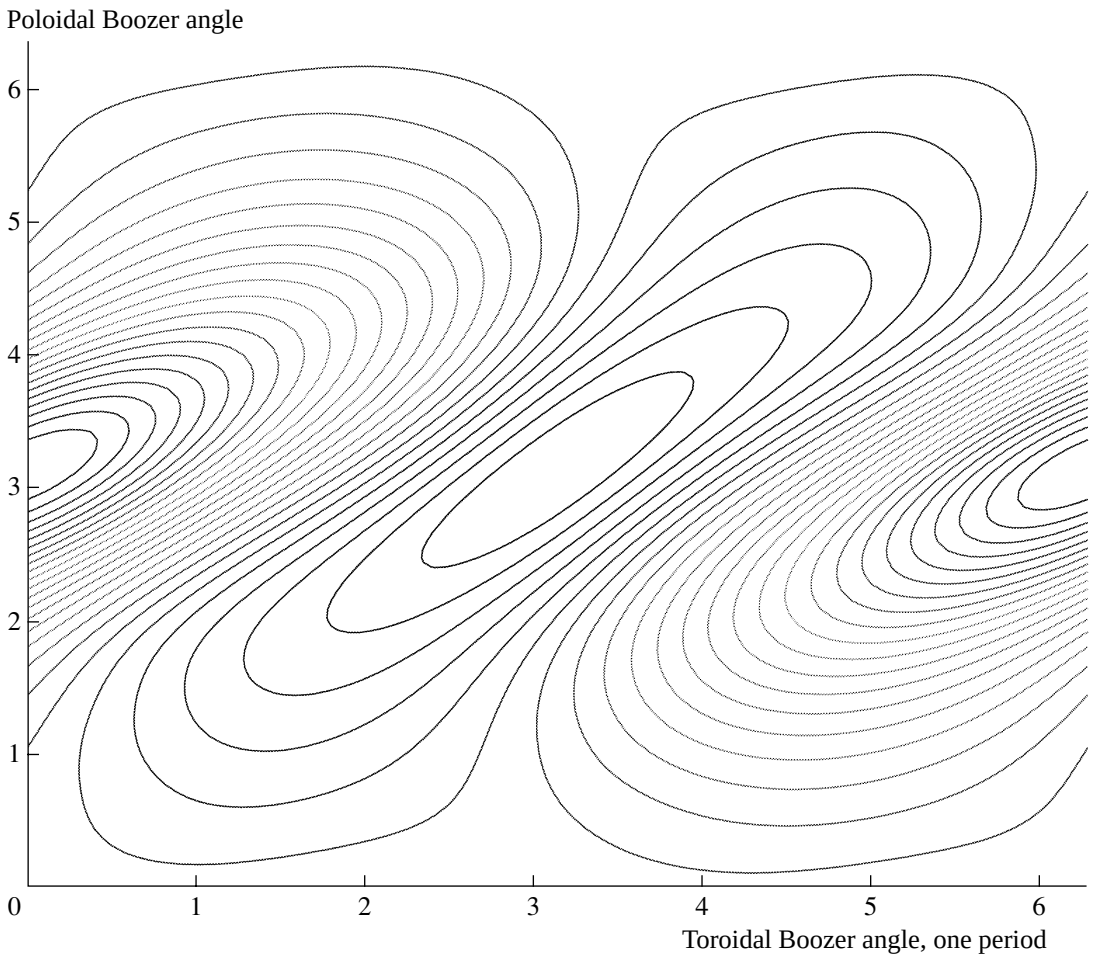

Fig. 16. Contours of the magnetic field strength on the magnetic surface $s = 8/33$ in the L-V-MI14 configuration obtained, $\langle\beta\rangle \approx 0.56\%$.

improve the equilibrium β limit, which for the L-V-TQ and L-V-TUD standard cases is at a level of $\beta = 2\%$. The second objective is connected with the quasi-omnigenity condition, which can be fulfilled for conventional torsatrons with a large aspect ratio, modular triangularity, and a spatial axis [15].

The first result of such an optimization—the case L-V-MI10 with a vacuum magnetic hill—is shown in Fig. 10a. For small $\beta = 0.5\%$, it has $\iota = 0.32$. The VMEC equilibrium result for $\beta = 5.6\%$ is presented in Fig. 10b.

The Fourier spectrum of L-V-MI10 (Fig. 11) near the axis is similar to the spectrum of the W7-X stellarator and consists of (0,1), (1,0), and (1,1) modes. Such a combination of modes gives a typical figure of the contours of B with the maximum near $\theta = \pi$, $\zeta = 0$ and the minimum near $\theta = \pi$, $\zeta = \pi$ (Fig. 12).

The quasi-omnigenous structure of J contours in the near-axis region for the L-V-MI10 configuration obtained is shown in Fig. 13. According to this plot, there is no loss of trapped α particles starting from the plasma center. However, the quasi-omnigeneity condition is not fulfilled in the edge region and the particles starting there will be lost.

The second configuration numerically obtained, L-V-MI14, has a larger shear, vacuum magnetic hill, and vacuum rotational transform $\iota = 0.34$. L-V-MI14 accommodates a large equilibrium value of $\beta = 10.5\%$ (Fig. 14). The Fourier spectrum of the magnetic field has two main components: $(m, n) = (2,1)$ and $(1,1)$ (Fig. 15), which form exclusively closed contours of B (Fig. 16) aligned with the helical direction $\theta = \zeta$. Using the notation from [24], this configuration might be characterized as antipseudosymmetric.

A nice quasi-omnigenous structure of J contours for the L-V-MI14 case, on the left-hand part of the circle, is shown in Fig. 17. For this reflection value of $B_{\mathrm{ref}} = 1.00$ and $-\pi/2 < \theta < \pi/2$, the integration path is located in one system period. In the right-hand part of the circle, the integration path is larger than one period and, correspondingly, the result for J is not shown.

The table contains the main values obtained for the four configurations of the stellarator L-V: TQ, TUD, MI10 and MI14.

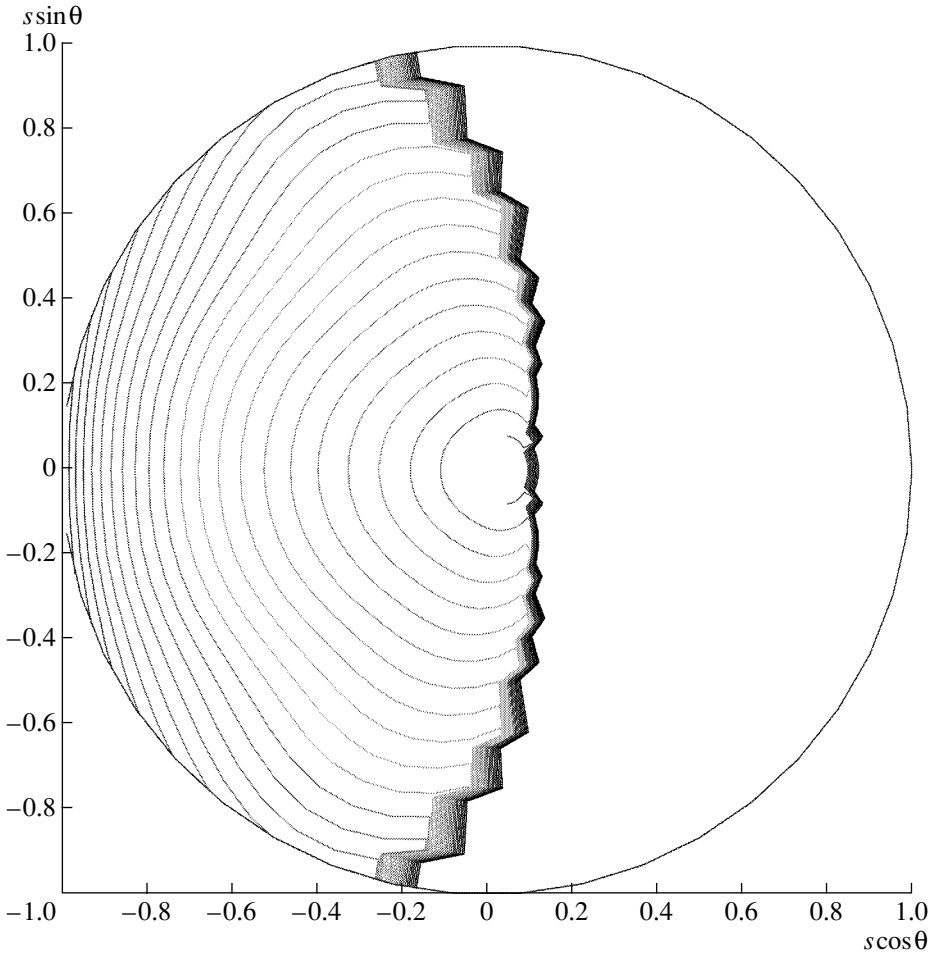

Fig. 17. Second adiabatic invariant contours for $B_{ref} = 1.00$ in the L-V-MI14 configuration obtained, $\langle\beta\rangle = 0$.

5. SUMMARY

Vacuum magnetic configurations of a compact conventional torsatron L-V have been considered as a starting point for further computational optimization aimed at improving the collisionless confinement of the guiding center orbits of fusion α particles and to increase the equilibrium plasma pressure limit. For these purposes, configurations have been obtained with a vacuum rotational transform having a significant shear in the bulk of the configuration, an increased value at the magnetic axis, and a minimized poloidal variation of the second adiabatic invariant on the magnetic surfaces. Two interesting magnetic configurations that are important for applications were found that have improved collisionless orbits together with equilibrium β limits at a level of 10%. The optimization regarding the MHD stability and the coil design remain to be studied.

ACKNOWLEDGMENTS

The authors are grateful to Dr. S.P. Hirshman for providing us with the VMEC and DESCUR codes and to M. Mikhailov and S. Gori, as well as R. Zille, for their help with the computational tools and discussions. The work was financially supported by INTAS, grant no. 99–00592; the Russian–German Agreements WTZ-V RUS-563-98 and WTZ RUS 01-581; the Russian Foundation of Basic Research, project no. N 00-02-17105; the Russian Federal Program for Support of the Leading Scientific Schools, grant no. N 00-15-96526; the Fonds National Suisse pour la Recherche Scientifique; and Euratom. The computational results were performed at the NEC-SX5 platforms at the Centro Svizzero di Calcolo Scientifico in Manno, Switzerland, and at the Rechenzentrum Garching, Max-Planck-Institut für Plasmaphysik, Germany.

REFERENCES

1. G. M. Batanov, E. N. Bondarchuk, S. A. Bulgakov, *et al.*, in *Proceedings of the 7th International Conference on Engineering Problems of Fusion Reactors, St. Petersburg, 2002*.
2. A. N. Boozer, Phys. Fluids **26**, 496 (1983).

3. J. Nührenberg and R. Zille, Phys. Lett. A **129**, 113 (1988).
4. F. Anderson, A. Almagri, D. Anderson, *et al.*, Fusion Technol. **27**, 273 (1995).
5. J. Nührenberg, W. Lotz, and S. Gori, in *Proceedings of International School of Plasma Physics on Theory of Fusion Plasmas* (SIF, Bologna, 1994), p. 3.
6. G. Neilson, A. H. Reiman, M. Zarnstorff, *et al.*, Phys. Plasmas **7**, 1911 (2000).
7. A. Reiman, L. Ku, D. Monticello, *et al.*, Phys. Plasmas **8**, 2083 (2001).
8. S. Okamura, K. Matsuoka, S. Nishimura, *et al.*, Nucl. Fusion **41**, 1865 (2001).
9. W. Lotz, J. Nuhrenberg, and C. Schwab, in *Proceedings of the 13th International Conference on Plasma Physics and Controlled Nuclear Fusion Research, Washington, 1990* (IAEA, Vienna, 1991), Vol. 2, p. 603.
10. S. Gori, W. Lotz, and J. Nuhrenberg, in *Proceedings of International School of Plasma Physics on Theory of Fusion Plasmas* (SIF, Bologna, 1996), p. 335.
11. D. Palumbo, Nuovo Cimento B **53**, 507 (1968).
12. M. I. Mikhailov, V. D. Shafranov, A. A. Subbotin, *et al.*, Nucl. Fusion **42**, 23 (2002).
13. J. Cary and S. Shasharina, Phys. Rev. Lett. **78**, 674 (1997).
14. D. Spong, S. P. Hirshman, J. C. Whitson, *et al.*, Phys. Plasmas **5**, 1752 (1998).
15. M. Yu. Isaev, J. Nührenberg, M. I. Mikhailov, *et al.*, Submitted to Nucl. Fusion.
16. http://www.nag.co.uk.
17. S. P. Hirshman and H. K. Meier, Phys. Fluids **28**, 1387 (1985).
18. S. P. Hirshman and O. Betancourt, J. Comput. Phys. **96**, 99 (1991).
19. J. Nührenberg and R. Zille, in *Proceedings of International School of Plasma Physics on Theory of Fusion Plasmas, Varenna, 1987* (Compositori, Bologna, 1988), p. 3.
20. R. H. Fowler, J. A. Rome, and J. F. Lyon, Phys. Fluids **28**, 338 (1985).
21. http://www.rzg.mpg.de.
22. C. Mercier, Nucl. Fusion Suppl. **2**, 801 (1962).
23. D. V. Anderson, W. A. Cooper, R. Gruber, *et al.*, *Scientific Computing on Supercomputers II* (Plenum, New York, 1992), p. 1011; W. A. Cooper, Plasma Phys. Controlled Fusion **34**, 1011 (1992).
24. M. I. Mikhailov, W. A. Cooper, M. Yu. Isaev, *et al.*, in *Proceedings of International School of Plasma Physics on Theory of Fusion Plasmas, Varenna, 1987* (Compositori, Bologna, 1998), p. 185.

Plasma Physics Reports, Vol. 29, No. 9, 2003, pp. 740–747. Translated from Fizika Plazmy, Vol. 29, No. 9, 2003, pp. 801–808.

BEAMS IN PLASMA

Unsteady Beam–Plasma Discharge: I. Mathematical Model and Linear Theory

Yu. P. Bliokh*, M. G. Lyubarsky, V. O. Podobinsky***, and Ya. B. Fainberg*****

**Technion, Haifa 3200, Israel*

***Karazin National University, pl. Svobody 4, Kharkov, 61077 Ukraine*

****Institute of Plasma Electronics and New Acceleration Methods, National Science Center Kharkov Institute of Physics and Technology, ul. Akademicheskaya 1, Kharkov, 61108 Ukraine*

Received December 11, 2002; in final form, February 13, 2003

Abstract—A mathematical model is constructed that describes the development of the beam–plasma instability in a traveling-wave tube amplifier in the presence of a neutral gas. Steady solutions are derived for conditions of microwave discharges in a magnetized plasma-filled traveling-wave tube amplifier, and their stability is investigated. It is shown that the steady-state amplification regime may become unstable and change to the self-modulation regime. The relationships between the amplifier parameters at the instability threshold are obtained, and the frequencies of the excited ion acoustic waves are determined. The results of numerical modeling are found to agree well with the analytical results. © *2003 MAIK "Nauka/Interperiodica".*

1. INTRODUCTION

One of the most promising approaches to creating high-power microwave sources employs plasma-filled waveguide structures (PWSs) in which an electron beam excites a synchronous wave. In recent years, PWS-based microwave devices have been developed that are capable of continuously generating high output powers in the centimeter range. This is one of a few lines of research that has become technically feasible in plasma physics. In contrast to standard vacuum waveguide structures, the microwave fields produced in a PWS change the electrodynamic parameters of the structure. That is why, in order to adequately describe the excitation of a PWS by an electron beam, it is necessary to elaborate a new self-consistent theory of the beam–plasma instability with allowance for both the change in the medium (plasma) parameters under the action of high-power microwave radiation and the associated changes in the generation process and microwave propagation.

Such a theory is constructed by developing and analyzing the mathematical models that take into account different aspects of the self-consistent dynamics of microwaves and plasmas. The first studies in this direction were carried out by Zakharov [1] and Kuznetsov [2], who investigated the self-consistent dynamics of the plasma and of the microwave propagating in it.

In a PWS with an electron beam, it is the excitation of a synchronous wave (rather than its propagation) that is primarily affected by the plasma nonlinearity. The theory that takes into account this property of the beam–plasma instability (BPI) in a PWS began to be developed in [3–7] via study of the effect of the microwave ponderomotive force [8] on the generation and amplification of microwaves in a plasma-filled traveling-wave tube (TWT). In those papers, it was shown that the ejection of a plasma from the regions of the most intense microwave generation gives rise to two new effects: the onset of low-frequency modulation of the microwave signal and a change in the mechanism for the instability saturation. These main properties of the excitation of a PWS by an electron beam were confirmed in experiments with hybrid structures [9] and a magnetized plasma waveguide [7, 10].

In the papers cited above, a study was made of the motion of the plasma as a single entity under the action of the microwave fields produced in it. Such a motion is characteristic of long-pulse devices. In short-pulse devices, it is only the light (electron) plasma component that is typically set in motion. A theory of the resonance plasma amplifier that takes into account the nonlinear nature of the electron motion in a cold plasma was constructed by Bobylev *et al.* [11].

In all of the cited papers, it was assumed that the excited high-power microwave field exclusively causes a redistribution of the plasma density and has no influence on the plasma source. This assumption is valid when the neutral gas is completely (100%) ionized or when the amplitudes of the excited microwaves are relatively small, so that the oscillatory energy of the plasma electrons is insufficient to ionize the neutral plasma component. A beam–plasma discharge (BPD) that otherwise develops in the system [12] serves as an additional plasma source, whose power and spatial distribution are governed by the parameters of the excited wave. The wave of the density of the additional plasma thus produced propagates away from the source region in the direction opposite to that of the beam and can

1063-780X/03/2909-0740$24.00 © 2003 MAIK "Nauka/Interperiodica"

give rise not only to effects analogous to those occurring under the action of the microwave ponderomotive force (such as loss of stability of the steady-state amplification regime and a transition to the self-modulation regime [5]) but also to radically new effects, which can be associated with the facts that the BPD has a threshold in terms of the electron oscillatory energy and that, in contrast to the microwave ponderomotive force, the discharge creates an increased (in comparison with the initial level) plasma density in the region of maximum microwave field.

In the present paper, we develop a theory of a linear TWT amplifier in which the amplitude of the output signal is close to the threshold for initiating a BPD. By "linear" we mean an amplifier in which the output signal amplitude is small enough that the nonlinearity of the motion of the beam electrons in the field of the wave excited by them can be neglected. However, the beam–wave–plasma system is treated as being nonlinear.

Our paper is organized as follows. In Section 2, we derive the basic equations and present the restrictions on the range of their validity. In Section 3, we analytically investigate the stability of the steady solutions to these equations. In Section 4, we solve the equations numerically and compare the results obtained with the analytical ones. Finally, we summarize the main conclusions of the theory proposed here.

2. BASIC EQUATIONS

We consider a TWT amplifier in the form of a slow wave structure (with the cross-sectional area S_w and length L) that is filled partially with a plasma (with the cross-sectional area S_p and initial uniform density n_0) and is penetrated by a nonrelativistic electron beam (with the cross-sectional area S_b, density $n_b \ll n_0$, and velocity v_b). We assume that, in the waveguide structure, there is a residual neutral gas with the density N_0 and ionization energy W_i.

Before proceeding to the construction of a mathematical model, we note that the basic equations will be derived under certain simplifying assumptions that make it possible to remove from consideration the effects that are unimportant for our purposes here. The main assumptions of our model are as follows.

(i) The guiding magnetic field is strong enough that the radial motion of the beam electrons and plasma particles can be neglected.

(ii) The condition $S_b \ll S_p$ is satisfied in order that the beam stratification due to the transverse nonuniformity of the field of the excited wave can be ignored.

(iii) Since, in the cases that are of interest for microwave electronics, the inequality $v_g \gg c_s$ (where v_g is the group velocity of the microwave, $c_s = \sqrt{T_e/M}$ is the ion acoustic speed, T_e is the plasma electron temperature, and M is the mass of a plasma ion) is satisfied by a large margin, it is also possible to neglect transient processes accompanying the excitation of the wave by the beam and to assume that, at each instant, the longitudinal profile of the microwave amplitude is steady-state and corresponds to that for an instantaneous longitudinal plasma density profile.

Using the fact that, for $n_b \ll n_0$, the spatial growth rate δk of the beam instability is small ($\delta k \ll k_0$, where k_0 is the wavenumber of a microwave), we represent the longitudinal component of the electric field of the amplified wave in the form

$$E(\mathbf{r}, z, t) = E_0(z, t)G(\mathbf{r})\exp(ik_0 z - i\omega_0 t) + \text{c.c.} \quad (1)$$

Here, $E_0(z, t)$ is the slowly varying complex amplitude and the function $G(\mathbf{r})$ describes the radial profile of the field of the eigenmode of the structure. The frequency of the wave and its wavenumber are related by the resonance condition $\omega_0 = k_0 v_b$.

In what follows, we assume that the electron beam amplifies the natural noise fluctuations rather than the external signal fed through the entrance plane of the system. If the interaction region is sufficiently long, the beam instability, being resonant in nature, acts as a natural narrowband frequency filter whose bandwidth decreases with increasing system length. Consequently, we can assume that, to zeroth order in the width of the amplification band, there exists only a single wave in the system, specifically, the one that has the maximum gain. Under the above assumptions, the longitudinal profile of the amplitude of this microwave is described by the following time-independent equations for the beam instability in an unsteady inhomogeneous plasma [7, 10]:

$$\frac{\partial \varepsilon}{\partial \zeta} + i\mathcal{N}(\zeta, \tau)\varepsilon = -\frac{1}{2\pi}\int_0^{2\pi} e^{-i\varphi(\varphi_0, \zeta)}d\varphi_0,$$
$$\frac{\partial^2 \varphi}{\partial \zeta^2} = \mathrm{Re}(\varepsilon e^{i\varphi}). \quad (2)$$

Here, $\zeta = \delta k \cdot z$ is the dimensionless longitudinal coordinate, $\varepsilon = \dfrac{ek_0 E_0 G(0)}{m v_b^2 \delta k^2}$ is the dimensionless wave amplitude, $\varphi = \omega(z/v_b - t)$ is the phase of a beam electron in the wave, φ_0 is the initial phase in the injection plane of the beam ($z = 0$), $\delta k = k_0\left(\dfrac{\omega_b^2 G^2(0)(S_b/\int_{S_w} G^2 ds)}{\omega_0^2 k_0(\partial D/\partial k_0)}\right)^{1/3}$ is the spatial growth rate of the beam instability in a homogeneous plasma, $D(\omega, k, \bar{n}_p)$ is a function whose zeros determine the dispersion of the eigenmodes of the system, the detuning $\mathcal{N}(\zeta, \tau) = \eta(\zeta, \tau) - \dfrac{1}{\zeta_0}\int_0^{\zeta_0}\eta(\zeta, \tau)d\zeta$ characterizes the dimensionless deviation of the wave phase velocity

from the beam velocity (due to the plasma density perturbation), $\eta(\zeta, \tau) = \frac{k_0}{2\delta k}\frac{\omega_p}{v_{ph}}\frac{\partial v_{ph}}{\partial \omega_p}\frac{\delta \bar{n}_p(\zeta, \tau)}{n_0}$ is the dimensionless amplitude of the plasma density perturbation, v_{ph} is the phase velocity of the microwave, $\delta \bar{n}_p \equiv (\int_{S_p} G^2 \delta n_p ds)(\int_{S_p} G^2 ds)^{-1}$ is the normalized perturbed plasma density averaged over the plasma cross section, and ζ_0 is the distance over which the microwave is amplified in the linear stage.

The inequality $v_g \gg c_s$ allows us to use the time-independent equations for the beam instability and to account for the unsteady nature of the plasma via the parametric dependence of the plasma density perturbations δn_p on the dimensionless time $\tau = \delta k \cdot c_s t$.

Equations (2) should be supplemented with boundary conditions. We assume that the beam velocity and beam density at the entrance to the system ($\zeta = 0$) are constant and specify the initial field amplitude $|\varepsilon|_0$ and phase as

$$\varepsilon(0, \tau) = |\varepsilon|_0, \quad \varphi(0, \tau) = \varphi_0, \quad \frac{\partial \varphi}{\partial \zeta}(0, \tau) = 0, \quad 0 \le \varphi_0 \le 2\pi. \tag{3}$$

These conditions are sufficient to determine the field amplitude ε at any point of the system, provided that the longitudinal plasma density profile and, accordingly, the dependence $\eta(\zeta, \tau)$ are known.

In order to arrive at the desired closed set of the basic equations, we need to write out the dynamic equations that describe the motion of the plasma as a single entity in the presence of the source (BPD). To do this, we make the following additional simplifying assumptions.

(i) Because of its resonant nature, the beam instability is very sensitive to the degree to which the plasma is inhomogeneous; hence, we will assume that the condition $\delta n_p \ll n_0$ is satisfied and will describe plasma motions in the linear approximation.

(ii) In order to eliminate the effect of inelastic collisions, which change the number of particles in the waveguide volume, we assume that the length of the interaction region is much shorter than the electron mean free path with respect to inelastic processes (e.g., recombination), in which case the temporal dynamics of the plasma density and its spatial distribution are determined by the balance between the plasma particles produced by the source and those escaping from the waveguide through its ends.

(iii) The microwave field intensity is such that the dependence of the cross section σ for ionization of neutral gas molecules by plasma electrons on the mean electron oscillatory energy $W = e^2|E|^2/2m\omega^2$ can be approximated by a linear function, $\sigma = \sigma'(W - W_i)$, where σ' = const (note that this assumption is valid over a fairly wide energy range, $-W\ W_i \le W \le 1.5W_i$).[1]

Taking into account the above assumptions and averaging the continuity equations and the equations of motion for the electron and ion plasma components over the fast oscillations, we obtain the following equations of plasma motion:

$$\frac{\partial \eta}{\partial \tau} + \frac{\partial u}{\partial \zeta} = S(\zeta, \tau), \quad \frac{\partial u}{\partial \tau} + \frac{\partial \eta}{\partial \zeta} = 0. \tag{4}$$

Here, $u(\zeta, \tau) = \frac{k_0}{2\delta k}\frac{\omega_p}{v_{ph}}\frac{\partial v_{ph}}{\partial \omega_p}\frac{\bar{v}(\zeta, \tau)}{c_s}$ is the dimensionless plasma velocity averaged over the plasma cross section; $S = S_0(\theta_1(\zeta, \tau) - \theta_2(\zeta, \tau))(|\varepsilon|^2(\zeta, \tau) - \varepsilon_i^2)$ (where $S_0 = \frac{N_0\sigma' m v_b^2}{2k}\frac{\sqrt{M/m}}{2}\left(\frac{\delta k}{k_0}\right)^2\frac{\omega_p}{v_{ph}}\frac{\partial v_{ph}}{\partial \omega_p}\int_{S_p} G^4(\mathbf{r})ds \times (G^2(0)\int_{S_p} G^2(\mathbf{r})ds)^{-1}$ is the dimensionless neutral gas pressure); $\varepsilon_i^2 = W_i G^2(0)\int_{S_p} G^2 ds\left(\frac{m v_b^2}{2}\left(\frac{\delta k}{k_0}\right)^4\int_{S_p} G^4 ds\right)^{-1}$ is the squared dimensionless ionization energy; $\theta_{1,2} = \theta(\zeta - \zeta_{1,2})$ (where $\theta(\zeta)$ the Heaviside step function); and $\zeta_1(\tau)$ and $\zeta_2(\tau)$ are, respectively, the coordinates of the left and right boundaries of the region of a BPD, which are solutions to the equation $|\varepsilon|(\zeta, \tau) = \varepsilon_i$ (we note that, for $|\varepsilon|(l) > \varepsilon_i$, where $l = \delta k \cdot L$, the right boundary of the BPD region coincides with the exit end of the amplifier, $\zeta_2 \equiv l$).

Equations (4) should be supplemented with boundary conditions at the entrance (left) boundary of the system, $\zeta = 0$, and at its exit (right) boundary, $\zeta = l$. In what follows, we will use the most general form of the linear boundary conditions:

$$(1 + \gamma)\eta(0, \tau) + (1 - \gamma)u(0, \tau) = 0, \quad (1 + \gamma)\eta(l, \tau) - (1 - \gamma)u(l, \tau) = 0. \tag{5}$$

Here, the reflection coefficients of the left and right ends of the system for an ion acoustic wave are assumed to be the same and are denoted by γ ($-1 < \gamma < 1$). For $\gamma < 0$, the wave phase does not change as the wave is reflected from the system ends, while, for $\gamma > 0$, the wave phase changes by π.

Under the above assumptions, Eqs. (2) and (4) with initial conditions (3) and boundary conditions (5) con-

[1] We assume that the amplifier is filled with a weakly ionized cold gas at a low pressure, so that the plasma can be treated as being weakly collisional, $l_{e,n} > L$ (where $l_{e,n}$ is the electron mean free path with respect to elastic collisions with neutral gas molecules). In this case, the total energy of the electrons is determined mainly by their oscillatory energy. Under the experimental conditions of [7, 9, 11], the electron mean free path in question at the beginning of a BPD is estimated to be $l_{e,n} > 10^2$ cm $> L$.

stitute the basis of a closed mathematical model of a BPD in a magnetized plasma-filled TWT amplifier. It is easy to see that, under the prescribed boundary and initial conditions (for l, $|\varepsilon|_0$, and γ), the model contains only two parameters: S_0 and ε_i.

3. STEADY-STATE LINEAR AMPLIFICATION REGIME AND ITS STABILITY

We assume that the output signal amplitude is small, $|\varepsilon(l)| \ll 1$, which allows us to consider the motion of the beam electrons in the linear approximation. In this case, the beam interacts linearly with the wave over the entire length of the system, $\zeta_0 \equiv l$.

Equations (2) can be simplified by using the condition that the wave amplitude is small. To do this, we linearize the second of Eqs. (2) in the small perturbations $\delta\varphi \sim \varepsilon \ll 1$ of the phases $\varphi = \varphi_0 + \delta\varphi$ of the beam electrons and carry out integration over the initial phases in the first of the equations. As a result, Eqs. (2) reduce to the equation

$$\frac{\partial^2}{\partial\zeta^2}\left(\frac{\partial\varepsilon}{\partial\zeta} + i\mathcal{N}(\zeta,\tau)\varepsilon\right) = \frac{i}{2}\varepsilon, \tag{6}$$

and initial conditions (3) become

$$\begin{aligned}&\varepsilon(0,\tau) = \varepsilon_0, \quad \frac{\partial\varepsilon}{\partial\zeta}(0,\tau) = -i\mathcal{N}(0,\tau)\varepsilon_0,\\ &\frac{\partial^2\varepsilon}{\partial\zeta^2}(0,\tau) = -\left(\mathcal{N}^2(0,\tau) + i\frac{\partial\mathcal{N}}{\partial\zeta}(0,\tau)\right)\varepsilon_0.\end{aligned} \tag{7}$$

Let us find steady solutions to Eqs. (4) and (6) with boundary conditions (5) and initial conditions (7). The steady solutions will be denoted by the subscript *st*. Setting $\partial/\partial\tau \equiv 0$ in Eqs. (4), we get

$$\eta_{st} = \frac{1}{2}\frac{1-\gamma}{1+\gamma}S_0\int_{\zeta_1}^{\zeta_2}(|\varepsilon|_{st}^2(\zeta) - \varepsilon_i^2)d\zeta = \text{const}. \tag{8}$$

The coordinates $\zeta_{1,2}$ of the left and right boundaries of the BPD region will be determined below.

Now, we turn to Eq. (6). Since, in the steady-state regime, the plasma is homogeneous, the detuning, by its definition, is equal to zero, $\mathcal{N}_{st} \equiv 0$. In this case, Eq. (6) has the following well-known solution, which satisfies initial conditions (7):

$$\varepsilon_{st}(\zeta) = \frac{|\varepsilon|_0}{3}\sum_{i=1}^{3}\exp(\lambda_i\zeta), \tag{9}$$

where the numbers λ_i are the roots of the equation $\lambda^3 = i/2$. Note that, since the level of the noise fluctuation is very low, the requirement that the amplification be efficient ($|\varepsilon(l)| \gg |\varepsilon|_0$) is equivalent to the condition $l \gg 1$.

In order to simplify expression (8), note that knowledge of the microwave field amplitude solely in the BPD region is sufficient for determining the plasma density. Since only one of the roots λ_i has a positive real part, $\lambda_1 = 2^{-4/3}(\sqrt{3} + i)$, the condition $l \gg 1$ enables us to neglect the exponentially small terms in solution (9) over the entire interval ζ_2–ζ_1 near the right end of the amplifier and to use the approximate equality $\varepsilon_{st}(\zeta) \cong |\varepsilon|_0\exp(\lambda_1\zeta)/3$, which holds over the source region. With allowance for the fact that the dependence $|\varepsilon|_{st}(\zeta)$ is monotonic, we obtain from the equality $|\varepsilon|_{st}(\zeta) = \varepsilon_i$ the relationships

$$\zeta_1 = \frac{1}{\beta}\ln\frac{3\varepsilon_i}{|\varepsilon|_0}, \quad \zeta_2 = l, \tag{10}$$

where $\beta \equiv \mathrm{Re}\,\lambda_1 = 2^{-4/3}\sqrt{3}$.

Using relationships (10) and the expression for $|\varepsilon|_{st}(\zeta)$, we can readily see that the assumption about the linear character of the dependence of the ionization cross section on the electron energy in the range $W \leq 1.5W_i$ is equivalent to the condition $l - \zeta_1 < \frac{1}{2\beta}\ln(3/2)$, which indicates that the length of the BPD region is small in comparison with the characteristic scale length $1/\beta$ of the microwave field. Taking into account this condition, we reduce expression (8) to

$$\eta_{st} = \frac{\beta}{2}\frac{1-\gamma}{1+\gamma}S_0\varepsilon_i^2(l-\zeta_1)^2. \tag{11}$$

Now, we investigate the stability of solutions (9) and (11), which describe the steady-state amplification regime. To do this, we determine the behavior of arbitrarily small perturbations of the plasma density, $\delta\eta(\zeta, \tau)$, plasma velocity, $\delta u(\zeta, \tau)$, and microwave field, $\delta\varepsilon(\zeta, \tau)$. Before proceeding to the derivation of the set of linear equations for these perturbations, we should make the following two remarks.

The first remark concerns Eq. (6). The plasma density perturbation gives rise to the detuning $\delta\mathcal{N}(\zeta, \tau) = \delta\eta(\zeta, \tau) - \frac{1}{l}\int_0^l\delta\eta(\zeta, \tau)d\zeta$. In the so-called adiabatic approximation (i.e., when the scale on which the plasma density varies is much longer than the characteristic scale of the microwave field, $\left|\frac{1}{\delta\eta}\frac{\partial\delta\eta}{\partial\zeta}\right| \ll \left|\frac{1}{\varepsilon}\frac{\partial\varepsilon}{\partial\zeta}\right| \sim 1$), the solution to Eq. (6) is well known. Unfortunately, we cannot use this solution in constructing the theory because, under the above assumptions, the perturbations of the plasma density and microwave field are not independent but are related by Eqs. (4). Therefore, it is incorrect to make an a priori assumption that their spatial scales are significantly different.

The second remark concerns Eqs. (4). In the presence of perturbations, the condition $|\varepsilon(\zeta, \tau)| = \varepsilon_i$ is satisfied not at the point ζ_1 but at some other point $\zeta_3(\tau)$. To be specific, we assume that this point lies to the right

of the point ζ_1 and consider the region $\zeta_1 < \zeta < \zeta_3$. Since its length is proportional to the perturbation amplitude, the solution to Eqs. (2) in this region is proportional to $\int_{\zeta_1}^{\zeta_3} \delta S d\zeta$ (where δS is the perturbation of the source) and is thus of the second order of smallness. Consequently, we can exclude this region from consideration and set $\zeta_3 \equiv \zeta_1$.

To first order in the small detuning $\delta\mathcal{N}$, Eq. (6) and initial conditions (7) have the form

$$\frac{\partial^3 \varepsilon}{\partial \zeta^3} - \frac{i}{2}\varepsilon = -i\frac{\partial^2}{\partial \zeta^2}[\delta\mathcal{N}(\zeta, \tau)\varepsilon_{st}(\zeta)], \tag{12}$$

$$\varepsilon(0, \tau) = |\varepsilon|_0, \quad \frac{\partial \varepsilon}{\partial \zeta}(0, \tau) = -i\delta\mathcal{N}(0, \tau)|\varepsilon|_0, \quad \frac{\partial^2 \varepsilon}{\partial \zeta^2}(0, \tau) = -i\frac{\partial \delta\mathcal{N}}{\partial \zeta}(0, \tau)|\varepsilon|_0, \tag{13}$$

where $\varepsilon_{st}(\zeta)$ is given by expression (9).

With allowance for the second of the above remarks, Eqs. (4) and boundary conditions (5) can be transformed into

$$\frac{\partial \delta\eta}{\partial \tau} + \frac{\partial \delta u}{\partial \zeta} = \delta S(\zeta, \tau), \quad \frac{\partial \delta u}{\partial \tau} + \frac{\partial \delta\eta}{\partial \zeta} = 0, \tag{14}$$

$$(1 + \gamma)\delta\eta(0, \tau) + (1 - \gamma)\delta u(0, \tau) = 0, \quad (1 + \gamma)\delta\eta(l, \tau) - (1 - \gamma)\delta u(l, \tau) = 0, \tag{15}$$

where $\delta S = 2S_0\theta(\zeta - \zeta_1)|\varepsilon|_{st}(\zeta)\delta|\varepsilon|(\zeta, \tau)$.

Assuming that the dependence $\delta\mathcal{N}(\zeta, \tau)$ is prescribed, the solution to Eq. (12) that satisfies initial conditions (13) can be found by the method of variation of constants. The solution thus derived yields the following expression for the perturbation of the microwave field amplitude:

$$\delta|\varepsilon|(\zeta, \tau) = |\varepsilon|_{st}(\zeta)\mathrm{Im}\left[\left(\sum_{i=1}^{3} F_i(\delta\mathcal{N})e^{\lambda_i \zeta}\right)\left(\sum_{i=1}^{3} e^{\lambda_i \zeta}\right)^{-1}\right], \tag{16}$$

where

$$F_i(\delta\mathcal{N}) = \frac{1}{3}\sum_{k=1, k\neq i}^{3}\int_0^\zeta \delta\mathcal{N}(\zeta', \tau)e^{(\lambda_k - \lambda_i)\zeta'}d\zeta'.$$

The perturbation of the source, δS, in Eqs. (14) is determined by the change in the field amplitude exclusively in the source region, in which expression (16) can be simplified by using a procedure analogous to that used in obtaining expressions (10) and (11). As a result, we arrive at the following expression for the perturbation of the field amplitude in the source region $l - \zeta_1$:

$$\delta|\varepsilon|(\zeta, \tau) = \frac{1}{3}|\varepsilon|_{st}(\zeta)\int_0^\zeta \delta\mathcal{N}(\zeta', \tau)\mathrm{Im}(e^{\alpha\zeta'} - e^{\alpha(\zeta - \zeta')})d\zeta', \tag{17}$$

where $\alpha = -\beta(1 + \sqrt{3}i)$.

Since Eqs. (14), boundary conditions (15), and expression (17) are all linear and uniform in the perturbations, we can represent the time dependence of the perturbation amplitudes in the form $\sim\exp(-i\Omega\tau)$, in which case Eqs. (14) reduce to

$$\frac{\partial \delta u}{\partial \zeta} - i\Omega\delta\eta = \delta S(\zeta), \quad \frac{\partial \delta\eta}{\partial \zeta} - i\Omega\delta u = 0 \tag{18}$$

and boundary conditions (15) become

$$(1 + \gamma)\delta\eta(0) + (1 - \gamma)\delta u(0) = 0, \quad (1 + \gamma)\delta\eta(l) - (1 - \gamma)\delta u(l) = 0. \tag{19}$$

Here,

$$\delta S = \frac{2}{3}S_0\theta(\zeta - \zeta_1)|\varepsilon|_{st}^2(\zeta) \times \int_0^\zeta \left(\delta\eta(\zeta') - \frac{1}{l}\int_0^l \delta\eta(\zeta'')d\zeta''\right)\mathrm{Im}[e^{\alpha\zeta'} + e^{\alpha(\zeta - \zeta')}]d\zeta'. \tag{20}$$

Note that the positive and negative imaginary parts of Ω correspond, respectively, to the stability and instability of the steady state under consideration. The intermediate case, when the frequency Ω is real, corresponds to the sought-for critical parameter values at which the steady state loses stability.

For a prescribed dependence $\delta S(\zeta)$, the solution to Eqs. (18) that satisfies boundary conditions (19) can be derived by the method of variation of constants:

$$\delta\eta = \frac{1}{2}\int_0^\zeta \delta S(\zeta')[e^{i\Omega(\zeta - \zeta')} - e^{i\Omega(\zeta' - \zeta)}]d\zeta' + C(e^{-i\Omega\zeta} - \gamma e^{i\Omega\zeta}), \tag{21}$$

where

$$C = \frac{1}{2}(1 - \gamma^2 e^{2i\Omega l})\int_0^l \delta S(\zeta)e^{i\Omega\zeta}(1 - \gamma e^{2i\Omega(l - \zeta)})d\zeta. \tag{22}$$

Note that the domain of integration in formula (22) is limited to the BPD region $l - \zeta_1$, because the function $\delta S(\zeta)$, given by expression (20), vanishes outside this region. Let us consider the characteristic spatial scales on which the quantities in the integrand vary. These are the scale $1/\beta$ of the microwave field, the length $l - \zeta_1$ of the source region, and the characteristic scale $2\pi/\Omega$ of the plasma density variations (in the dimensionless

variables introduced above, we have $K \equiv \Omega$, where K is the wavenumber of the low-frequency wave). The scale of the microwave field is much longer than the length of the source region; this circumstance has been used in the above analysis. As will be clear later, we can assume that the spatial scale of the plasma density variations in of the same order of magnitude as the scale of the microwave field; i.e., it is also substantially longer than the length of the source region. With such relations between the scales, we substitute expression (22) into formula (20) and expand the integrand on the right-hand side of the resulting equality in a series in $l - \zeta_1$. The right-hand side of expression (22) thus expanded contains only the amplitude of the plasma density perturbation outside the BPD region. According to solution (21), this perturbation amplitude is equal to $\delta\eta = C(e^{-i\Omega\zeta} - \gamma e^{i\Omega\zeta})$. We divide both sides of the equality by C and obtain, to first order in the source length $l - \zeta_1$, a complex expression from which to derive the dispersion relation

$$\Omega_n l = 2\pi n, \quad n = 1, 2, \ldots \tag{23}$$

and the relationship between the amplifier parameters at the stability boundary of the steady-state regime,

$$P = P_c \equiv \frac{3}{2^{1/3}}\frac{1+\gamma}{1-\gamma}\left(\frac{\mu_n^4}{\mu_n^2 - 1} - 1\right). \tag{24}$$

Here, we have introduced the quantity $P \equiv S_0\int_{\zeta_1}^{l}|\varepsilon|_{st}^2(\zeta)d\zeta$ and the parameter $\mu_n \equiv \Omega_n/2\beta$, which characterizes the relationships between the spatial scales of the excited ion acoustic wave and microwave field.

The solution with $n = 0$ is excluded from solutions (23) because it certainly does not satisfy relationship (24). Moreover, according to this relationship, the only ion acoustic waves that can be excited at the stability boundary of the steady-state regime are those whose frequency satisfies the condition $\mu_n > 1$, which, in fact, indicates that the spatial scale of the microwave field is longer than the wavelengths of the low-frequency waves ($1/2\beta > 1/\Omega_n$). This confirms the correctness of the above remark that the well-known solution to Eq. (12) in the adiabatic approximation cannot be used to construct the theory.

As follows from relationship (24), the quantity P_c has a minimum at $\mu = \bar{\mu} = \sqrt{2}$. This indicates that the first wave to be excited is an ion acoustic wave whose frequency $\Omega_k = 2\pi k/l$ is closest to $\bar{\Omega} = 2\sqrt{2}\beta$. The characteristic spatial scale of this ion acoustic wave is on the order of the scale of the microwave field. This circumstance confirms the correctness of the assumption made in deriving dispersion relation (23) and relationship (24).

Let us investigate the dependence of the quantity P_c on the reflection coefficient γ. Relationship (24) implies that negative values of the reflection coefficient (the wave phase does not change as the wave is reflected from the system ends) decrease the value of the quantity P_c in comparison with that for $\gamma = 0$ (in the absence of reflections), while positive γ values (the wave phase changes by π) increase the value of this quantity. The reason is that negative and positive values of the reflection coefficient correspond, respectively, to the intensification and relaxation of the perturbations. Note that relationship (24) has two singularities $\gamma = \pm 1$, near which solution (23) is invalid. Expression (8) implies that, as $\gamma \longrightarrow -1$, the quantity η_{st} increases without bound, which violates the applicability condition $\delta n_p \ll n_0$ of our mathematical model. In the limit $\gamma \longrightarrow +1$, it is incorrect to retain only the first term in the expansion of the integrand in formula (22) in a series in the length $l - \zeta_1$ of the BPD region.

To conclude this section, we analyze the main approximation that was used to derive the basic equations, namely, the linear approximation for the equation of plasma motion. Using solution (9), we find the explicit form of the condition $\delta n_p \ll n_0$ in terms of the parameters of the waveguide structure:

$$\begin{aligned}&\frac{N_0\sigma' W_i}{\delta k}\frac{1-\gamma}{1+\gamma}\sqrt{\frac{M}{m}}(\delta kL - \zeta_1)^2 \\ &\equiv 2\frac{\delta k}{k}\frac{1-\gamma}{1+\gamma}(\delta kL - \zeta_1)\left|\frac{\omega_p}{v_{ph}}\frac{\partial v_{ph}}{\partial \omega_p}\right|^{-1} P \ll 1,\end{aligned} \tag{25}$$

where $\zeta_1 = \dfrac{1}{2\beta}\ln\dfrac{9W_i}{W_0}$ and W_0 is the energy level of the natural plasma fluctuations. Condition (25) can easily be satisfied by choosing the corresponding ranges of neutral gas pressures and beam parameters. As can be seen, the threshold value $P = P_c$ is consistent with this condition, especially if we take into account the fact that the spatial growth rate of the beam instability is small and the BPD region is short (for plasma-filled waveguides, we have $\left|\dfrac{\omega_p}{v_{ph}}\dfrac{\partial v_{ph}}{\partial \omega_p}\right| > 1$).

4. NUMERICAL CALCULATIONS

In order to confirm the results obtained analytically, we numerically solved the basic set of nonlinear equations (2) and (4) with initial conditions (3) and boundary conditions (5). An electron beam was modeled by the particle method, and Eqs. (4) were solved by the method of characteristics. In simulations, we fixed the amplifier length ($l = 7.0$), the beam parameters, the gas species ($\varepsilon_i = 0.06$), and the coefficient of reflection of the ion acoustic wave from the ends of the system ($\gamma = 0$) and varied the gas pressure (the parameter S_0) and the microwave field amplitude at the left end of the ampli-

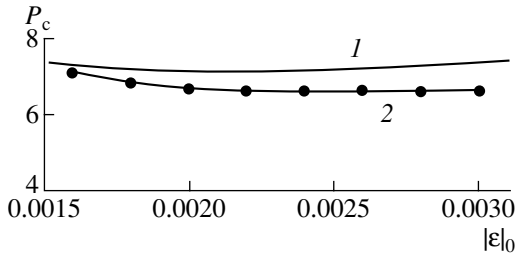

Fig. 1. Dependence of the quantity P_c on the microwave field amplitude at the left end of the amplifier: (*1*) calculations from relationship (24) and (*2*) numerical computations.

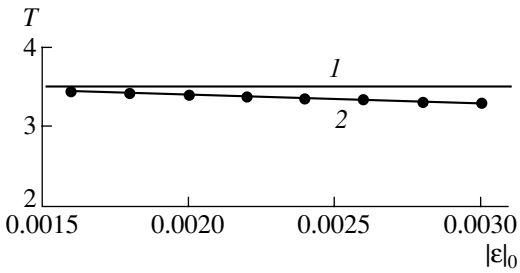

Fig. 2. Dependence of the period of the ion acoustic wave on the microwave field amplitude at the left end of the amplifier: (*1*) calculations from dispersion relation (23) and (*2*) numerical computations.

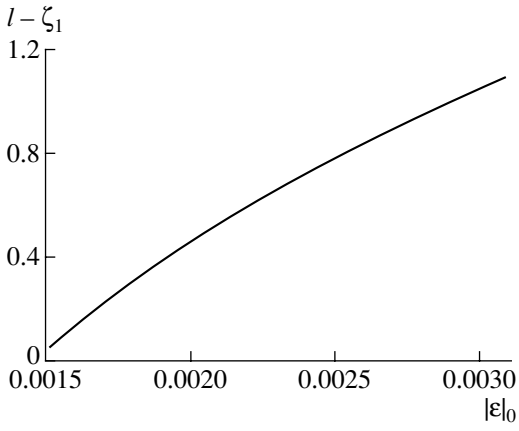

Fig. 3. Dependence of the length of the BPD region on the microwave field amplitude at the left end of the amplifier.

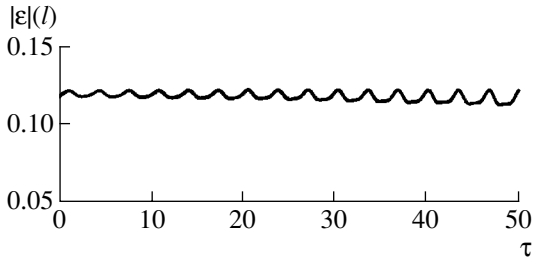

Fig. 4. Time evolution of the amplitude of the output microwave signal in the self-modulation regime.

fier (the parameter $|\varepsilon|_0$). The range over which to vary the parameter $|\varepsilon|_0$ was chosen so that, on the one hand, a microwave is amplified in the linear regime along the entire system and the microwave field amplitude at the exit from the system is small ($|\varepsilon|(l) \ll 1$) and, on the other hand, this amplitude is above the threshold $|\varepsilon| = \varepsilon_i$ for the onset of a BPD.

Our numerical simulations confirmed both analytical conclusions: that the steady-state amplification regime becomes unstable and that it is threshold in nature. The results of calculations are illustrated in Figs. 1–4.

Figure 1 shows the quantity $P = P_c$ calculated as a function of the microwave field amplitude at the left end of the amplifier. The closed circles represent numerical results, and the solid curves are the results obtained analytically from relationship (24). Figure 2 demonstrates the dependence of the period of the ion acoustic wave, $T = 2\pi/\Omega$, on $|\varepsilon|_0$ at the instability threshold, calculated numerically and obtained analytically from solutions (23). The dependence of the length of the BPD region, $l - \zeta_1$, on the microwave field amplitude at the entrance to the system is given in Fig. 3.

Figures 1 and 2 show that numerical results agree well with analytical predictions. As is clear from a comparison of these figures with Fig. 3, we did not carry out numerical simulations for a very short BPD region, because, in this case, the amount of computer time required to achieve satisfactory accuracy is unreasonably large. Good agreement between numerical and analytical results obtained even for a comparatively long source region, $l - \zeta_1 \leq 1$, is explained by the fact that, for $\gamma = 0$, the next term in the expansion in the discharge length that was used to derive dispersion relation (23) and relationship (24) is of the third (rather than second) order.

Figure 4 shows a typical time dependence of the output signal amplitude $|\varepsilon|(l)$ in the self-modulation regime near the instability threshold. The dependence is seen to be slightly aperiodic, the characteristic time scale being much longer than the period of the ion acoustic wave. Such behavior may be associated with the nonlinear corrections that were neglected in the previous section, in particular, those introduced by the region $\zeta_1 < \zeta < \zeta_3$, whose existence is attributed to the threshold nature of the BPD and whose length in the self-modulation regime varies periodically with time.

5. CONCLUSIONS

Our theoretical calculations show that, because of the development of the BPI during the injection of an electron beam into a homogeneous plasma containing a neutral component, the amplitude of the excited microwave evolves to a steady-state, axially nonuniform distribution. Initially, the BPD that develops near the right boundary of the waveguide structure increases the plasma density but does not change its uniform distri-

bution or the steady character of the amplification regime. As the neutral gas pressure or the beam current increases, the steady-state regime of the amplification of the excited microwave becomes unstable and changes to the self-modulation regime.

The change of the amplification regime is associated with the plasma density perturbations that originate in the BPD region, propagate in the direction opposite to that of the beam, and affect the conditions for the generation of microwaves, thereby changing the microwave field amplitude in the region where they originated. Because of such an influence of the plasma nonlinearity, the beam instability gives rise to a new effect—distributed delayed feedback, which causes the microwave amplifier to operate simultaneously as a generator of low-frequency plasma oscillations.

ACKNOWLEDGMENTS

We are grateful to the anonymous referee for valuable remarks about the role of elastic collisions in the development of a beam–plasma discharge. One of the authors (Yu.P. Bliokh) also acknowledges financial support from the Center for Absorption in Science, the Ministry of Immigrant Absorption, State of Israel.

REFERENCES

1. V. E. Zakharov, Zh. Éksp. Teor. Fiz. **62**, 1745 (1972) [Sov. Phys. JETP **35**, 908 (1972)].
2. E. A. Kuznetsov, Fiz. Plazmy **2**, 327 (1976) [Sov. J. Plasma Phys. **2**, 178 (1976)].
3. Yu. P. Bliokh, Ya. B. Fainberg, M. G. Lyubarskii, and V. O. Podobinskii, in *Proceedings of SPIE on Intense Microwave Pulses, San Diego, CA, 1997*, Vol. 3158, p. 182.
4. Yu. P. Bliokh, Ya. B. Fainberg, M. G. Lyubarsky, *et al.*, Phys. Plasmas **5**, 4061 (1998).
5. K. Yu. Bliokh, Yu. P. Bliokh, M. G. Lyubarsky, and V. O. Podobinsky, Izv. Vyssh. Uchebn. Zaved., Prikl. Nelin. Dinam. **7**, 29 (1999).
6. Yu. P. Bliokh, M. G. Lyubarsky, G. S. Nusinovich, and V. O. Podobinsky, Izv. Vyssh. Uchebn. Zaved., Prikl. Nelin. Dinam. **7**, 56 (1999).
7. Yu. P. Bliokh, N. M. Zemlyansky, M. G. Lyubarsky, *et al.*, Fiz. Plazmy **29**, 336 (2003) [Plasma Phys. Rep. **29**, 307 (2003)].
8. M. A. Miller, Izv. Vyssh. Uchebn. Zaved., Radiofiz. **1**, 110 (1958).
9. A. N. Antonov, Yu. P. Bliokh, E. A. Kornilov, *et al.*, Fiz. Plazmy **26**, 1097 (2000) [Plasma Phys. Rep. **26**, 1027 (2000)].
10. Yu. P. Bliokh, N. M. Zemlyansky, M. G. Lyubarsky, *et al.*, Scientific and Technical Report on Project UNTTs, No. 277, 81 (1997).
11. Yu. V. Bobylev, M. V. Kuzelev, and A. A. Rukhadze, Zh. Éksp. Teor. Fiz. **118**, 105 (2000) [JETP **91**, 93 (2000)].
12. E. A. Kornilov, E. A. Lutsenko, N. S. Pedenko, *et al.*, Zh. Éksp. Teor. Fiz. **38**, 685 (1960) [Sov. Phys. JETP **11**, 493 (1960)].

Translated by I.A. Kalabalyk

Plasma Physics Reports, Vol. 29, No. 9, 2003, pp. 748–756. Translated from Fizika Plazmy, Vol. 29, No. 9, 2003, pp. 809–817.

PLASMA DYNAMICS

Formation of a Z-Pinch during Electromagnetic Compression of a Nonquasineutral Current Filament

A. V. Gordeev* and T. V. Losseva**

**Russian Research Centre Kurchatov Institute, pl. Kurchatova 1, Moscow, 123182 Russia*

***Institute of Geosphere Dynamics, Russian Academy of Sciences, Leninskiĭ pr. 38-1, Moscow, 119334 Russia*

Received November 21, 2002; in final form, March 18, 2003

Abstract—A study is made of the structure of a relativistic current filament with the azimuthal magnetic field B_θ in the range $4\pi n_e m_e c^2 \ll B_\theta^2 \ll 4\pi n_i m_i c^2$, when the plasma quasineutrality near the filament axis is violated and a narrow peak in electron density is formed there. The ion dynamics in a strong radial electric field of the filament on time scales of about several inverse ion plasma frequencies ω_{pi}^{-1} is investigated. The initial ion pressure prevents the ion plasma component from compression to infinitely high densities under the action of the electric field and leads to the formation of a dense hot plasma core near the axis of the Z-pinch on time scales of about a dozen ω_{pi}^{-1}. The compression of the ion component in the axial region gives rise to a collisionless "unloading" shock wave that propagates away from the axis and is accompanied by the vanishing of the radial ion velocity behind the shock front, the accumulation of positive charge near the axis, and the formation of a steady-state ion density profile. It is shown theoretically that ion–ion dissipation manifests itself as the destruction of the hot core of the formed Z-pinch on picosecond time scales. This may serve to explain the explosions of "hot points" in a current-carrying plasma. © *2003 MAIK "Nauka/Interperiodica".*

1. In recent years, interest has grown in systems with Z-pinches that make it possible to achieve high X-ray intensities and large neutron yields. The experimentally obtained characteristic dimensions of the emitting regions were found to be somewhat less than 0.1 cm, and their characteristic lifetimes were on the order of 10^{-8} s [1–4]. Recent space- and time-resolved measurements have shown that reproducible processes in Z-pinches occur on spatial scales of about 10^{-4} cm and time scales of about 3×10^{-12} s [5–7]. Theoretical analysis performed for this range of scales consists mainly of laborious numerical calculations in which not only electrodynamic processes but also radiation and various dissipative effects in the plasma are taken into account [7, 8]. Meanwhile, to gain insight into the phenomena occurring on very short spatial and time scales, when most of the dissipative processes play an equally important role, it is, first of all, necessary to have a clear understanding of the electrodynamic processes accompanying electron and ion motions in strong electric and magnetic fields [9]. The initial stage of gas breakdown is dominated by the electric field E_z, which drives and maintains the ohmic current $j_z = \sigma E_z$. However, as the magnetic field B_θ grows and the dimensionless Hall parameter increases to large values, $\sigma B_\theta / e n_e c \gg 1$, the role of the dissipative processes decreases. Moreover, in this stage, the electrons can form current-carrying filaments on time scales on the order of ω_{pe}^{-1} by the Weibel mechanism for generating a quasistatic magnetic field due to the anisotropy of the electron motion [10]. The physical processes governing the formation and subsequent evolution of current filaments were investigated by present-day computational means in a recent paper by Sakai *et al.* [11]. The characteristic radius of the electron current filaments calculated in that paper is on the order of the magnetic Debye radius $r_B \sim B_\theta / 4\pi e n_e$, which confirms the possibility of the existence of electron current structures during the evolution of a pulsed current-carrying plasma. A distinctive feature of such current structures is the violation of plasma quasineutrality and the generation of a strong Hall electric field E_r on a spatial scale of about r_B (see [12–14]), on which the electrons within the filament drift along the z axis in crossed electric (E_r) and magnetic (B_θ) fields, thereby producing the filament current in the absence of dissipation. In this case, the radial drop in the electric potential across such a "capacitor" is substantially higher than the potential difference between the electrodes. Measurements show that the Z-pinch starts to emit electromagnetic radiation and neutrons in the stage in which the voltage at the electrodes drops considerably; moreover, the characteristic electron energy in the electron beams observed experimentally can be higher than the applied voltage [1]. In such a nonquasineutral electron filament, the compression of the ion plasma component on a time scale of about ω_{pi}^{-1} by the inwardly directed radial electric field gives rise to a nonlinear unloading wave that propagates away

1063-780X/03/2909-0748$24.00

from the axis and in which the radial ion velocity vanishes due to the accumulation of hot ions in the core of the Z-pinch according to a certain effective adiabatic law.

2. In order to describe a nonquasineutral electron current structure, we use a set of basic equations consisting of the hydrodynamic equation of electron motion converted into the form (see [13])

$$\frac{\partial \mathbf{p}_e}{\partial t} + \nabla \gamma m_e c^2 = -e\mathbf{E} - \frac{e}{c}\mathbf{v}_e \times \mathbf{\Omega}_e, \qquad \mathbf{\Omega}_e = \mathbf{B} - \frac{c}{e}\nabla \times \mathbf{p}_e \tag{1}$$

and Maxwell's equations

$$\nabla \times \mathbf{B} = \frac{4\pi e}{c}(Zn_i\mathbf{v}_i - n_e\mathbf{v}_e) + \frac{1}{c}\frac{\partial \mathbf{E}}{\partial t}, \tag{2}$$

$$\nabla \cdot \mathbf{E} = 4\pi e(Zn_i - n_e). \tag{3}$$

Here, m_e is the mass of an electron, $\mathbf{v}_e$ is the electron velocity, $\mathbf{p}_e = \gamma m_e \mathbf{v}_e$ is the electron momentum, $\gamma = 1/\sqrt{1 - \mathbf{v}_e^2/c^2}$ is the relativistic factor, n_e is the electron density, and $\mathbf{E}$ and $\mathbf{B}$ are the electric and magnetic fields.

Taking the curl of Eq. (1) and using the continuity equation for the electrons, we obtain the following equation for the Lagrangian invariant I:

$$\frac{\partial I}{\partial t} + \mathbf{v}_e \cdot \nabla I = 0, \quad I = \frac{\Omega_{e\theta}}{rn_e}. \tag{4}$$

The ion dynamics is described by the hydrodynamic equations

$$\frac{\partial n_i}{\partial t} + \nabla \cdot (n_i \mathbf{v}_i) = 0, \qquad m_i \frac{d\mathbf{v}_i}{dt} = Ze\mathbf{E} + \frac{Ze}{c}\mathbf{v}_i \times \mathbf{B} - \frac{1}{n_i}\nabla p_i, \tag{5}$$

where n_i, $\mathbf{v}_i$, and p_i are the ion density, velocity, and pressure, respectively.

Of course, the question may then be raised about the applicability of the hydrodynamic approach under such extreme conditions. Estimates show that the ions are decelerated primarily because they lose their energy in collisions with electrons; consequently, the ion mean free path $l_i \sim \tau^{i/e}|\mathbf{v}_i|$ can serve as a characteristic spatial scale in related physical problems (see Section 7). In our simulations, collisions were neglected; however, Sagdeev [15] already pointed out that, under conditions like those in the highly nonquasineutral plasma under consideration, a collisional shock wave can form on the spatial scale r_B [13]. In numerical calculations for the problem as formulated, the formation of steep fronts of the ion density and velocity in an unloading wave is undoubtedly associated with the violation of plasma quasineutrality at the wave front. Note that, for the parameters of the problem at hand, these spatial scales are on the same order of magnitude.

The above equations allow us to investigate the plasma dynamics in the following range of magnetic fields:

$$4\pi n_e m_e c^2 \ll B_\theta^2 \ll 4\pi n_i m_i c^2. \tag{6}$$

The left-hand inequality reflects the basic assumption that an electron current structure with a characteristic spatial scale on the order of the magnetic Debye radius $r_B \sim B/4\pi e n_e$ is nonquasineutral. As will be seen below, the characteristic time scale is the inverse ion plasma frequency $t_0 \sim \omega_{pi}^{-1}$. The right-hand inequality introduces the small parameter $\varepsilon = r_B/ct_0 \ll 1$, which indicates the quasistatic approximation for electrons and makes it possible to neglect the time-dependent term in Eq. (1) and to remove from consideration the ion motion on a scale of $r \sim r_B$ along the z axis.

It is important to stress here that the structure of the electron current filaments under discussion differs substantially from the fine structure of filaments that was calculated numerically in [11]. In that paper, the total current in the filaments produced by an electron beam propagating in a plasma is zero because, on very short time scales, the current of fast beam electrons generates a return current, which is able to flow in the absence of dissipation for a fairly long time. In the approach developed here, it is assumed that, although return current is initially generated by the current flowing in a filament (at the expense of the applied electric field E_z), it dissipates on comparatively short time scales. As a result, only the current flowing in the direction of the applied field remains within the filament. Estimates show that, under conditions in which the initial electric conductivity is fairly low, the return current on micron scales is dissipated sufficiently rapidly. It is because of the absence of the return current that, in our model, the filament does not expand and the ions are not accelerated toward the filament periphery, in contrast to the numerical results presented in [11]. However, despite the above differences between the two approaches, the characteristic radius of the electron filaments calculated in [11] turns out to be approximately equal to the magnetic Debye radius, which can be estimated as $r_B \simeq c/\omega_{pe}\sqrt{\varepsilon_i/(m_e c^2)}$, where ε_i is the calculated energy of the accelerated ions.

3. The generation of magnetic fields in laser plasmas has been investigated in many papers (see [16] and the references therein). In some studies, the electron vorticity

$$\mathbf{\Omega}_e \equiv \mathbf{B} - \frac{c}{e}\nabla \times \mathbf{p}_e \tag{7}$$

was assumed to be zero throughout the entire plasma evolution [16]. This indicates that the vortex structure

cannot form, because $\mathbf{\Omega}_e \equiv 0$. In this limit, the vortices cannot exist in the plasma and helicon perturbations cannot propagate in it. In principle, the conservation of the electron vorticity $\mathbf{\Omega}_e$ can be disturbed by many mechanisms. The most generally accepted mechanism is that proposed by Weibel [10], who took into account the electron pressure anisotropy induced by a high-power electromagnetic wave whose electric field accelerates the electrons. In the nonrelativistic limit, the hydrodynamic equation for the electron plasma component with a nonzero pressure (but without dissipation) can be represented as

$$m_e \frac{d\mathbf{v}_e}{dt} = -e\mathbf{E} - \frac{e}{c}\mathbf{v}_e \times \mathbf{B} - \frac{1}{n_e}\nabla p_e. \quad (8)$$

Taking the curl of Eq. (8) and using the induction equation, we can obtain

$$\frac{\partial \mathbf{\Omega}_e}{\partial t} - \nabla \times (\mathbf{v}_e \times \mathbf{\Omega}_e) = \nabla \times \left(\frac{1}{n_e}\nabla p_e\right). \quad (9)$$

Hence, if p_e depends not only on n_e but also on some other parameters (in the case of the Weibel mechanism, it is necessary to take into account the pressure anisotropy); then, according to Eq. (9), the vorticity becomes nonzero and vortex structures may be generated.

For further analysis, it is important to emphasize that there are two essentially different types of vortex structures: (i) structures with azimuthal electron currents j_θ, in which the magnetic field is aligned with the z axis ($\mathbf{B} = \mathbf{e}_z B_z$) and (ii) structures with longitudinal electron currents j_z, which produce an azimuthal magnetic field B_θ. Our investigations show that the electron density in these two types of vortex structures behaves in radically different ways. In vortex structures with azimuthal electron currents, the electron density near the axis is low, so that the axial plasma region of the structure is charged positively. As a result, the plasma ions fly apart in the radial direction toward the periphery of the structure [13]. In contrast, in a vortex structure with a longitudinal electron current and an azimuthal magnetic field B_θ, the electron density at the axis is maximum and the axial plasma region is charged negatively, so that the ion plasma component collapses toward the axis, giving rise to a Z-pinch [9].

Note that, for electron structures with azimuthal electron currents, Berezhiani *et al.* [16] revealed that, when $\mathbf{\Omega}_e = 0$, the electron density at the axis is depressed, as is the case when $\mathbf{\Omega}_e \neq 0$ [13].

Since, at $\mathbf{\Omega}_e \neq 0$, the objects in question (i.e., vortex structures with an azimuthal magnetic field B_θ) are, in fact, current filaments, we will use this traditional term for them in our analysis.

4. In what follows, an electron filament is considered to be a quasisteady formation on time scales much shorter than the characteristic time ω_{pi}^{-1} of the evolution of the ion plasma component. From electron equations (1)–(3), the potential of an electron current filament can be estimated as $U \sim J/c$ (where J is the current on the spatial scale r_B within the filament) [14]. Even for currents of about $J \sim 100$ kA, this yields a potential in excess of one megavolt.

Using the dimensionless formulas describing electron equilibrium [see formulas (16) and (17) below], we can obtain the following expression for the absolute value of the dimensionless potential φ_0 at the axis of a current filament:

$$|\varphi_0| = 1 - \gamma_0 + \frac{2i_0}{\rho_0^2}\int_0^\infty \frac{b\rho^2 d\rho}{\left(1 + \dfrac{\rho^2}{\rho_0^2}\right)^2}. \quad (10)$$

Here, the potential at infinity is assumed to be zero, the ions are assumed to be immobile, and the dimensionless Lagrangian invariant i at the initial instant has the form

$$i = \frac{i_0}{1 + \dfrac{\rho^2}{\rho_0^2}}, \quad (11)$$

where ρ_0 is the characteristic spatial scale of the current filament structure. For calculations, we chose the value $\rho_0 = 3$. In expression (10), the relativistic factor of the electrons at the axis, γ_0, determines the height of the peak in the electron density in the axial region, $\nu_0 = \gamma_0^2$.

Calculations carried out on the basis of expression (10) for two initially equilibrium filaments with the currents $J_1 = 153$ kA and $J_2 = 191$ kA yielded the following two values of the potential at the axis: $U_1 = -6.0$ MV and $U_2 = -9.1$ MV. That the values of the potential are so high is confirmed to some degree by the experimental results of [4], where, at a total current of $J \sim 400$ kA, ions with an energy of about 1 MeV were recorded by measuring the Doppler shift of their spectral lines. These values of the potential in the filament also correlate with the numerical results obtained in [11], where the ions were found to be accelerated to energies of several MeV.

It is also instructive to present the maximum magnetic field strengths b_{max} in electron filaments at different values of γ_0. Figure 1 shows the dependence $b_{max}(\gamma_0)$ calculated for a wide range of γ_0 values. We can see that the relativistic factor of the electrons γ_0 at the axis increases with the magnetic field in the filament. (We note that a similar dependence for the case with $\mathbf{\Omega}_e = 0$ was found in [16].) As a result, the electron–ion collisions in the system are in fact "switched off" and, simultaneously, the radiation emitted by the evolving filament becomes far less intense.

5. The basic equations describing a quasistatic current structure can be derived by exploiting the small-

ness of the parameter $\varepsilon = r_B/ct_0 \ll 1$. To do this, we utilize, together with Eq. (1), the drift equation

$$\mathbf{E} + \frac{1}{c}(\mathbf{v}_e \times \mathbf{B}) = 0, \tag{12}$$

which is valid for $\varepsilon = r_B/ct_0 \ll 1$. We estimate the displacement current using Eq. (12) and exploit the condition that the structure is quasistatic to obtain from Eq. (2) the relationship

$$v_{ez} = -\frac{c}{4\pi e n_e r}\frac{\partial}{\partial r}(rB_\theta). \tag{13}$$

The definition of the vorticity component $\Omega_{e\theta}$ gives

$$\gamma^3\frac{\partial v_{ez}}{\partial r} = \frac{e}{m_e c}(\Omega_{e\theta} - B_\theta). \tag{14}$$

Then, we express the electric field component E_r from Eq. (12), insert it into Eq. (3), and take the derivatives in the resulting equation. Finally, using relationship (13), Eq. (14), and definition (4) for I, we arrive at the following expression for n_e:

$$n_e\left(\gamma + \frac{rB_\theta I}{4\pi m_e c^2}\right) = \gamma^3 Z n_i + \frac{B_\theta^2}{4\pi m_e c^2}. \tag{15}$$

We introduce the dimensionless quantities

$$r = \rho\sqrt{\frac{m_e c^2}{4\pi e^2 n_\infty}}, \quad B_\theta = b\sqrt{4\pi m_e c^2 n_\infty},$$
$$v_{ez} = cv, \quad n_e = n_\infty\nu, \quad n_i = \frac{n_\infty}{Z}n, \quad I = 4\pi e i, \tag{16}$$

in terms of which we obtain the set of equations describing a quasistatic electron current structure (see also [13]):

$$\frac{1}{\rho}\frac{\partial}{\partial\rho}(\rho b) = -\nu v, \quad \gamma^3\frac{\partial v}{\partial\rho} = \rho\nu i - b,$$
$$\nu = \frac{n\gamma^3 + b^2}{\gamma + \rho i b}. \tag{17}$$

As can be seen from these equations, the filament structure at a given ion density n is completely determined by the profile of the Lagrangian invariant i. Since the equilibrium of plasma electrons is quasistatic, the dependence on time in Eqs. (17) is parametric.

In this formulation of the problem, the dynamics of the structure is governed by the relatively slow ion motion in an electric field. In the ion hydrodynamic equations (5) of our model, only the radial motion of the ions is taken into account, because the right-hand inequality in conditions (6) allows us to ignore the ions moving in the z direction. The corresponding terms in the equation for radial ion motion turn out to be on the order of ε^2, where $\varepsilon = r_B/ct_0 = \sqrt{Zm_e/m_i}$. All of the quantities are assumed to depend only on the radial coordinate r; hence, the kink instabilities and sausage-type instabilities are excluded from consideration. By virtue of the symmetry properties of our problem, the electron velocity, which enters Eq. (4) for the Lagrangian invariant I, is expressed from Eq. (2) as follows:

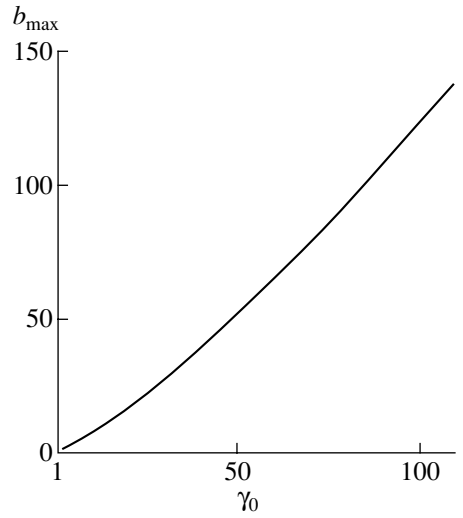

Fig. 1. Dependence of the maximum dimensionless magnetic field $b_{\max}$ on the relativistic factor γ_0 of the electrons at the axis of the filament.

$$v_{er} = \frac{Zn_i}{n_e}v_{ir} + \frac{1}{4\pi e n_e}\frac{\partial E_r}{\partial t}. \tag{18}$$

With the corresponding nondimensionalization procedure, we arrive at the following time-dependent dimensionless equations, which enable us to close the set of equations (17) and to determine the time-varying ion density n and the values of the Lagrangian invariant i:

$$\frac{\partial n}{\partial\tau} + \frac{1}{\rho}\frac{\partial}{\partial\rho}(\rho n u) = 0,$$
$$\frac{\partial u}{\partial\tau} + u\frac{\partial u}{\partial\rho} = -\frac{\partial\gamma}{\partial\rho} - i\frac{\partial}{\partial\rho}(\rho b) - \frac{1}{n}\frac{\partial p}{\partial\rho}, \tag{19}$$

$$\frac{\partial i}{\partial\tau} + \left[\frac{n}{\nu}u + \frac{1}{\nu}\frac{\partial}{\partial\tau}\left(\frac{\partial u}{\partial\tau} + u\frac{\partial u}{\partial\rho} + \frac{1}{n}\frac{\partial p}{\partial\rho}\right)\right]\frac{\partial i}{\partial\rho} = 0. \tag{20}$$

Here, we have introduced the dimensionless time τ and dimensionless radial ion velocity and pressure:

$$t = \tau\sqrt{\frac{m_i}{4\pi e^2 Z n_\infty}}, \quad v_{ir} = uc\sqrt{\frac{Zm_e}{m_i}},$$
$$p_i = pn_\infty m_e c^2, \quad p = \lambda\frac{n^2}{2}. \tag{21}$$

The initial conditions on Eqs. (19) and (20) are $n(\tau = 0) = 1$ and $u(\tau = 0) = 0$, and the boundary conditions for these quantities are $n(\rho = \infty) = 1$ and $u(\rho = 0) =$

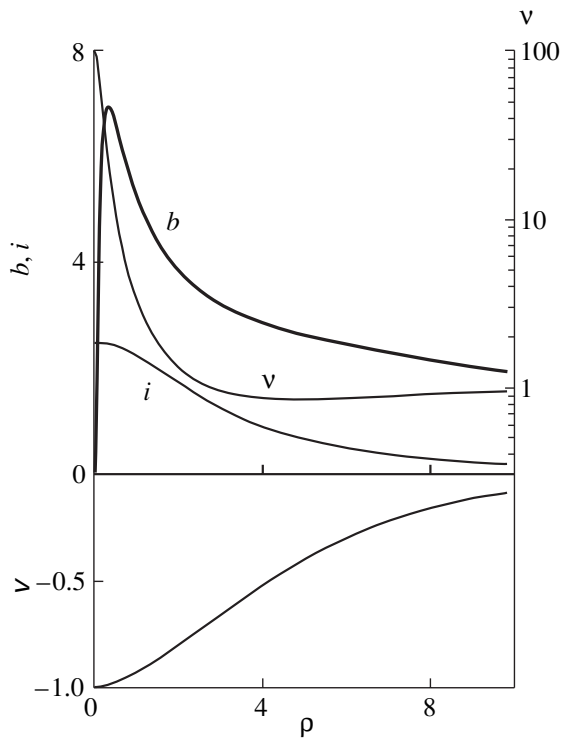

Fig. 2. Profile of the Lagrangian invariant i for a filament with the current J_2 = 191 kA and calculated profiles of the magnetic field b, electron density ν, and electron velocity v.

$u(\rho = \infty) = 0$. The adiabatic index was chosen to be equal to 2. Calculations were carried out for several values of λ, corresponding to different initial ion pressures. Note that the choice of the adiabatic law in accordance with relationships (21) is somewhat incorrect because the pressure at infinity is certainly equal to zero. However, in the case at hand, this choice does not lead to contradictions, because the formulas contain the derivatives of the pressure p and because, for the region where $n \gg 1$, this choice of the adiabatic law is quite fair.

Equations (17), (19), and (20) can be divided into two sets. (i) The first set of ordinary differential equations (17) was used to calculate a steady electron vortex in an azimuthal magnetic field by finding the functions b, v, and ν from their solution at given n and i. (ii) The second set of time-dependent partial differential equations (19) and (20) was used to follow the evolution of the ion plasma component and Lagrangian invariant i by calculating the transport of the quantities n, u, and i with the corresponding rates. Equations (17) were integrated by the Gear method. Among the integral curves that originate from the singular point $r = 0$, which is a removable singularity, the curves that satisfy the boundary conditions at $r \longrightarrow \infty$ were chosen by adjusting the value of ν at $r = 0$. Equations (19) and (20) were integrated by a version of the Boris–Book method, specifically, the LCPFCT version [17], which is the modification of the nonlinear flux-corrected transport (FCT) algorithm, ensuring that the solution will always be monotonic and positive. In numerical integration of the equations of ion motion by the LCPFCT algorithm, the artificial viscosity resulted implicitly from the use of a controlled antidiffusive correction.

6. Figure 2 illustrates the initial equilibrium of an electron current structure with unperturbed ions. We can see that the electron density in the initial state is peaked near the axis of the structure. The peak produces a radial electric field directed toward the axis. The relativistic electron motion in the z direction generates an azimuthal magnetic field, in which case the electrons drift in crossed electric and magnetic fields. Such a filament is a universally encountered formation, whose structure changes due to the slow motion of unmagnetized ions in its electric field [9, 13]. The numerical results obtained in [11] confirm fairly well the validity of the model used in our simulations. The characteristic radius of the filaments was calculated to be on the order of r_B, which agrees with the estimates obtained for the parameters adopted in that paper.

Figure 3 shows time evolutions of the density n and velocity u of the ions moving in a radial electric field in the initial stage of development of the current filament. We can see that accelerated ions moving from the periphery are decelerated by the pressure gradient of the ions that have been accumulated in the dense hot core near the axis. Figure 3 implies that, at the beginning of the process (on time scales τ from about 0.2 to 0.5), the profile of the ion density has already steepened and a discontinuity has appeared. As a result, after the time $\tau = 0.3$, the forming unloading wave in which the radial ion velocity vanishes has a steep front, at which the accelerating electric field and decelerating pressure gradient cancel one another. This front, which has become flatter already on time scales $\tau \simeq 0.7$–1, propagates toward the periphery, leaving behind an essentially immobile, dense hot core. A comparison of the profile of the dimensionless electric field, $e(\rho)$, with a narrow peak in the profile of the decelerating force, $(1/n)\partial p/\partial\rho$, shows that the wave front occurs between the two surfaces whose radii are determined by the intersections of the profiles, $e(\rho) = (1/n)\partial p/\partial\rho$. Figure 3 shows that, at a time of about $\tau \sim 0.5$, positive ion charge starts to be accumulated within the wave front, thereby weakening the electric field therein. Presumably, it is because of the weakening of the electric field (and, accordingly, the decrease in the electron drift velocity) that the front of the unloading wave propagating toward the periphery divides the electron-drift region into two parts and forms an advancing "cloud" of drifting electrons (Fig. 4). In this case, the front of the increasing ion density profile and the front of the velocity profile of the decelerated ions in the wave propagating away from the axis occur just at the minimum (which falls to zero on longer time scales) of the absolute value of the electron velocity.

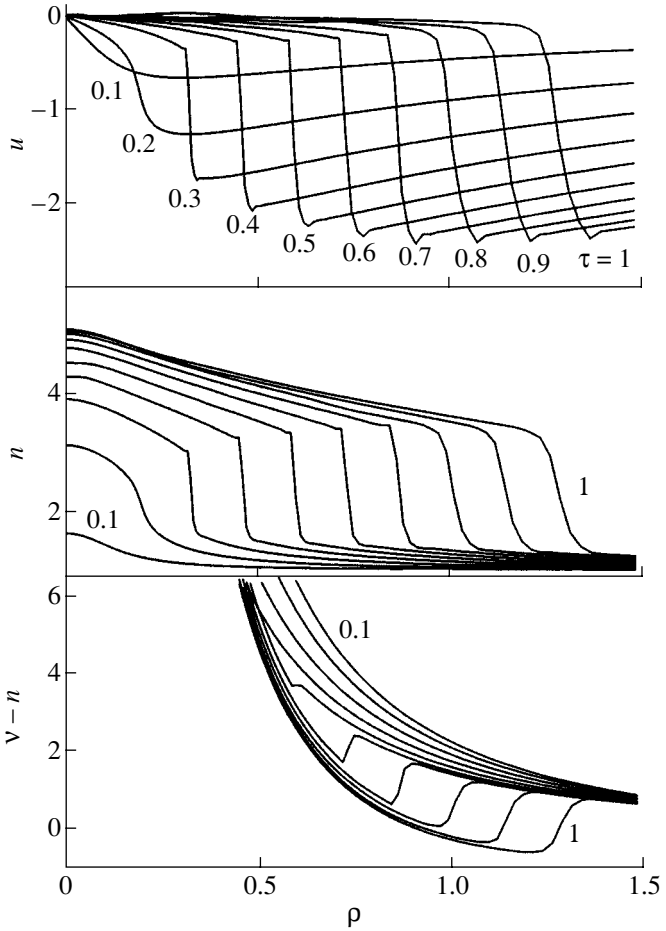

Fig. 3. Formation of a collisionless unloading shock wave within a current filament in the initial stage of deceleration of the inwardly accelerated ions by the pressure gradient in the dense core of a Z-pinch.

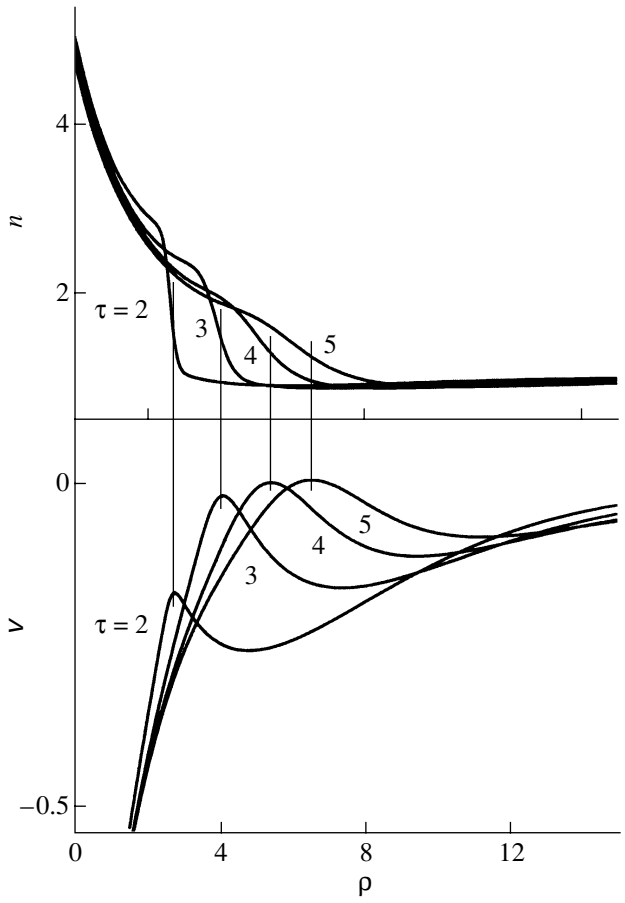

Fig. 4. Evolution of a cloud of drifting electrons ahead of the front of a nonlinear unloading wave propagating away from the axis of the filament.

Recall that, as a nonlinear unloading wave propagates toward the periphery, the profiles of all the quantities in the wave become flatter on time scales of $\tau > 1$. Consequently, the wave in this propagation stage can be interpreted merely as a nonlinear unloading wave. The ion density and ion velocity profiles in this nonlinear wave on long time scales are shown in Fig. 5.

Figure 6 displays the ion density as a function of both the current flowing in the filament and the initial ion pressure. One can see that, as the current J increases and the initial temperature [which is described by the dimensionless parameter λ, see relationships (21)] decreases, the ion density near the axis becomes higher. An increase in the steady-state ion density at the axis with decreasing λ agrees with the experimental results of [5].

As time progresses, the nonlinear unloading wave propagating toward the periphery becomes less intense and an equilibrium plasma structure with hot ions is formed. The ions in this structure are kept at equilibrium by magnetic and electric fields on a spatial scale on the order of r_B.

The Z-pinch configuration obtained above results from electrodynamic compression of the ion plasma component. The equilibrium state in which the configuration is maintained is described by the integral relationship

$$r^2(B_\theta^2 - E_r^2) + 8\pi\int_0^r dr r^2 \frac{\partial p_i}{\partial r} = 0, \qquad (22)$$

which implies that not only the magnetic but also the electric field plays an important role.

Our numerical calculations show that, e.g., for a 1-cm-long Z-pinch, carrying the current $J_2 = 191$ kA, the energy transferred to the ions (primarily from the magnetic field) does not exceed 2–3 J (see also [4]). Thus, the characteristic amount of the energy transferred and the spatial and time scales of the processes in a micropinch with a current of about several hundred kiloamperes are found to be very close to those in a

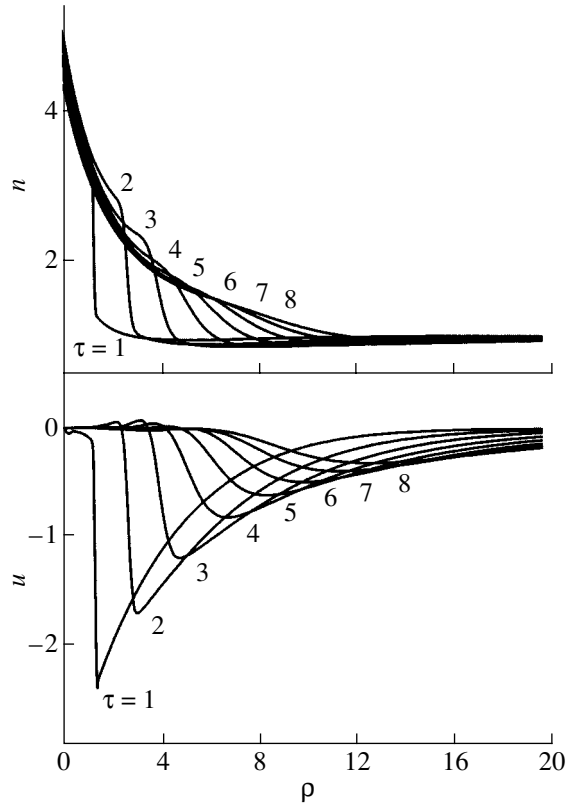

Fig. 5. Calculated profiles of the ion density n and ion velocity u within an unloading wave at successive times τ (in units of ω_{pi}^{-1}) for the current $J_2 = 191$ kA.

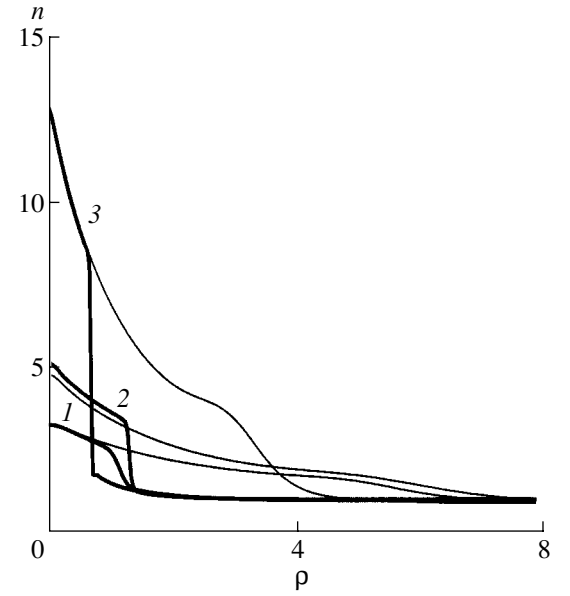

Fig. 6. Density profiles within an unloading wave for different currents J and different initial pressures λ: (*1*) $J_1 = 153$ kA and $\lambda = 1$, (*2*) $J_2 = 191$ kA and $\lambda = 1$, and (*3*) $J_2 = 191$ kA and $\lambda = 0.1$. The heavy curves are the density profiles at the time $\tau = 1$.

laser plasma produced by a focused laser pulse with an intensity of 10^{19} W/cm^2 [18]. However, it should be kept in mind that, in the problem of ion acceleration by laser radiation, nonquasineutral plasma dynamics in a quasistatic magnetic field [13, 11] is as important as the direct action of the ponderomotive pressure force [18].

On longer time scales, the plasma structure is expected to evolve to an almost quasineutral equilibrium state.

7. In the system under consideration, collisions between particles give rise to dissipation of the electromagnetic field energy and lead to additional heating. As a result, an equilibrium configuration to which the system has evolved should be destroyed. Because of the above-mentioned "switching-off" of the electron–ion collisions, ion–ion collisions begin to play an important role [19]. Consequently, there exists a parameter range in which ion–ion dissipation dominates even when the electron and ion temperatures are comparable:

$$|\mathbf{v}_1 - \mathbf{v}_2| \gg \left(\frac{m_e}{Z^2 m_i}\right)^{1/4} \frac{|\mathbf{j}|}{en_e}. \tag{23}$$

In this case, electron–ion collisions may be important only when

$$\frac{Z_1}{M_1} \neq \frac{Z_2}{M_2}, \tag{24}$$

where Z_1 and Z_2 are the charge numbers of different ion species and M_1 and M_2 are their masses.

The relative velocity of the ion species, $|\mathbf{v}_1 - \mathbf{v}_2|$, which governs the magnetic field diffusion, can be significant only when fast inertial ion motion is taken into account. Such motion is accompanied by the spatial separation of the ion species. Now, we consider how the magnetic field in the equilibrium system analyzed above evolves under the action of ion–ion collisions. According to [19], the magnetic field evolution is described by the equation

$$\frac{\partial B_\theta}{\partial t} + \frac{\partial}{\partial r}(v_{ir} B_\theta) = \frac{c^2}{4\pi}\frac{\partial}{\partial r}\left[\frac{(\eta_1\xi_2 - \eta_2\xi_1)^2}{\xi_1\xi_2}\frac{h^2}{1+h^2}\frac{1}{r\sigma}\frac{\partial}{\partial r}(rB_\theta)\right], \tag{25}$$

where η_k and ξ_k are the relative mass and charge of the ion species ($k = 1, 2$), $h = \sigma B_\theta/(en_e c)$, and $\sigma(T_i)$ is the conductivity due to ion–ion collisions. Under the inequality

$$|\mathbf{v}_i| \gg |\mathbf{v}_1 - \mathbf{v}_2| \tag{26}$$

(where $\mathbf{v}_i = \eta_1\mathbf{v}_1 + \eta_2\mathbf{v}_2$ is the mass velocity), the quantities η_k and ξ_k may be considered constant. Here, we assume that the ion temperature is equalized sufficiently rapidly, so that the conductivity $\sigma(T_i)$ can also be regarded constant.

It is easy to see that, in terms of the variable $\zeta = r^2/t$, Eq. (25) can be represented in a self-similar form describing the magnetic energy dissipation. Then, we take into account hydrodynamic equations analogous to Eqs. (5), namely, those that were derived in [19] for a multicomponent plasma, and assume that $h = h(\zeta)$. As a result, for a quasineutral plasma, we obtain

$$n_e = t^{-1}N(\zeta), \quad B_\theta = t^{-1}B(\zeta), \quad v_{ir} = t^{-1/2}V(\zeta). \quad (27)$$

Therefore, when ion–ion dissipation comes into play, the compression stage should be followed by the stage in which the quasineutral edge plasma of the heated core expands radially and the density and magnetic field both rapidly decrease. Ion–ion dissipation becomes important under condition (23), which yields the inequality $h > (m_e/Z^2m_i)^{1/4}$ [19], corresponding to an ion temperature of $T_i \sim 10$ keV at an electron density of $n_e \sim 10^{23}$ cm^{-3}. A dense hot core with a radius of about $r \sim 10^{-4}$ cm expands dissipatively on time scales on the order of 10^{-12} s, while the time scales of the expansion due to electron–ion dissipation are two orders of magnitude longer.

Note that, in actual plasma experiments, the expansion stage is preceded by a stage in which collapsing plasma ions are decelerated by the electrons and which occurs on time scales shorter than 10^{-12} s. Although, in our study, collisions between particles are neglected, it is expedient to carry out the following simple estimate. In the electric field of the filament under consideration, the ions acquire an energy of about several MeV and lose it mainly due to the deceleration by electrons on a characteristic time scale of [20]

$$\tau^{i/e} \approx \frac{m_e}{m_i}\frac{\sqrt{m_e}\varepsilon_i^{3/2}}{\pi\sqrt{2}Z^2e^4\Lambda n_e}, \quad (28)$$

where Λ is the Coulomb logarithm.

We substitute the electron density typical of experiments [5–7] into formula (28) and take into account the fact that such experiments are usually carried out with heavy ions with masses of about $m_i \sim 10^2 m_p$ (where m_p is the proton mass) and charge numbers of $Z \geq 10$. As a result, we find that the ions are decelerated on a time scale shorter than 10^{-12} s; in this case, their characteristic mean free path is shorter than 10^{-4} cm (which is just the characteristic radius of the Z-pinch, $r_B = B_\theta/4\pi en_e$) at currents of about several hundred kiloamperes.

Presumably, further evolution of the Z-pinch proceeds through the equalization of the electron and ion temperatures and the cooling by emission of radiation [5–7].

8. Hence, we have shown that a universal nonquasineutral electron current structure (filament) may exist in an azimuthal magnetic field, where the charge-separation electric field produces an electron drift current, which self-consistently maintains the magnetic field of the filament. The electric field accelerates the ions with a given initial pressure, leading to the formation of a dense hot plasma core in the Z-pinch. As a result, the pinch evolves to an equilibrium state governed by the accumulation of positive ion charge near the axis. Analytic estimates show that taking into account ion–ion collisions results in a self-similar expansion of the hot core of the Z-pinch on picosecond time scales.

In conclusion, we summarize the main results of our work.

(i) We have numerically investigated the structure of a universal relativistic current filament at the axis of which there is a narrow electron density peak, which is responsible for drift current transport in crossed electric and magnetic fields within the filament.

(ii) We have considered the compression of the ion plasma component by the electric field of a nonquasineutral electron current structure and have shown that a dense hot plasma core in the Z-pinch is formed due to the excitation of an unloading shock wave that propagates away from the axis and is accompanied by the vanishing of the radial ion velocity behind the shock front.

(iii) We have analytically revealed that quasineutral plasma can rapidly expand in a self-similar manner because of the rapid dissipation of the magnetic field energy in ion–ion collisions on picosecond time scales.

It should be emphasized that recent space- and time-resolved measurements of the structure of Z-pinches [5] and simulations of the evolution of a current-carrying plasma [11], which showed the formation of electron current structures, provide experimental and computational bases for the model of an electron current filament that was proposed in [9] and is used in the present paper.

ACKNOWLEDGMENTS

We are grateful to S.A. Pikuz for providing us with his experimental data prior to their publication. This study was supported in part by the Russian Foundation for Basic Research, project no. 00-02-16305.

REFERENCES

1. Yu. L. Bakshaev, P. I. Blinov, A. S. Chernenko, *et al.*, in *Proceedings of the International Conference on Research Application of Plasmas, 2001*, Report No. PS-22.
2. Yu. L. Bakshaev, P. I. Blinov, V. V. Vikhrev, *et al.*, Fiz. Plazmy **27**, 1101 (2001) [Plasma Phys. Rep. **27**, 1039 (2001)].
3. G. V. Ivanenkov, S. A. Pikuz, D. V. Sinars, *et al.*, Fiz. Plazmy **26**, 927 (2000) [Plasma Phys. Rep. **26**, 868 (2000)].
4. T. A. Shelkovenko, D. V. Sinars, S. A. Pikuz, and D. A. Hammer, Phys. Plasmas **8**, 1305 (2001).
5. S. A. Pikuz, D. V. Sinars, T. A. Shelkovenko, *et al.*, Phys. Rev. Lett. **89**, 035003 (2002).

6. T. A. Shelkovenko, S. A. Pikuz, D. B. Sinars, *et al.*, Phys. Plasmas **9**, 2165 (2002).
7. S. A. Pikuz, D. B. Sinars, T. A. Shelkovenko, *et al.*, Pis'ma Zh. Éksp. Teor. Fiz. **76**, 571 (2002).
8. G. V. Ivanenkov and V. Stepniewski, Fiz. Plazmy **28**, 499 (2002) [Plasma Phys. Rep. **28**, 457 (2002)].
9. A. V. Gordeev and T. V. Losseva, in *Proceedings of the 14th International Conference on High-Power Particle Beams and 5th International Conference on Dense Z-Pinches, New Mexico, 2002*, Book of Abstracts, p. 259; in *Proceedings of the 5th International Conference on Dense Z-Pinches*; AIP Conf. Proc. **651**, 420 (2002).
10. E. S. Weibel, Phys. Rev. Lett. **2**, 83 (1959).
11. J. Sakai, S. Saito, H. Mae, *et al.*, Phys. Plasmas **9**, 2959 (2002).
12. A. V. Gordeev and S. V. Levchenko, Pis'ma Zh. Éksp. Teor. Fiz. **67**, 461 (1998) [JETP Lett. **67**, 482 (1998)].
13. A. V. Gordeev and T. V. Losseva, Pis'ma Zh. Éksp. Teor. Fiz. **70**, 669 (1999) [JETP Lett. **70**, 684 (1999)].
14. A. V. Gordeev, Fiz. Plazmy **27**, 251 (2001) [Plasma Phys. Rep. **27**, 235 (2001)].
15. R. Z. Sagdeev, in *Plasma Physics and the Problems of Controlled Thermonuclear Reactions*, Ed. by M. A. Leontovich (Akad. Nauk SSSR, Moscow, 1958), Vol. 4, p. 384.
16. V. I. Berezhiani, S. M. Mahajan, and N. L. Shatashvili, Phys. Rev. E **55**, 995 (1997).
17. E. S. Oran and J. P. Boris, *Numerical Simulation of Reactive Flow* (Elsevier, New York, 1987; Mir, Moscow, 1990).
18. G. S. Sarkisov, V. Yu. Bychenkov, V. T. Tikhonchuk, *et al.*, Pis'ma Zh. Éksp. Teor. Fiz. **66**, 787 (1997) [JETP Lett. **66**, 828 (1997)].
19. A. V. Gordeev, Fiz. Plazmy **27**, 700 (2001) [Plasma Phys. Rep. **27**, 659 (2001)].
20. B. A. Trubnikov, in *Review of Plasma Physics*, Ed. by M. A. Leontovich (Atomizdat, Moscow, 1963; Consultants Bureau, New York, 1965), Vol. 1.

Translated by O.E. Khadin

Plasma Physics Reports, Vol. 29, No. 9, 2003, pp. 757–763. Translated from Fizika Plazmy, Vol. 29, No. 9, 2003, pp. 818–825.

PLASMA DYNAMICS

Material Transport in a Low-Inductance Vacuum Spark

A. N. Dolgov and G. Kh. Salakhutdinov

Moscow Engineering Physics Institute, Kashirskoe sh. 31, Moscow, 115409 Russia

Received December 26, 2002

Abstract—The transport processes and the parameters of material flows in a low-inductance vacuum spark excited in a medium produced by erosion of the electrodes are investigated. © *2003 MAIK "Nauka/Interperiodica".*

1. INTRODUCTION

High-current ($I_{max} \geq 100$ kA) Z-pinch discharges are characterized by high values of the plasma parameters: $T_e \sim 1$–10 keV and $n_e \sim 10^{22}$–10^{23} cm^{-3} [1].

A micropinch discharge can be excited in a low-inductance spark device, which is very simple in design and reliable in operation. This explains widespread interest in this type of discharges. Such discharges are used as laboratory sources of X-ray and XUV emission from multicharged ions [2]. Micropinch plasma is one of the promising sources of multicharged ions for nuclear physics experiments [3]. Methods of X-ray lithography have been developed for the replication of VLSICs and for contact X-ray microscopy of biological objects with the use of micropinch soft X-ray (SXR) sources [5]. The effect of polishing the surface of high-temperature superconductor films irradiated with high-intensity XUV pulses emitted by micropinch plasma was revealed in [6]. Low-inductance vacuum sparks can also be used to deposit thin metal films.

All these applications of a micropinch plasma require knowledge of mechanisms for the generation and decay of discharge plasmas. This paper is devoted to experimental studies of the transport processes and the parameters of material flows in a low-inductance vacuum spark (LIVS). Figure 1 shows a schematic of the discharge device. The discharge was excited in a vacuum chamber evacuated to a residual pressure of less than 10^{-4} torr. The working medium was produced by the erosion of the electrode material. The electrodes were made of different materials: the anode was made of iron, and the cathode was made of brass. As a pulsed current source, we used a low-inductance high-voltage capacitor bank with a total capacitance of $C = 3$–12 μF. The discharge voltage was $V = 5$–20 kV, the amplitude of the discharge current was $I_{max} = 60$–200 kA, and the discharge current period was $T = 4$–8 μs. The discharge was initiated by injecting a foreplasma from an auxiliary low-current pulsed surface-erosion discharge with a period of ~0.2 μs. The pinching of the discharge plasma and the formation of micropinch regions were usually observed only in the first half-period of the discharge, when the current reached its maximum [17].

2. EXPERIMENTAL TECHNIQUES AND RESULTS OBTAINED

1. In order to determine the position of the region in which a micropinch is formed, we studied the spatial structure of the radiating discharge plasma by using a pinhole camera [8] with and without absorbing filters. As filters, we used 15- and 100-μm beryllium foils and ~1-μm polymeric (Zapon) films. The spatial resolution of the pinhole images was no worse than 0.1 mm.

Micropinches form at a distance of no less than 1–3 mm from the electrode surface, usually closer to the anode. The ~1-mm-thick surface plasma layers near the electrodes do not emit in the SXR and XUV regions, but they emit in the UV–visible region.

2. To estimate the heat fluxes transferred by XUV and SXR radiation, we measured the radiation intensity in these spectral regions with the help of a photodiode and a scintillation detector [7]. The radiation pulse duration was $(0.3–0.5) \times 10^{-7}$ s.

3. To obtain information on the conditions under which the micropinch is formed (i.e., on the parameters of the hot dense plasma of the LIVS discharge), we studied the X-ray line spectrum in the region corresponding to the characteristic radiation (K_α and K_β lines) of the electrode material.

The X-ray spectrum was measured by a crystal spectrograph with the horizontal focusing by the Johann scheme.

X radiation was output from the vacuum chamber through a 100-μ-thick beryllium window (which allowed almost total transmission at wavelengths $\lambda <$ 2 Å) and fell onto a concave SiO_2 (1010) crystal ($2d =$ 8.50 Å; $n = 2$). The curvature radius of the crystal (325 mm) was specified by a metal holder consisting of two ground pieces, between which the 0.2-μm-thick crystal was clamped. The crystal working area was 40×60 mm^2. The crystal holder was mounted on a positioner, which allowed us to move the crystal in the hor-

1063-780X/03/2909-0757$24.00

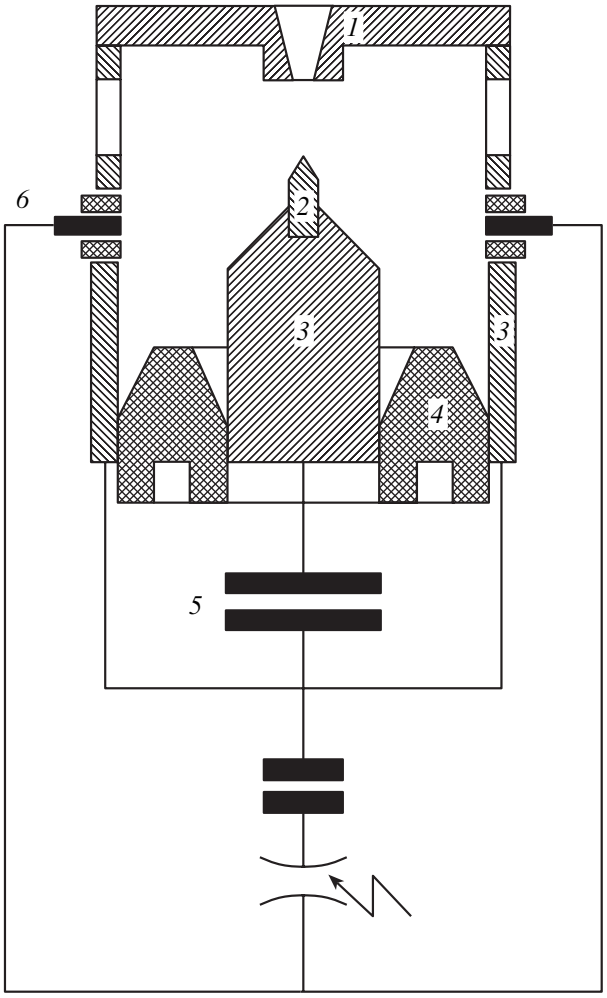

Fig. 1. Schematic of the discharge device: (*1*) cathode, (*2*) anode, (*3*) conductors, (*4*) insulator, (*5*) pulsed high-voltage capacitor bank, and (*6*) discharge-initiation system. The cathode diameter is 20 mm, and the diameter of the cylindrical part of the anode is 4 mm. The interelectrode distance is 6–8 mm.

izontal plane and rotate it around the vertical axis. In this way, we could tune the spectrograph in the wavelength range 1.35–2.00 Å. The radiation was recorded on an RT-1 X-ray film.

Attention was primarily focussed on the spectral intervals from K_α (1.93–1.94 Å) to K_β (1.74–1.75 Å) lines of iron and from K_α (1.53–1.54 Å) to K_β (1.38–1.39 Å) lines of copper.

In the experiments, we reliably detected radiation from iron ions, (including multicharged ions up to Fe XXV). Radiation from copper ions was not detected. Estimates showed that the radiation intensity of copper ions in this case was at least two orders of magnitude lower than that of iron ions.

4. In order to obtain information about the parameters and conditions of the formation of the cold peripheral plasma of the LIVS discharge, the visible spectrum of radiation was recorded with the help of an STE-1 spectrograph. The radiation was output from the vacuum chamber through a quartz window. The spectrograph was calibrated against the emission spectrum of spark and arc discharges excited in the atmosphere between iron electrodes.

The LIVS emission spectrum consists of groups of intense lines of singly charged copper and zinc ions and much less intense lines of atomic and singly charged iron against the background of recombination radiation. We studied the profiles of the brightest lines of Zn II ions: 4911.7 Å ($4d^2D_{3/2} \longrightarrow 4f^2F_{5/2}$); 4924.0 Å ($4d^2D_{5/2} \longrightarrow 4f^2F_{7/2}$); 6021.3 Å ($5p^2P_{1/2} \longrightarrow 5d^2D_{3/2}$); 6102.5 Å ($5p^2P_{3/2} \longrightarrow 5d^2D_{5/2}$). In order to determine which mechanism for the line broadening is predominant, we plotted the logarithm of the line intensity versus distance $\Delta\lambda$ from the center of the line [9]. A line broadened due to the Doppler effect has a Gaussian profile falling as $\exp\left[-\left(\frac{\Delta\lambda}{\lambda}\right)^2\right]$, whereas the Stark broadening gives the profile falling as $(\Delta\lambda)^{-2}$. The results obtained show that the Stark broadening is predominant. For the above lines, the measured broadening amounts to $\Delta\lambda = 4$–10 Å.

Based on the Stark broadening model, we estimated the electron density of the radiating plasma. In the quasistatic approximation, the broadening due to the Stark effect [10] is

$$\Delta\lambda = 6.5\alpha a^3\lambda^2 n_e^{4/3}, \quad (1)$$

where $a = a_B n^2/z$ is the orbit radius of an outer electron, $a_B = \hbar^2/m_e e^2$ is the Bohr radius, $\alpha = e^2/\hbar c$, n is the level number, and z is the charge of the atomic core. For the group of lines corresponding to the radiation of the material of the outer electrode (cathode), the calculated value of the electron density is

$$n_e \cong 10^{18}\ \text{cm}^{-3}, \quad (2)$$

which agrees well with the results of laser interferometry of the peripheral plasma density in a micropinch discharge [11].

The electron temperature of the radiating plasma was determined from the decay in the intensity of recombination continuum [12]:

$$T_e = \frac{2\pi\hbar\Delta\nu}{k\Delta\{\ln[i_c(\nu)]\}}, \quad (3)$$

where $\Delta(\ln[i_c(\nu)])$ is the difference between the logarithms of the relative continuum intensities at the ends of the frequency interval $\Delta\nu$ and k is the Boltzmann constant. The electron temperature in our experiments was estimated as

$$T_e \cong 1\ \text{eV}. \quad (4)$$

5. Using a thermocouple calorimeter (designed at the Lebedev Physical Institute of the Russian Academy of Sciences), we studied the spectrum of the LIVS plasma over a wide spectral range: from the infrared to the SXR region. The radiation detector in this device is a 8-mm-diameter plate made of a 100-μm lead foil and blackened on the outside. The "hot" ends of a copper–constantan thermoelectric battery are glued to the back surface of the foil with a heat-conducting glue. The "cold" ends are glued to a massive metal housing of the device. The calorimeter was calibrated with a pulsed IZ-25 YAG laser. The amplitude of voltage pulses arising at the outputs of the thermoelectric battery was measured with an F-138 microvoltmeter. The receiving area of the calorimeter and an IMO-2I standard power meter were in turn exposed to a laser beam passed through a diaphragm. Based on the results of numerous measurements, we determined the sensitivity of the calorimeter. An important advantage of the calorimeter is that its characteristic (the dependence of the output voltage on the absorbed energy) is linear.

The high noise level, which exceeded the amplitude of valid signals, made it necessary to take special measures in order to suppress noise. Thus, we used a ferrite stabilizer in the supply circuit of the microvoltmeter and an *LC* filter in the measurement circuit at the microvoltmeter input, the chassis of the microvoltmeter was grounded through an individual conductor that was not connected to the main ground circuit of the device, and the calorimeter housing was galvanically decoupled from the vacuum chamber in which the measuring element of the calorimeter was placed.

To study the radiation spectrum, the calorimeter was equipped with a set of absorbing filters. As such filters, we used 15- to 100-μm beryllium foils; 2- to 20-μm aluminum foils; 5-μm copper, silver, and bismuth foils; 200-μm silicon plates; 1-mm quartz glass plates; 1-mm lithium fluoride plates; and 0.25- to 1-μm Zapon films. The polymeric filters were protected from being damaged by plasma flows from the discharge; for this purpose, a fine metal mesh with a mesh size of 8×8 μm and transmittance of 50% was placed near the discharge. The calculated transmission curves of the filters were used [13–15].

The radiation spectrum was reconstructed using a fitting procedure [16], which can be described as follows. We solved a set of linear algebraic equations written on the basis of the data obtained from calorimeter measurements and the calculated response of the calorimeter to radiation in chosen spectral intervals. The radiation energy before passing through the filter was taken to be unity, and the spectral density within each spectral interval was assumed to be constant. Thus, the reconstructed spectrum was represented as a histogram in which the height of a column corresponding to a given spectral region was equal to the radiation energy divided by the width of the spectral region expressed in units of photon energy.

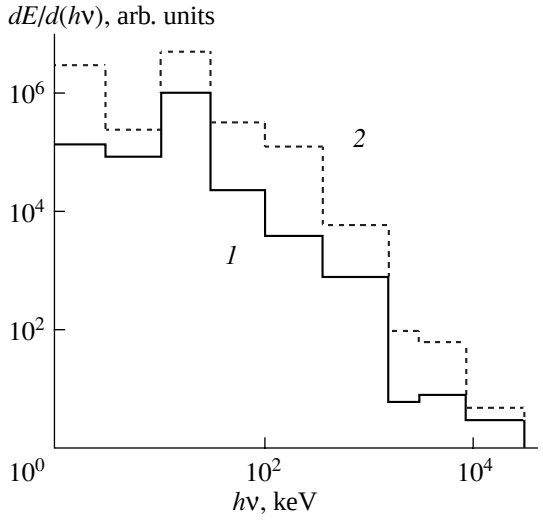

Fig. 2. Spectrum of the LIVS plasma at I_{max} = (*1*) 45 and (*2*) 180 kA (C = 12 μF; T = 8 μs).

We solved the following set of equations:

$$\sum_{i=1}^{n}\left(E_i - \sum_{j=1}^{m} a_{ij}J_j\right)a_{ik} = 0, \quad k = 1, 2\ldots m; \ m \le n, \quad (5)$$

where n is the number of filters, m is the number of the chosen spectral intervals, E_i is the detector signal behind the ith filter, a_{ik} is the calculated detector signal behind the ith filter exposed to the radiation corresponding to the kth histogram column of unit height, and J_j is the sought height of the histogram column for the jth spectral interval. This allowed us to find the linear combination of the column heights J_j that gives the minimum difference between the measured and calculated attenuation curves (the distributions of the energy absorbed by the detector). The shape of the spectrum varied insignificantly when a random measurement error corresponding to the scatter in the detector data in different discharges was introduced into the detector signal. A typical reconstructed spectrum of the LIVS radiation from the infrared to SXR region is shown in Fig. 2.

The calibration of the calorimeter allowed us to perform absolute measurements of the discharge plasma emission. Figure 3 shows the measured dependence of the emission energy integrated over the entire spectrum on the amplitude of the discharge current. Most (≥50%) of the emission energy is concentrated in the XUV region.

6. We estimated the fractions of the anode and cathode materials in the total mass of the electrode material escaping from the discharge. To do this, a preliminarily etched 10×10-mm plane molybdenum target was placed outside the discharge, 10 cm from the axis of the discharge gap. During the discharge, the material of the

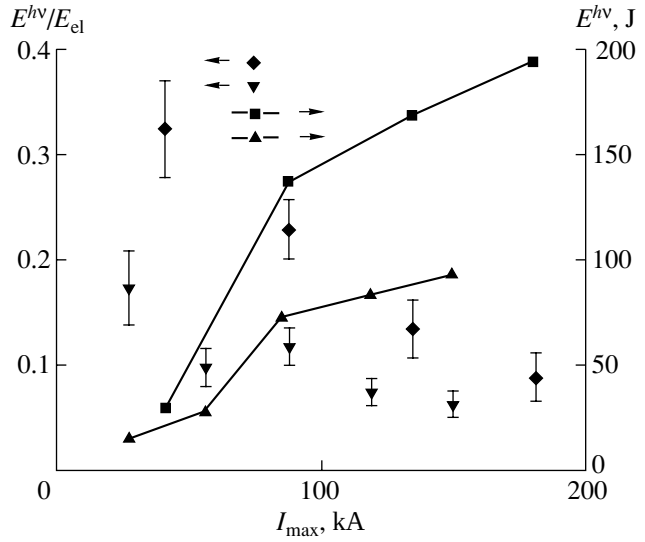

Fig. 3. Conversion efficiency of the current-source energy into the LIVS plasma energy and the radiation energy integrated over the spectrum as functions of the amplitude of the discharge current. The triangles correspond to a current source with $C = 6$ μF ($T = 6$ μs), and the squares and diamonds correspond to a source with $C = 12$ μF ($T = 8$ μs).

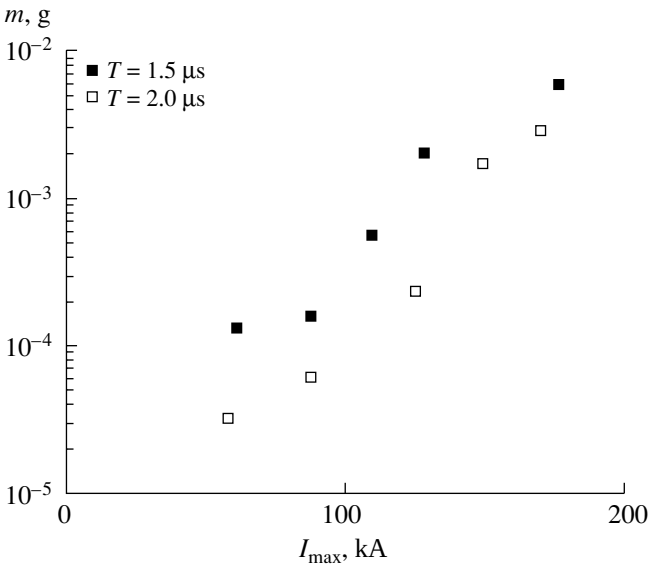

Fig. 4. Mass of the material sputtered in one discharge as a function of the amplitude of the discharge current.

eroded electrodes was deposited on this target. The chemical composition of the electrode material deposited on the target was analyzed by the method of secondary ion–ion emission with the help of a SIM device, designed at the Moscow Engineering Physics Institute. A 20-keV helium ion beam bombarded the surface of the exposed target under high-vacuum (~10^{-8} torr) conditions. The collimated beam of the secondary ions fell into a magnetic separator, in which the ions with different masses were separated and recorded.

Taking into account that all the fractions of the eroded electrode material are deposited onto the target surface under similar conditions and the elements involved (iron, copper, and zinc) are closely positioned in the periodic table and have similar physical and chemical properties, we can suggest that the proportion between the currents produced by the ions of these elements in the analyzer coincides with the proportion of these elements on the target surface. Additional evidence in favor of this suggestion is that the proportion between the secondary-ion currents for copper and zinc coincides with the proportion of these elements in the cathode material (brass).

An analysis of the chemical composition of the material deposited on the target surface shows that the number of atoms of the sputtered anode material is at least one order of magnitude greater than the that of the sputtered cathode material. However, visual observations of the state of the electrodes contradict this conclusion, because we observed nearly the same erosion on both electrodes.

7. The amount of the material sputtered in the discharge was estimated from the transmission factor (at $\lambda = 5893$ Å) of the electrode material layer deposited on a glass plate [17]. The absorption coefficient of this layer was calculated by the formula

$$\gamma = 4\pi\kappa/\lambda, \quad (6)$$

where $\kappa = 1.63$ for iron. The transmission factor, defined by the formula

$$1 - \frac{I}{I_0} = 1 - \exp(\gamma\delta),$$

was measured with a SPECORD spectrophotometer. Here, I_0 is the radiation intensity at a given wavelength in the absence of an absorbing layer on the glass plate, I is the intensity of the radiation passed through the deposited layer (before passing through the glass), and δ is the layer thickness. The results of the measurements are presented in Fig. 4, which shows the mass of the material sputtered into the total solid angle (4π sr) as a function of the amplitude of the discharge current, assuming that the sputtering of the electrode material is isotropic. The mass of the sputtered material increases rapidly with increasing current. As the current amplitude increases fourfold, the mass of the sputtered material increases by nearly two orders of magnitude.

We note that the mass of the sputtered material depends not only on the amplitude of the discharge current, but also on the parameters of the discharge circuit. The highest sputtering efficiency is observed in the regime with the highest intensity of short-wavelength (XUV and SXR) emission.

8. We also studied the energy and charge composition of the ion bunches leaving the LIVS discharge. Two methods were used: the separation of particles in parallel magnetic and electric fields in a Thomson analyzer with a photoemulsion detector and the time-of-

flight technique with a passive collector [18]. The discharge current in these experiments reached $I_{max} \cong 120$ kA.

The former method provides the calibrated detection of each component of the ion flux, and the latter technique allows one to estimate the number of the emitted ions and examine the ion energy spectrum over a wide range. The results of these measurements show that most of the emitted ions are singly charged iron ions. The range of the ion energies is 20 eV–50 keV. The average number of the ions emitted in one discharge is ~10^{17} ion/sr for ions with energies higher than 5 keV and (3–5) × 10^{17} ion/sr for ions with energies lower than 5 keV.

9. Visual observations of the state of the electrodes exposed to the particle flows generated in the discharge show that, in the course of discharge, the electrode material is melted and transferred along the electrode surface to the discharge periphery. In addition, we observed a unidirectional transport of the anode material toward the cathode and the fragmentation of the melted electrode material, i.e., the formation of metal drops with diameters of ~10–100 μm. Judging from the rate at which the anode length decreases, the mass leaving the anode surface in one discharge amounts to ~(1–2) × 10^{-3} g. The degrees of erosion of the cathode and anode surfaces are comparable to each other.

3. DISCUSSION OF THE EXPERIMENTAL RESULTS

In the initial stage of the discharge, the erosion of the anode occurs under the action of an electron beam propagating in the interelectrode gap [19]. The heating of the anode surface layer can be described as follows [20]:

$$T_a - T_0 = \frac{jU\tau_h}{(R+X)\left(\frac{1}{T_b - T_0}\int_{T_0}^{T_b} \rho C_P dT\right)}, \quad (7)$$

where R is the depth to which the anode is heated by the electron beam, X is the depth to which the deeper anode layers are heated due to heat conduction, j is the current density, U is the accelerating voltage, T_b is the boiling temperature of the anode material, T_0 is the initial temperature, and ρ is the mass density of the anode material. At electron energies of $0.01 \le E \le 2$ MeV, we have

$$R = \frac{1}{\rho}\frac{Z_{Al}}{Z_{Fe}} \times 0.412 E^{(1.265 - 0.095 \log E)} \text{ [cm]},$$

where Z is the atomic number of the element. The depth X is equal to

$$X = (\chi\tau_h)^{1/2}, \quad (8)$$

where χ is the thermal conductivity of the anode material and τ_h is the heating time.

For an applied voltage of U = 10 kV and a design value for the device impedance of ~10 Ω, the electron beam current attains a value of ~1 kA. Then, for a heating time of $\tau_h \cong (3–5) \times 10^{-7}$ s [19], we have $(R + X) \sim 1$ μm. Taking into account an uncertainty in determining the surface area bombarded by electrons, we find that the mass of the evaporated material is ~10^{-6}–10^{-5} g. At a charging voltage of U = 10 kV, the amplitude of the discharge current is $I_{max} \cong 60$ kA for a capacitor bank with a capacitance of C = 6 μF and it is $I_{max} \cong 90$ kA for C = 12 μF. It can be seen from Fig. 4 that, at such currents, the mass of the sputtered electrode material is on the order of 10^{-4} g. Therefore, even at relatively low discharge currents, there is no agreement between the above estimate and the measured mass of the sputtered material. Hence, the erosion of the electrodes is due to an electron beam only in the initial stage of the discharge, until the discharge gap becomes bridged by a sufficiently dense plasma that provides the high conductivity of the gap. When the discharge current becomes high enough, other mechanisms come into play. The role of the electron beam is to create a plasma with a linear electron density of $N_e > 10^{16}$ cm^{-1}, which is sufficient to ensure the pinching regime.

The thermal conductivity of the cold plasma, which exists throughout almost the entire discharge phase, is also insufficient to provide the observed electrode erosion. The thermal energy transferred to the electrode in a time on the order of the discharge duration $\tau \sim 10^{-5}$ s due to the plasma heat conduction at an average electron temperature of $T_e \sim 1$ eV is estimated as

$$Q \sim \lambda_e \frac{T_e}{l}\tau \sim 10^{-2} \text{ J/cm}^2, \quad (9)$$

where $l \cong 1$ mm is the characteristic scale length of the temperature inhomogeneity, $\lambda_e \cong 2.65 \times 10^{-2}(T_e[\text{eV}])^{3/2}/\Lambda$ [W/cm K] is the electron thermal conductivity [21], and Λ is the Coulomb logarithm. This corresponds to the evaporation of ~10^{-6} g of the anode material.

On the other hand, the observed ion fluxes toward the cathode surface are sufficient to provide the evaporation and sputtering of ~10^{-4}–10^{-3} g of the cathode material.

Powerful electrode-heating mechanisms come into play at the stage of plasma pinching in the first half-period of the discharge current. For example, an iron plasma flow with a velocity of $v \sim 10^6$ cm/s (which is a characteristic velocity of the cumulative axial plasma flow in the initial stage of pinching [22]) has an ion density of $n_i \sim 10^{18}$ cm^{-3}. When this flow is decelerated on

the electrode surface, it provides an energy flux with a density of

$$Q \sim \frac{1}{2} m_i v^3 n_i, \quad (10)$$

where m_i is the ion mass. During the characteristic pinching time $\tau \sim (3–5) \times 10^{-7}$ s, this energy flux is sufficient to evaporate up to $\sim 5 \times 10^{-4}$ g of the cathode material and $\sim 2 \times 10^{-5}$ g of the anode material. The difference is due to the different exposed areas on the cathode and the anode.

The absorption of the short-wavelength radiation emitted by the micropinch plasma can provide the evaporation of $\sim 10^{-2}$ g of the cathode material and $\sim 10^{-3}$ g of the anode material.

For the pinch-plasma temperature $T_e \sim 20$ eV [11], the characteristic scale length of the temperature inhomogeneity $l \sim 1$ mm, and the pinch lifetime $\tau \sim (3–5) \times 10^{-7}$ s, the energy flux from the pinch plasma due to heat conduction can evaporate $\sim 2 \times 10^{-3}$ g of the electrode material.

It is also necessary to take into account the limitations imposed by the thermal conductivity of the metal. Estimates show that, in a time $\tau \sim (3–5) \times 10^{-7}$ s, the mass that can be heated to the boiling temperature is $\sim 3 \times 10^{-4}$ g on the cathode surface and $\sim 10^{-5}$ g on the anode surface.

As follows from the structure of the electrode surface exposed to plasma flows generated in the discharge, mechanical stresses can also significantly contribute to the destruction of the electrode surface. During the pinching, the iron plasma flow produces a pressure of $m_i n_i u^2 \sim 10^4$ atm on the electrode surface. This pressure significantly exceeds the strength of the electrode material [23]. The mechanical action of the plasma flow on the electrode surface causes the destruction and fragmentation of the electrode material. If the size of the produced metal fragments is ~10–100 μm, then the effective area of the interface separating the liquid and solid phases from the gaseous one increases by a factor of $\sim 10^2$–10^3. Accordingly, the rate of heat exchange between the discharge plasma and the electrode material increases, which leads to an increase in the mass of the evaporated electrode material.

We also note that the geometry of the discharge device is such that, in the course of discharge, most of the sputtered anode material is entrained by the plasma flow in the axial direction, whereas most of the sputtered cathode material is entrained in the radial direction and some portion of this material is again deposited on the cathode.

In a LIVS discharge, the erosion process on the anode differs from that on the cathode. The discharge pinching occurs in the plasma produced from the anode material (iron). Hence, we only observed SXR emission from iron ions and did not observe SXR emission from copper ions. In the visible region, the emission from the ions of the cathode material (copper and zinc) is predominant. Based on the estimates of the density and temperature of the plasma emitting in the visible region, we suggest that, near the cathode, the plasma is a weakly ionized, almost saturated vapor of the cathode material [24]. This explains the shape of the plasma emission spectrum, which has two distinct maxima: one maximum is in the XUV and SXR regions and the other one is in the visible and near-infrared regions. In other words, there are two plasma regions with different temperatures and chemical compositions: the cold region with a plasma temperature of $T_e \cong 1$ eV, which is related to the cathode erosion, and the hot region with $T_e \cong 10$ eV–1 keV (the temperature varies during the formation of the micropinch region), which is related to the anode erosion. Probably, these temperatures determine the energies of the particles that leave the corresponding regions during the plasma decay and form the observed particle flows outside the discharge.

Let us consider the results of measurements of the ion flows and the mass of the material deposited on the target, as well as the chemical composition of the material deposited on the target. The mass carried out by the ion flow from the discharge (10^{-4}–10^{-3} g) is close to the mass of the sputtered anode material. At the same time, as was mentioned above, the degrees of erosion of the anode and the cathode surfaces are comparable to each other, whereas the products of the cathode erosion are present in a lesser amount on the target. This can be explained by the fact that the deposition conditions of the cathode and anode materials on the target are different. The sputtered anode material arrives at the target in the form of relatively high-energy ions, which results in a high degree of adhesion. In contrast, the sputtered cathode material arrives at the target in the form of low-energy neutrals, which are characterized by a low degree of adhesion.

Let us dwell on another observed phenomenon, namely, unidirectional transport of the anode material onto the cathode. Such a transport can be explained by the action of ponderomotive forces that play the role of a piston accelerating the plasma in the axial direction as it occurs, for instance, in plasma accelerators with a similar configuration of the electrodes. This is confirmed by the results of high-speed multiframe photography of the LIVS plasma with the help of a pulsed laser illuminator [25]. It has been revealed that the boundary of the plasma column in the LIVS is subject to the Rayleigh–Taylor instability, which results in the radial shrinking of some segments of the discharge column with a velocity up to $\sim 4 \times 10^6$ cm/s. The constrictions produced move along the axis toward the cathode with velocities of up to $\sim 10^6$ cm/s.

4. CONCLUSIONS

The results obtained allow us to compile the following picture of the processes of material transport in a LIVS operating in the micropinch regime. In the initial discharge stage, which lasts $\sim 3 \times 10^{-7}$ s, the interelectrode space is filled with a low-conductivity rarified foreplasma. This leads to the generation of an electron beam accelerated in the electric field applied to the interelectrode gap. The bombardment of the anode surface with accelerated electrons causes the evaporation and ionization of the anode material. The plasma produced fills the interelectrode gap and bridges it. As a result, the Ohmic resistance of the discharge gap becomes much less than the circuit impedance.

The increase in the discharge current is accompanied by the pinch effect, which results in a substantial local increase in the plasma density and temperature. The discharge plasma (more exactly, the micropinch plasma) becomes an intense radiation source. During a time of $\sim(3–5) \times 10^{-7}$ s, about 10–20% of the energy stored in the pulsed current source (capacitor bank) is radiated predominantly in the XUV and SXR spectral regions. The radiation incident onto the electrode surface, as well as the heat flux from the hot pinch plasma, causes the melting and evaporation of the electrode surface layer, and the cumulative plasma jet propagating along the discharge axis from the micropinch region results in electrode erosion.

The pinching terminates with the decay of a dense hot plasma produced from the anode material. This results in the generation of charged particle flows (including those directed to the electrodes) that escape from the micropinch region with velocities of $\geq 10^6$ cm/s. Note that ponderomotive forces lead to a unidirectional transport of the anode material along the discharge axis toward the cathode.

Then, the interelectrode space gets filled with a dense cold plasma, which is predominantly a weakly ionized, nearly saturated vapor of the cathode material. This plasma emits for $\sim 10^{-5}$ s (mainly in the visible and near-infrared regions). The outflow of the products of the discharge decay from the interelectrode gap (as a rule, the second pinching does not occur) is accompanied by the generation of neutral flows with velocities of $\sim 10^5$ cm/s at the discharge periphery [11].

ACKNOWLEDGMENTS

We thank O.V. Bashutin, D.L. Kirko, and A.S. Savelov for assistance in experiments.

REFERENCES

1. É. Ya. Kononov, K. N. Koshelev, and Yu. V. Sidel'nikov, Fiz. Plazmy **11**, 927 (1985) [Sov. J. Plasma Phys. **11**, 538 (1985)].
2. Li Vont, Prib. Nauchn. Issled., No. 7, 117 (1984).
3. Yu. A. Bykovskiĭ, V. B. Lagoda, and G. A. Sheroziya, Pis'ma Zh. Éksp. Teor. Fiz. **30**, 489 (1979) [JETP Lett. **30**, 458 (1979)].
4. K. A. Valiev, L. V. Velikov, Yu. S. Leonov, and O. G. Semenov, Élektron. Prom. **13**, 75 (1984).
5. V. A. Veretennikov, A. E. Gureĭ, K. T. Karaev, *et al.*, Preprint No. 10 (Lebedev Physical Inst., Russ. Acad. Sci., Moscow, 1994).
6. Yu. V. Afanas'ev, V. A. Veretennikov, D. G. Emel'yanov, *et al.*, Preprint No. 59 (Lebedev Physical Inst., USSR Acad. Sci., Moscow, 1991).
7. V. V. Averkiev, A. N. Dolgov, V. K. Lyapidevskiĭ, *et al.*, Fiz. Plazmy **18**, 596 (1992) [Sov. J. Plasma Phys. **18**, 374 (1992)].
8. V. A. Veretennikov, A. N. Dolgov, O. N. Krokhin, and O. G. Semenov, Fiz. Plazmy **11**, 1007 (1985) [Sov. J. Plasma Phys. **11**, 587 (1985)].
9. V. P. Bogen, in *X-Ray Diagnostics of Plasmas*, Ed. by W. Lochte-Holtgreven (Elsevier, New York, 1968; Mir, Moscow, 1971).
10. S. E. Frish, *Optical Spectra of Atoms* (Fizmatlit, Moscow, 1963), p. 361.
11. V. A. Veretennikov, A. E. Gureĭ, T. Pisarchik, *et al.*, Fiz. Plazmy **16**, 818 (1990) [Sov. J. Plasma Phys. **16**, 475 (1990)].
12. V. N. Kolesnikov, *Optical Diagnostics of Thermally Equilibrium Plasma* (Moscow Engineering Physics Inst., Moscow, 1984).
13. M. A. Blokhin and I. G. Shveĭtser, *Handbook of X-ray Spectra* (Nauka, Moscow, 1982), p. 376.
14. J. A. Samson, *Techniques of Vacuum Ultraviolet Spectroscopy* (Wiley, New York, 1967), p. 184.
15. V. V. Kozelkin and N. F. Usol'tsev, *Principles of Infrared Engineering* (Mashinostroenie, Moscow, 1974), p. 335.
16. S. A. Zverev, Candidate's Dissertation in Physics and Mathematics (Moscow, 1981), p. 233.
17. G. V. Kaloshnikov, K. N. Koshelev, Yu. V. Sidel'nikov, and S. S. Churilov, Fiz. Plazmy **11**, 254 (1985) [Sov. J. Plasma Phys. **11**, 150 (1985)].
18. V. A. Veretennikov, A. E. Gureĭ, A. N. Dolgov, *et al.*, Pis'ma Zh. Tekh. Fiz. **21** (11), 78 (1995) [Tech. Phys. Lett. **21**, 940 (1995)].
19. V. A. Veretennikov, Yu. S. Leonov, V. I. Mishachev, and O. G. Semenov, Pis'ma Zh. Tekh. Fiz. **11**, 1200 (1985) [Sov. Tech. Phys. Lett. **11**, 497 (1985)].
20. V. I. Derzhiev, F. V. Libakh, and G. I. Remendik, Zh. Tekh. Fiz. **51**, 719 (1981) [Sov. Phys. Tech. Phys. **26**, 428 (1981)].
21. Yu. P. Raizer, *Gas Discharge Physics* (Nauka, Moscow, 1987; Springer-Verlag, Berlin, 1991).
22. A. N. Dolgov, Fiz. Plazmy **22**, 639 (1996) [Plasma Phys. Rep. **22**, 569 (1996)].
23. *Tables of Physical Quantities*, Ed. by I. K. Kikoin (Atomizdat, Moscow, 1976).
24. V. P. Nikol'skiĭ, *Handbook for Chemisists* (Nauka, Moscow, 1966), p. 789.
25. V. A. Veretennikov, S. N. Polukhin, O. G. Semenov, and Yu. V. Sidel'nikov, Fiz. Plazmy **7**, 1199 (1981) [Sov. J. Plasma Phys. **7**, 656 (1981)].

Translated by N.F. Larionova

Plasma Physics Reports, Vol. 29, No. 9, 2003, pp. 764–767. Translated from Fizika Plazmy, Vol. 29, No. 9, 2003, pp. 826–829.

PLASMA DYNAMICS

Feasibility of Igniting Thermonuclear Reaction during the Gas-Dynamic Compression of a Capsule Filled with a Gaseous DT Mixture by a Compact High-Speed Plasma Liner

G. V. Dolgoleva, V. F. Ermolovich, A. V. Ivanovsky, and A. P. Orlov

All-Russia Research Institute of Experimental Physics, Russian Federal Nuclear Center, Sarov, Nizhni Novgorod oblast, 607188 Russia

Received August 29, 2002; in final form, January 21, 2003

Abstract—The feasibility is considered of igniting thermonuclear reaction during the gas-dynamic compression of a capsule filled with a gaseous DT mixture by a compact high-speed plasma liner. Semiempirical parameters of the liner are chosen by analyzing the results of experiments on X-ray generation in the PBFA-Z device. Results are presented from one-dimensional scaling calculations of the neutron yield, temperature, and gas compression ratio over a wide range of liner current. © *2003 MAIK "Nauka/Interperiodica".*

1. INTRODUCTION

In recent years, significant progress has been achieved in creating high-speed (~(4–7) × 10^7 cm/s) liners with an energy of ~1 MJ (e.g., the PBFA-Z device). At present, next-generation electrophysical devices with a liner energy of ≥10 MJ are being developed. These devices are primarily intended to generate soft X rays, which then should be used to ignite thermonuclear reaction inside a hollow target. An alternative method of ignition may be direct gas-dynamic compression of a capsule filled with a gaseous DT mixture. Hence, it is of interest to compare the potentialities of these two methods.

The physics of the formation and implosion of a wire-array liner is rather complicated, and an adequate description of the processes occurring in it can only be provided by three-dimensional numerical simulations. In view of the very different spatial scales on which these processes occur (the initial wire diameter is ~10 μm, and the displacement of the liner produced is ~1 cm), an efficient computational procedure for full-scale three-dimensional simulations of such objects can hardly be created in the near future.

In this paper, we use the model of a compact plasma liner with the effective parameters that ensure the generation of X-ray pulses with characteristics close to those observed in experiments in the PBFA-Z device [1].

This approach does not pretend to completely describe the formation and implosion of a liner. Nevertheless, it allows one to compare the potentialities of the above two methods of igniting thermonuclear reaction.

2. FORMULATION OF THE PROBLEM

Figure 1 shows the geometry of the problem.

The liner kinetic energy acquired during the interaction with the electromagnetic field is transferred by impact to a cylindrical target. The target is a high-Z (Au, W) shell filled with a gaseous DT mixture. The length z_0 of the liner system is 2 cm. The linear mass m of the liner is equal to that of the cylindrical target. At the initial instant, we specify the target radius r_0, mass per unit length m, velocity v_0, and liner thickness δ. As

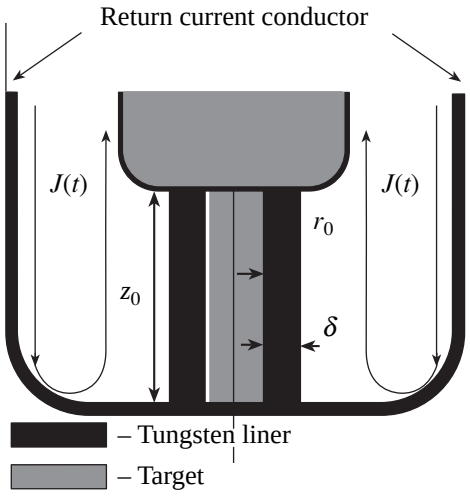

Fig. 1. Scheme of the gas-dynamic compression of a cylindrical target filled with a gaseous DT mixture.

1063-780X/03/2909-0764$24.00 © 2003 MAIK "Nauka/Interperiodica"

in [1], the mass density of the liner material is assumed to be constant and equal to $\rho_0 = m/\pi[(r_0 + \delta)^2 - r_0^2)]$.

Two-temperature gas-dynamics equations were solved numerically using a one-dimensional code ALF [2]. The code takes into account the following effects and processes:

(i) physical viscosity, momentum transfer by neutrons and fast charged particles, energy release due to thermonuclear and neutron-nuclear reactions, and mass variations due to transport of neutrons and fast charged particles;

(ii) radiation transfer in the model of nonequilibrium spectral quasi-diffusion with allowance for Compton diffusion;

(iii) heat transfer by electrons and ions;

(iv) the kinetics of thermonuclear and neutron-nuclear reactions;

(v) the transport of fast charged particles produced in thermonuclear and neutron-nuclear reactions and due to the elastic scattering of neutrons by the thermal H, D, T, He^3, and He^4 recoil nuclei; and

(vi) neutron transport (by calculating the thermal dispersion of DT neutrons and the energy distribution of neutrons produced in the nonthermal TD reaction).

In the calculations, we used the equations of state of the materials according to [3] and the radiation ranges calculated by the PERST-3 procedure [4].

The liner parameters m, v_0, r_0, and δ were determined by fitting the calculated radiation parameters to the parameters measured in the PBFA-Z experiments.

Investigations performed in [1] showed that, for a radiation power of $P_r \cong 290$ TW, the liner thickness was $\delta \cong 3.7$ mm. As the current increases, the effective liner thickness may decrease as the number of wires ($\sim J^2$) increases due to both the improved conditions of the shell formation and reduced initial perturbations. For this reason, we also considered a promising version with $\delta \cong 1.6$ mm, which corresponds to $P_r \cong 10^3$ TW under the PBFA-Z conditions.

For a given linear mass m and an initial coordinate R_0, the liner velocity at the instant of its collision with the target, $v_0 = v|_{r = r_0 + \delta}$, is determined from the motion equation

$$\begin{cases} \dfrac{dr}{dt} = v \\ \dfrac{dv}{dt} = -\dfrac{\mu_0}{4\pi r m} J^2(t). \end{cases} \quad (1)$$

New-generation devices are similar in design to the PBFA-Z device; hence, in order to estimate the liner current J, we can use the PBFA-Z equivalent electrical scheme (Fig. 2) described by the equations [6]

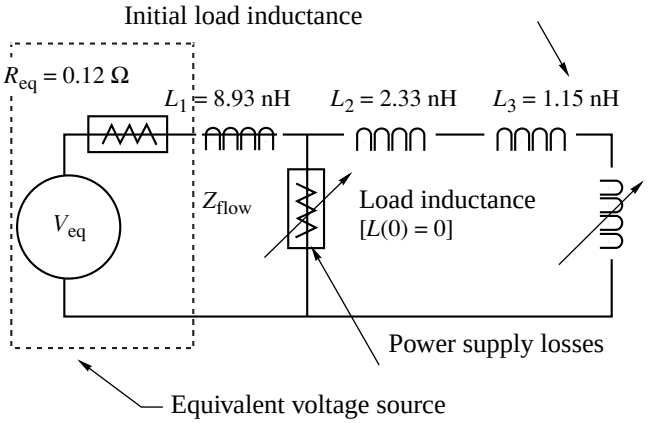

Fig. 2. Equivalent electric circuit of the PBFA-Z device [5].

$$\begin{cases} \dfrac{dJ}{dt} + \dfrac{R(t)J}{L_2 + L_3 + L(t)} = \dfrac{Z_{flow}\sqrt{J_s^2 - J^2}}{L_2 + L_3 + L(t)} \\ \dfrac{dJ_s}{dt} + \dfrac{R_{eq}J_s}{L_1} + \dfrac{Z_{flow}\sqrt{J_s^2 - J^2}}{L_1} = \dfrac{V_{eq}(t)}{L_1}. \end{cases} \quad (2)$$

Here, r and v are the coordinate and velocity of the liner, J_s is the source current, $L(t) = (\mu_0 z_0/2\pi)\ln(R_0/r(t))$ is the liner inductance, and $R(t) = (\mu_0 z_0/2\pi)v(t)/r(t)$ is the resistance related to energy losses caused by the liner acceleration.

In the PBFA-Z device, the voltage of the equivalent voltage source is $V_{eq} \cong 5.8$ MV and the electromagnetic pulse energy is $W \cong 5$ MJ. For the projected devices, this energy can be recalculated by the scaling law $W \sim V_{eq}^2$.

Equations (1) and (2) were solved with the following initial conditions: $J|_{t=0} = 0$, $J_s|_{t=0} = 0$, $r|_{t=0} = R_0$, and $v|_{t=0} = 0$. The initial liner radius was chosen to be $R_0 = 2$ cm.

3. RESULTS OF CALCULATIONS

The calculations have shown that the maximum number of DT reactions per unit length is attained at the target radius $r_0 \cong 0.2$–0.3 cm and the liner velocity $v_0 \cong 4$–5×10^7 cm/s.

The neutron yield and the gas compression ratio as functions of r and v for different liner thicknesses and electromagnetic pulse energies are shown in Figs. 3 and 4.

At $W = 100$ MJ, the DT mixture is not ignited (only a few tenths of one percent of the mixture is burnt out, and the maximum temperature is ~2–3 keV); however,

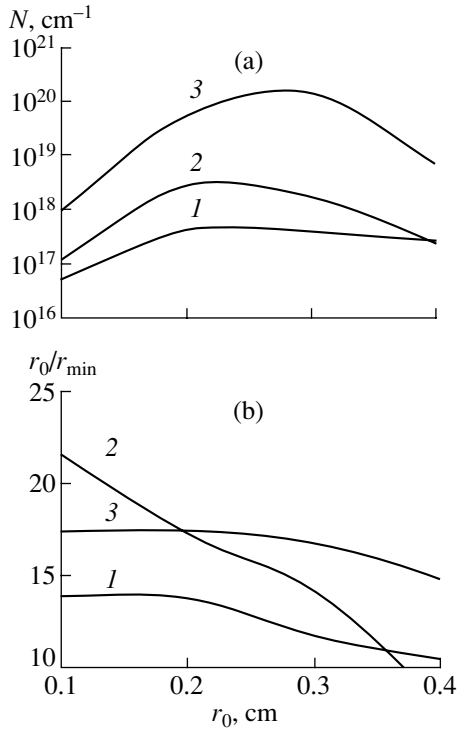

Fig. 3. (a) The number of DT reactions per unit length and (b) the gas compression ratio as functions of the target radius for $v_0 = 4 \times 10^7$ cm/s: (*1*) $\delta = 3.7$ mm, $W = 100$ MJ; (*2*) $\delta = 1.6$ mm, $W = 100$ MJ; and (*3*) $\delta = 1.6$ mm, $W = 200$ MJ.

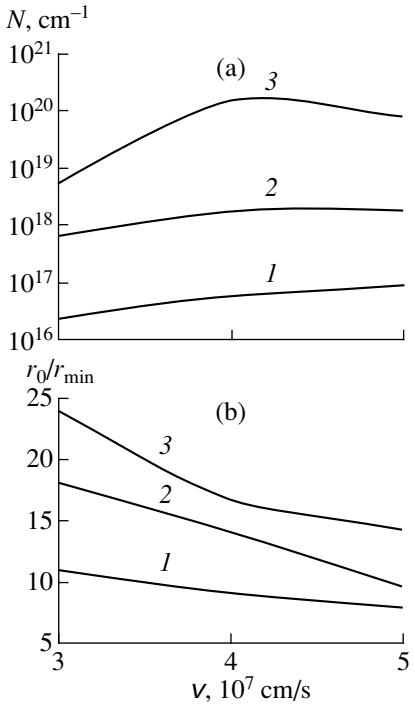

Fig. 4. (a) The number of DT reactions per unit length and (b) the gas compression ratio as functions of the liner velocity for $r_0 = 0.2$ cm: (*1*) $\delta = 3.7$ mm, $W = 100$ MJ; (*2*) $\delta = 1.6$ mm, $W = 100$ MJ; and (*3*) $\delta = 1.6$ mm, $W = 200$ MJ.

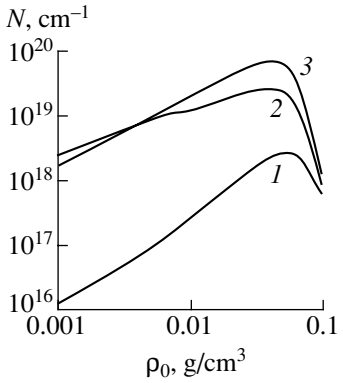

Fig. 5. The number of DT reactions per unit length as a function of ρ_0 for $r_0 = 0.2$ cm and $v_0 = 4 \times 10^7$ cm/s: (*1*) λ_e, λ_i, $L_\alpha \neq 0$; (*2*) λ_e, $\lambda_i = 0$, $L_\alpha \neq 0$; and (*3*) $\lambda_e = \lambda_i = L_\alpha = 0$.

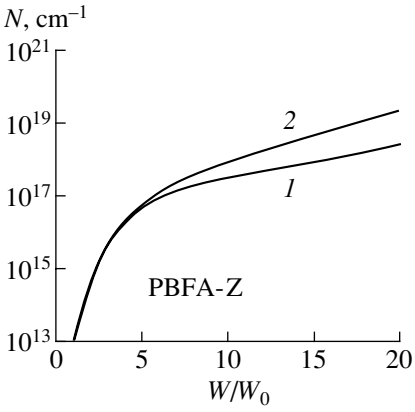

Fig. 6. The number of DT reactions per unit length as a function of the electromagnetic pulse energy for $r_0 = 0.2$ cm and $v_0 = 4 \times 10^7$ cm/s: (*1*) λ_e, λ_i, $L_\alpha \neq 0$ and (*2*) $\lambda_e = \lambda_i = 0$, $L_\alpha \neq 0$.

the system is close to ignition. With a twofold increase in the energy W, ≈10% of the mixture is burnt out and the temperature increases to 10 keV.

Estimates show that the magnetic field produced during the compression of the capsule is high enough not only for the electron and ion thermal conductivities to be suppressed, but also for the α particles generated in the DT reaction to be magnetized. To estimate the influence of these phenomena, we performed calculations with completely suppressed electron and ion thermal conductivities ($\lambda_e = \lambda_i = 0$) and highly magnetized α particles (the α-particle range is $L_\alpha = 0$). The calcu-

lated dependences of the neutron yield on the initial gas density ρ_0 for $\delta = 1.6$ mm and $W = 100$ MJ are shown in Fig. 5.

In the case of suppressed conductivities, a few percent of the DT mixture is burnt out and the temperature amounts to ~10 keV; i.e., ignition is possible at the pulse energy $W \cong 100$ MJ.

Figure 6 shows the dependence of the neutron yield on the electromagnetic pulse energy.

Therefore, the calculations performed by the same liner model show that the electromagnetic energy required for the ignition of thermonuclear reaction during the direct gas-dynamic compression of a gaseous DT capsule ($W \approx 100$ MJ) is close to that required for the ignition of reaction during the compression of the capsule by X radiation (see [1]). The advantages and disadvantages of both methods depend on the possibility of attaining the required gas compression ratio. Note that the problem of stability has been considered in more detail for compression by soft X rays.

REFERENCES

1. V. F. Ermolovich, A. V. Ivanovsky, and A. P. Orlov, in *Proceedings of the 12th IEEE International Conference on Pulsed Power, Monterey, 1999*, Vol. 2, p. 1063.
2. É. M. Antonenko, G. V. Dolgoleva, and V. F. Ermolovich, Vopr. At. Nauki Tekh., Ser. Mat. Model. Fiz. Protsessov, No. 4, 62 (1996).
3. G. M. Eliseev and G. E. Klinishov, Preprint No. 173 (Inst. of Applied Mathematics, USSR Acad. Sci., Moscow, 1982).
4. N. N. Degtyarenko and G. M. Eliseev, *Fractals in Applied Physics*, Ed. by A. E. Dubinov (Arzamas-16, 1995).
5. K. W. Struve, T. H. Martin, R. B. Spielman, *et al.*, in *Proceedings of the 11th IEEE International Conference on Pulsed Power, Baltimore, 1997*, Vol. 1, p. 162.
6. V. D. Selemir, V. A. Demidov, and A. V. Ivanovsky, Fiz. Plazmy **25**, 1085 (1999) [Plasma Phys. Rep. **25**, 1000 (1999)].

Translated by E.L. Satunina

Plasma Physics Reports, Vol. 29, No. 9, 2003, pp. 768–778. Translated from Fizika Plazmy, Vol. 29, No. 9, 2003, pp. 830–840.

PLASMA INSTABILITY

Ponderomotive Force of the Low-Frequency Field and Modulational Instability of Drift Waves

D. N. Klochkov* and S. I. Popel**

**Prokhorov Institute of General Physics, Russian Academy of Sciences, ul. Vavilova 38, Moscow, 117942 Russia*

***Institute of Geosphere Dynamics, Russian Academy of Sciences, Leninskiĭ pr. 38-1, Moscow, 119334 Russia*

e-mail: s_i_popel@mtu-net.ru

Received January 30, 2003; in final form, March 31, 2003

Abstract—A study is made of the processes that occur in an inhomogeneous nonisothermal plasma in a strong external magnetic field and whose characteristic frequencies are lower than the ion Langmuir frequency but higher than the collision frequency. An expression for the ponderomotive force of the low-frequency field is derived. The excitation of a long-wavelength low-frequency drift wave during the development of the modulational instability of a drift pump wave is investigated. The growth rates of the instability are obtained, and the conditions for its onset are determined. The possible relation of the modulational instability to the formation of structures in the plasma is discussed. © *2003 MAIK "Nauka/Interperiodica".*

1. INTRODUCTION

It is common practice to associate the ponderomotive force in a plasma with the gradient of the pressure of a strong high-frequency (HF) field [1]. There are many papers devoted to the investigation of this effect and related nonlinear processes, such as parametric, decay, and modulational instabilities. Interest in this area of research is related to the problems of the interaction of laser radiation with plasma. In such an interaction, the excitation of HF fields in a plasma can be accompanied by the generation of strong low-frequency (LF) potential fields. This situation is encountered, e.g., in a tokamak wall plasma, where drift waves can be produced. In a fusion plasma in which a density of about $n \sim 10^{14}$–10^{15} cm^{-3} is achieved at a temperature of $T \sim 10^8$ K in an external magnetic field with a strength of $B_0 \sim 10$ T, the characteristic frequency of drift waves on the scale on which the plasma density varies ($L \sim 10$ cm) is on the order of $\omega_d \sim cT_e/eB_0L^2 \sim 10^5$–$10^6$ s^{-1}. Nevertheless, even at these frequencies, mean ponderomotive forces are generated and affect plasma ions. This effect was first pointed out by Aleksandrov *et al.* [2], who considered the influence of the LF field of a capacitor on a narrow nonisothermal plasma slab under conditions such that the field frequency is lower than the ion Langmuir frequency but higher than the collision frequency in the plasma. In the one-dimensional one-fluid hydrodynamic approximation, they derived an expression for the ponderomotive force of an LF field and compared it with the corresponding HF ponderomotive force. Later, Morales and Lee [3] obtained an expression for the mean ponderomotive force of a lower hybrid wave propagating along the external magnetic field and across the direction in which the plasma is inhomogeneous, and Benkadda *et al.* [4] investigated the modulational instability of this wave, accompanied by the excitation of LF drift waves. It should be noted that the frequency of the lower hybrid waves is on the order of the highest possible frequency of the drift waves. This indicates that drift waves with comparatively high frequencies can be modulationally unstable, which results in the generation of drift waves with comparatively low frequencies.

The investigation of the effects associated with the modulational instability of drift waves is of interest not only in connection with the practical problems concerning the transport of energy and matter across the magnetic field in an inhomogeneous magnetized plasma but also from the standpoint of the fundamental theory of drift plasma turbulence. During the development of the modulational instability in a weakly turbulent plasma, the correlations between the wave phases become increasingly strong; as a result, the plasma eventually evolves into a strongly turbulent state, in which the waves interact with each other and with the plasma particles [5, 6].

Finite-amplitude drift waves become subject to modulational instability just after their onset in the plasma. Drift waves can be generated by the instabilities (e.g., the Cherenkov interaction with electrons can lead to the growth of waves in the drift frequency range [7]) and also by the external sources (as is the case during microwave plasma heating in a tokamak [4]). In the present paper, we assume that, in the plasma, there is a source of drift waves that is capable of balancing their damping.

1063-780X/03/2909-0768$24.00

The dispersion relation for drift waves allows the LF and HF drift oscillations to be studied separately, in which case we can introduce a hierarchy of time scales characteristic of the problem. Such separation of fast and slow motions makes it possible to formulate a relatively simple set of self-consistent hydrodynamic equations for a collisionless plasma. Under the condition that the drift waves are quasineutral, this set can be reduced to two equations of motion and two continuity equations for the fast and slow plasma ions. Earlier, the method of separating the spectrum of waves with the same dispersion relation into the LF and HF spectral components was used by Rudakov and Tsytovich [8] to investigate the modulational instability of ion acoustic waves.

Our objective here is to derive an expression for the ponderomotive force of an LF field, to study the modulational instability of the drift waves (under the assumption that they are affected by the modulationally unstable LF waves), and to analyze the possible formation of structures in a plasma in the course of modulational processes. The paper is organized as follows. In Section 2, we make the main assumptions and formulate the basic equations. In Section 3, we derive an expression for the ponderomotive force of an LF field. In Section 4, we obtain nonlinear evolutionary equations for the drift waves. In Section 5, we investigate the modulational instability of a drift pump wave. In Section 6, we examine one-dimensional solutions to the nonlinear evolutionary equations. Finally, in Section 7, we discuss the results of our work.

2. BASIC EQUATIONS

We consider an inhomogeneous collisionless plasma in a uniform external magnetic field $\mathbf{B}_0$ and assume that the density of an unperturbed plasma varies in the direction perpendicular to the field $\mathbf{B}_0$. For definiteness, let the z axis be directed along $\mathbf{B}_0$ and let the x axis point in the direction in which an unperturbed plasma is inhomogeneous. In other words, we assume the dependence $n_0 = n_0(x)$. We also introduce the reciprocal of the scale on which the plasma density varies, $\kappa = -d\ln n_0/dx$, where $\kappa > 0$. For simplicity, we assume that the plasma electron temperature T_e is constant. The ion plasma component is assumed to be cold, which corresponds to a highly nonisothermal plasma with $T_e \gg T_i$. We are interested in the processes that occur at frequencies satisfying the inequalities

$$k_z v_{Ti}, \nu_i \ll \omega \ll k_z v_{Te}, \omega_{Li}, \omega_{Bi}, \tag{1}$$

where v_{Ti} and v_{Te} are the thermal velocities of the plasma electrons and ions, ω_{Li} is the ion plasma frequency, and ν_i is the ion–ion collision frequency. Under conditions (1), the electric field in the plasma can be assumed to be potential and the plasma electrons can be described by the Boltzmann distribution

$$n_e = n_0 \exp\left(\frac{e\phi}{T_e}\right). \tag{2}$$

Here and below, the temperature is in energy units. The electric field strength $\mathbf{E}$ is expressed in terms of the potential ϕ by the familiar relationship $\mathbf{E} = -\nabla\phi$.

Under the conditions such that the plasma dimensions are much larger than the electron Debye radius $r_{De} \approx v_{Te}/\omega_{Le}$, the plasma on the spatial scales of the drift perturbations ($l \gg r_{De}$) can be treated as quasineutral, $n_e = n_i = n$.

The cold plasma ions are described by the one-fluid hydrodynamic equations, namely, the ion continuity equation

$$\partial_t n_i + \nabla \cdot (n_i \mathbf{v}) = 0 \tag{3}$$

and the equation of ion motion

$$\partial_t \mathbf{v} + (\mathbf{v} \cdot \nabla)\mathbf{v} = \frac{e}{m_i}\mathbf{E} + \mathbf{v} \times \boldsymbol{\omega}_{Bi}, \tag{4}$$

where $\boldsymbol{\omega}_{Bi} = e\mathbf{B}_0/m_i c$ is the ion gyrofrequency. The plasma quasineutrality condition and the Boltzmann distribution for electrons close the set of Eqs. (3) and (4) with respect to the unknown quantities.

3. PONDEROMOTIVE FORCE OF THE LOW-FREQUENCY POTENTIAL FIELD

Under the above assumptions, the modulational instability of the drift waves is associated with the ponderomotive force of the LF field in a plasma. That is why, following [2], we first generalize previous results obtained on the mean ponderomotive force to the three-dimensional case of an inhomogeneous magnetized plasma. We expand all the quantities in powers of the small parameter $\varepsilon = e\phi/T_e$, which indicates that each of them is represented as

$$f = \sum_n \varepsilon^n f_{(n)}. \tag{5}$$

Thus, the plasma density has the form $n = n_0(x) + \varepsilon n_{(1)} + \varepsilon^2 n_{(2)} + \ldots$, where $n_0(x) \equiv n_{(0)}$ is the unperturbed plasma density. The first terms in the expansions of the remaining quantities are first-order in the perturbed field.

To first order in the dimensionless parameter ε, we obtain the equations

$$\mathbf{E}_{(1)} = -\frac{T_e}{e}\nabla\left(\frac{n_{(1)}}{n_0}\right), \tag{6}$$

$$\partial_t n_{(1)} + \nabla \cdot (n_0 \mathbf{v}_{(1)}) = 0, \tag{6'}$$

$$\partial_t \mathbf{v}_{(1)} = \frac{e}{m_i}\mathbf{E}_{(1)} + \mathbf{v}_{(1)} \times \boldsymbol{\omega}_{Bi}, \quad (6'')$$

$$\mathbf{E}_{(1)} = -\nabla\phi_{(1)}, \quad (6''')$$

in which all first-order quantities are represented as

$$\begin{aligned}
\mathbf{E}_{(1)} &= \frac{1}{2}(\mathbf{E}_1 + \mathbf{E}_1^*) = \frac{1}{2}\mathbf{E}_{(1)}^0 e^{-i\omega t + i\mathbf{kr}} + \text{c.c.} \\
\mathbf{v}_{(1)} &= \frac{1}{2}(\mathbf{v}_1 + \mathbf{v}_1^*) = \frac{1}{2}\mathbf{v}_{(1)}^0 e^{-i\omega t + i\mathbf{kr}} + \text{c.c.} \\
n_{(1)} &= \frac{1}{2}(n_1 + n_1^*) = \frac{1}{2}n_{(1)}^0 e^{-i\omega t + i\mathbf{kr}} + \text{c.c.} \\
\phi_{(1)} &= \frac{1}{2}(\phi_1 + \phi_1^*) = \frac{1}{2}\phi_{(1)}^0 e^{-i\omega t + i\mathbf{kr}} + \text{c.c.}
\end{aligned} \quad (7)$$

We also represent all vector quantities as the sum of the transverse and longitudinal components, $\mathbf{E}_1 = \mathbf{E}_{1\perp} + E_{1z}\mathbf{i}_z$ and $\mathbf{v}_1 = \mathbf{v}_{1\perp} + v_{1z}\mathbf{i}_z$, where $\mathbf{i}_z$ is a unit vector pointing in the z direction. Then, the solution to Eqs. (6) can be written in the form

$$\begin{aligned}
\mathbf{E}_1 &= -i\mathbf{k}\phi_1, \\
\mathbf{v}_{1\perp} &= \frac{e}{m_i}\frac{1}{\omega_{Bi}^2 - \omega^2}(-i\omega\mathbf{E}_{1\perp} + \mathbf{E}_{1\perp} \times \boldsymbol{\omega}_{Bi}), \\
v_{1z} &= \frac{ie}{m_i\omega}E_{1z}, \\
\frac{n_1}{n_0} &= \frac{e\phi_1}{T_e}.
\end{aligned} \quad (8)$$

Here, the frequency ω and wave vector $\mathbf{k}$ satisfy the dispersion relation

$$D(\omega, \mathbf{k}) = \omega^2(1 + k_\perp^2\rho_s^2) - \omega_*\omega - k_z^2 v_s^2 = 0, \quad (9)$$

where $\omega_* = k_y v_0$, $v_0 = \kappa v_s^2/\omega_{Bi}$, $v_s = \sqrt{T_e/m_i}$ is the ion acoustic speed, and $\rho_s = v_s/\omega_{Bi}$ is the effective ion gyroradius. Note that dispersion relation (9) was derived in the limit $\omega \ll \omega_{Bi}$.

To second order in ε, we obtain the equations

$$\mathbf{E}_{(2)} = -\frac{T_e}{e}\nabla\left(\frac{n_{(2)}}{n_0} - \frac{1}{2}\frac{n_{(1)}^2}{n_0^2}\right), \quad (10)$$

$$\partial_t n_{(2)} + \nabla \cdot (n_0\mathbf{v}_{(2)} + n_{(1)}\mathbf{v}_{(1)}) = 0, \quad (10')$$

$$\partial_t \mathbf{v}_{(2)} + (\mathbf{v}_{(1)} \cdot \nabla)\mathbf{v}_{(1)} = \frac{e}{m_i}\mathbf{E}_{(2)} + \mathbf{v}_{(2)} \times \boldsymbol{\omega}_{Bi}. \quad (10'')$$

Since we are interested in steady solutions, we average Eqs. (10) over time, assuming that the averaged quantities satisfy the relationships $\langle\partial_t f\rangle = \partial_t\langle f\rangle = 0$.

This averaging procedure allows us to simplify Eqs. (10)–(10'') in such a way that the electric field $\mathbf{E}_2$ can be determined from Eq. (10''); the velocity $\mathbf{v}_2$, from Eq. (10'); and the density $n_{(2)}$, from Eq. (10). As a result, we arrive at the expressions

$$\langle\mathbf{E}_{(2)}\rangle = -\frac{T_e}{e}\nabla\left(\frac{\langle n_{(2)}\rangle}{n_0} - \frac{1}{2}\frac{\langle n_{(1)}^2\rangle}{n_0^2}\right), \quad (11)$$

$$\langle\mathbf{E}_{(2)}\rangle = \frac{m_i}{e}[\langle(\mathbf{v}_{(1)} \cdot \nabla)\mathbf{v}_{(1)}\rangle - \langle\mathbf{v}_{(2)} \times \boldsymbol{\omega}_{Bi}\rangle], \quad (12)$$

$$\langle\mathbf{v}_{(2)}\rangle = -\frac{\langle n_{(1)}\mathbf{v}_{(1)}\rangle}{n_0}. \quad (13)$$

In the general case, the averaged velocity $\langle\mathbf{v}_{(2)}\rangle$ is determined to within a vector $\mathbf{f}$ satisfying the condition $\nabla \cdot \mathbf{f} = 0$. We restrict ourselves to a forced solution, specifically, the one for which $\mathbf{f} = 0$. Inserting $\langle\mathbf{v}_{(2)}\rangle$ into expression (12) and taking into account first-order solutions (8) yields the averaged electric field in the plasma,

$$\begin{aligned}
\langle\mathbf{E}_{(2)}\rangle &= \frac{m_i}{4e}\nabla\left|\mathbf{v}_{(1)}^0\right|^2 \\
&= \frac{e}{4m_i}\nabla\left[\frac{\omega_{Bi}^2 + \omega^2}{(\omega_{Bi}^2 - \omega^2)^2}\left|\mathbf{E}_{(1)\perp}^0\right|^2 + \frac{1}{\omega^2}\left|E_{(1)z}^0\right|^2\right],
\end{aligned} \quad (14)$$

which produces the averaged ponderomotive force $\langle\mathbf{F}\rangle = e\langle\mathbf{E}_{(2)}\rangle$. The electric field potential has the form

$$\begin{aligned}
\langle\phi_{(2)}\rangle &= -\frac{m_i}{4e}\left|\mathbf{v}_{(1)}^0\right|^2 \\
&= -\frac{e}{4m_i}\left[\frac{\omega_{Bi}^2 + \omega^2}{(\omega_{Bi}^2 - \omega^2)^2}\left|\mathbf{E}_{(1)\perp}^0\right|^2 + \frac{1}{\omega^2}\left|E_{(1)z}^0\right|^2\right] \\
&= -\frac{e\mu}{4T_e}\left|\phi_{(1)}^0\right|^2,
\end{aligned} \quad (15)$$

where we have introduced the notation

$$\mu = v_s^2\left(\frac{\omega_{Bi}^2 + \omega^2}{(\omega_{Bi}^2 - \omega^2)^2}k_\perp^2 + \frac{k_z^2}{\omega^2}\right). \quad (16)$$

For $\omega \ll \omega_{Bi}$, we obtain $\mu \approx \rho_s^2 k_\perp^2 + k_z^2 v_s^2/\omega^2$.

Now, we discuss the difference between the force of an LF field and the ponderomotive force [10] and their common features. In a strong HF field, it is only the plasma electrons that oscillate under the action of this field, whereas the ions undergo a slow motion driven by the ponderomotive force. Otherwise, in a strong LF field, only cold plasma ions oscillate, while electrons have enough time to acquire a Boltzmann distribution. Nevertheless, in both cases, the mean force causes precisely the same effect: the plasma is expelled from the region of the strong field. This effect is easy to demonstrate using the time-averaged second-order equations.

Integrating expression (12) with allowance for Boltzmann distribution (11) yields Bernoulli's equation

$$2T_e\langle n_{(2)}\rangle + \frac{\rho_i\left|\mathbf{v}^0_{(1)}\right|^2}{2} - \frac{\left|\phi^0_{(1)}\right|^2}{8\pi r_{De}^2} = \text{const}, \qquad (17)$$

in which the left-hand side is constant along the lines of the external magnetic field $\mathbf{B}_0$. Here, $\rho_i = n_0 m_i$ is the ion plasma density and $r_{De} = \sqrt{T_e/(4\pi e^2 n_0)}$ is the electron Debye radius. The factor 2 in front of the gas-kinetic electron pressure $P_e = T_e\langle n_{(2)}\rangle$ stems from an averaging of the oscillations of the kinetic and potential energies ($\rho_i\left|\mathbf{v}^0_{(1)}\right|^2/2$ and $\left|\phi^0_{(1)}\right|^2/8\pi r_{De}^2$, respectively) over the unit volume. We can see that the second term on the left-hand side of Bernoulli's equation is associated with the ponderomotive force because this term is the force potential to within a constant factor. The third term accounts for the potential interaction, which leads to the opposite effect: the plasma is drawn into the region of the strong field. These two competing effects govern the sign of the plasma density fluctuations $\langle n_{(2)}\rangle$. For $\mu > 1$, the plasma is expelled from the region of the strong field, whereas, for $\mu < 1$, the plasma is drawn into this region. To conclude the discussion, note that Bernoulli's equation (17) was derived from the general hydrodynamic equations; hence, the results obtained are valid over the entire applicability range of the hydrodynamic approach.

4. NONLINEAR EVOLUTIONARY EQUATIONS

The plasma density modulation considered above can give rise to the modulational instability of a drift wave. We consider a drift wave $\tilde{\phi}$ propagating in a plasma and having the frequency ω_0, wavenumber $\mathbf{k}_0$, and amplitude ψ:

$$\tilde{\phi} = \psi e^{-i\omega_0 t + i\mathbf{k}_0\cdot\mathbf{r}}, \qquad (18)$$

where $\psi = \psi(\mathbf{r}, t)$ is the wave envelope amplitude.

In order to derive the nonlinear evolutionary equations, we assume that there exists a hierarchy of time scales, which indicates that the fast and slow processes occurring in the plasma can be studied separately. Note that the method of separating the spectrum of waves of the same nature into the LF and HF components was used in investigating modulational processes in a medium with an anomalous dispersion [8, 9, 11] and the modulational instability of ion acoustic waves [12, 13].

Below, the rapidly varying quantities will be denoted by a tilde and a superior bar will mark the slowly varying quantities. Using the standard method of separating the fast and slow processes [1], we arrive at the equations for slow motions,

$$\partial_t\bar{\eta} - \kappa\bar{v}_x + \nabla\bar{\mathbf{v}} = \kappa\langle\tilde{\eta}\tilde{v}_x\rangle - \nabla\langle\tilde{\eta}\tilde{\mathbf{v}}\rangle \qquad (19)$$

$$\partial_t\bar{\mathbf{v}} + \langle(\tilde{\mathbf{v}}\nabla)\tilde{\mathbf{v}}\rangle = -v_s^2\nabla\bar{\eta} + \frac{1}{2}v_s^2\nabla\langle\tilde{\eta}^2\rangle + \bar{\mathbf{v}}\times\boldsymbol{\omega}_{Bi}, \qquad (20)$$

and the equations for fast motions,

$$\partial_t\tilde{\eta} - \kappa\tilde{v}_x + \nabla\tilde{\mathbf{v}} = \kappa\bar{\eta}\tilde{v}_x + \kappa\tilde{\eta}\bar{v}_x - \nabla(\bar{\eta}\tilde{\mathbf{v}} + \tilde{\eta}\tilde{\mathbf{v}}) \qquad (21)$$

$$\partial_t\tilde{\mathbf{v}} + \boldsymbol{\sigma} = -v_s^2\nabla\tilde{\eta} + \tilde{\mathbf{v}}\times\boldsymbol{\omega}_{Bi}. \qquad (22)$$

Here, the nondimensionalized perturbations of the plasma density ($\tilde{\eta}$ and $\bar{\eta}$) are defined by the relationship $n/n_0 = 1 + \tilde{\eta} + \bar{\eta}$.

In what follows, we will be interested primarily in drift waves propagating nearly perpendicular to the external magnetic field, because such waves are most important from the standpoint of plasma confinement. Under the conditions $k_z v_s \ll \omega \ll \omega_{Bi}$, we can neglect the Reynolds term $\boldsymbol{\sigma} = (\bar{\mathbf{v}}\nabla)\tilde{\mathbf{v}} + (\tilde{\mathbf{v}}\nabla)\bar{\mathbf{v}}$ in Eq. (22) and can consider a two-dimensional case such that $\partial_z = 0$.

The equations for slow motions yield the following equation for an LF drift wave:

$$\begin{aligned}&[\partial_t(1-\rho_s^2\Delta_\perp) + v_0\partial_y]\bar{\eta}\\ &= \frac{1}{4}(1-\mu)\frac{e^2}{T_e^2}[v_0\partial_y - \rho_s^2\Delta_\perp\partial_t]|\psi|^2\\ &-\frac{e^2\rho_s^2}{2T_e^2}\frac{\omega_0}{\omega_{Bi}}([\mathbf{k}_{0\perp}\times\nabla_\perp]_z + \kappa k_{0y})\partial_t|\psi|^2.\end{aligned} \qquad (23)$$

This LF wave is driven by the modulational instability of the HF drift wave $\tilde{\phi}$. Here, the quantity μ is defined in notation (16), introduced for an HF drift wave, and is approximately equal to $\mu \approx \rho_s^2 k_{0\perp}^2$. The first term on the right-hand side of Eq. (23) accounts for the ponderomotive effect described by Bernoulli's equation (17). The second term corresponds to the drift $\langle(\tilde{\mathbf{v}}\cdot\nabla)\tilde{\mathbf{v}}\rangle$ in the pump wave field and is of the higher order in the small parameter ω_0/ω_{Bi}.

From the second pair of the equations, namely, Eqs. (21) and (22), we can derive the evolutionary equation for an HF drift wave:

$$\begin{aligned}&[\partial_t(1-\rho_s^2\Delta_\perp) + v_0\partial_y]\tilde{\phi}\\ &= -v_0\partial_y(\bar{\eta}\tilde{\phi}) + \rho_s^2\nabla_\perp(\bar{\eta}\nabla_\perp\partial_t\tilde{\phi}).\end{aligned} \qquad (24)$$

Since the slowly varying amplitude ϕ satisfies the conditions

$$\left|\frac{\partial_t\psi}{\omega_0\psi}\right| \ll 1, \quad \left|\frac{\partial_i\psi}{k_i\psi}\right| \ll 1, \qquad (25)$$

we arrive at the final equation describing the evolution of the amplitude of the envelope of an HF drift wave:

$$\begin{aligned}&\partial_t\psi + \mathbf{v}_{g\perp}\cdot\nabla_\perp\psi + ia\Delta_\perp\psi \\ &= -ib(\bar{\eta}\psi) - \mathbf{v}_{g\perp}\cdot\nabla_\perp(\bar{\eta}\psi) - a\psi\mathbf{k}_{0\perp}\cdot\bar{\eta}.\end{aligned} \tag{26}$$

Here, we have introduced the notation $a = \omega_0^2\rho_s^2/(v_0k_{0y})$ and $b = a/\rho_s^2$. The group velocity of the drift wave is described by the expression

$$\mathbf{v}_{g\perp} = \frac{\partial\omega_0}{\partial\mathbf{k}_{0\perp}} = a\left(-2k_{0x}, \frac{v_0}{\omega_0\rho_s^2} - 2k_{0y}\right), \tag{27}$$

in which the frequency ω_0 and wave vector $\mathbf{k}$ are related by the dispersion relation. The two nonlinear equations (23) and (26) make it possible to describe the excitation of LF drift waves due to the modulational instability of HF drift waves. Below, we will consider the linear stage of this process. It should be mentioned parenthetically that, in terms of the familiar Hasegawa–Mima equation, it is possible to describe only the modulational instability of a convective cell, accompanied by the excitation of a drift wave.

5. MODULATIONAL INSTABILITY

Before proceeding to a description of the linear stage of the modulational instability, we consider an unperturbed state described by the above nonlinear equations. We assume that, in the absence of perturbations, the quantities η and $|\psi|^2$ are independent of the coordinate $\mathbf{r}$ and time t. All the unperturbed quantities will carry the subscript 0. We represent ψ_0 in the form corresponding to a plane monochromatic wave:

$$\psi_0 = \psi_0^0 e^{-i\Omega t + i\Delta\mathbf{k}\cdot\mathbf{r}}. \tag{28}$$

Then, from Eq. (26), it follows that the frequency Ω and wave vector $\Delta\mathbf{k}$ satisfy the dispersion relation

$$\Omega = \mathbf{v}_{g\perp}\cdot\Delta\mathbf{k}_\perp - a\Delta k_\perp^2 + b + \mathbf{v}_{g\perp}\cdot\Delta\mathbf{k}_\perp\eta_0. \tag{29}$$

The instability gives rise to small perturbations, so that we can write $\eta = \eta_0 + \delta\eta$, $\psi = \psi_0 + \delta\psi$, and $\psi^* = \psi_0^* + \delta\psi^*$. We linearize the initial nonlinear equations with respect to the small perturbations $\delta\eta$, $\delta\psi$, and $\delta\psi^*$ and represent the perturbations in the form

$$\begin{aligned}\delta\eta &= \delta\bar{\eta}e^{-i\omega t + i\mathbf{kr}}, \\ \delta\psi &= \delta\bar{\psi}e^{-i(\omega+\Omega)t + i(\mathbf{k}+\Delta\mathbf{k})\mathbf{r}}, \\ \delta\psi^* &= \delta\bar{\psi}^*e^{-i(\omega-\Omega)t + i(\mathbf{k}-\Delta\mathbf{k})\mathbf{r}}.\end{aligned} \tag{30}$$

Substituting expressions (30) into the linearized equations, we obtain the dispersion relation for the modulational instability:

$$\begin{aligned}&(\omega-\omega_d)[(\omega-\mathbf{v}_{g\perp}\cdot\mathbf{k}_\perp)^2 - a^2k_\perp^4] \\ &= \left(\frac{1}{2}(1-\mu)(\omega\rho_s^2k_\perp^2 - v_0k_y)\right. \\ &\left. - \rho_s^2\omega\frac{\omega_0}{\omega_{Bi}}(i[\mathbf{k}_{0\perp}\times\mathbf{k}_\perp]_z + \kappa k_{0y})\right) \\ &\times\frac{(\omega-\mathbf{v}_{g\perp}\cdot\mathbf{k}_\perp)[\mathbf{v}_{g\perp}\cdot\mathbf{k}_\perp + a(\mathbf{k}_{0\perp}\cdot\mathbf{k}_\perp)] - abk_\perp^2}{1+\rho_s^2k_\perp^2}\frac{e^2}{T_e^2}|\psi_0^0|^2.\end{aligned} \tag{31}$$

In deriving the dispersion relation, we assumed the following hierarchies of spatial and time scales: $\Delta k \ll k \ll k_0$ and $\Omega \ll \omega \ll \omega_0 \ll \omega_B$. The drift waves excited in the case under analysis have the frequency $\mathrm{Re}\,\omega$ and wave vector $\mathbf{k}_\perp$, which satisfy dispersion relation (9) with $k_z = 0$. We assume that the frequency is approximately equal to $\mathrm{Re}\,\omega \approx \omega_d$, where

$$\omega_d = \frac{v_0k_y}{1+\rho_s^2k_\perp^2}, \tag{32}$$

and that the instability growth rate $\gamma_{\mathrm{mod}} = \mathrm{Im}\,\omega$ is much lower than the frequency ω_d.

We restrict ourselves to considering the long-wavelength limit in which $\rho_s^2k_\perp^2 \ll 1$ and the frequency is approximately equal to $\omega_d \approx v_0k_y$. Since dispersion relation (31) is similar in structure to the dispersion relation for the well-studied beam instability in the plasma, we can draw an analogy with the Cherenkov instability. First, we consider the solutions to dispersion relation (31) that satisfy the resonance condition

$$\omega_d = \mathbf{v}_{g\perp}\cdot\mathbf{k}_\perp. \tag{33}$$

We can see that the group velocity of a modulationally unstable drift pump wave plays the same role as the beam velocity in the Cherenkov instability. It is assumed that the modulational instability develops at the resonant frequency; hence, we can write $\omega = \omega_d + \delta\omega$. We neglect the small term on the order of ω_0/ω_{Bi} on the right-hand side of dispersion relation (31) in order to rewrite it as the following equation with respect to $\delta\omega$:

$$\begin{aligned}&\delta\omega(\delta\omega^2 - a^2k_\perp^4) \\ &= -\frac{1}{2}(1-\mu)\omega_d b\left[\left(1+\frac{1}{2}\mu\right)\frac{\omega_d}{\omega_0}\delta\omega - ak_\perp^2\right]\frac{e^2}{T_e^2}|\psi_0^0|^2,\end{aligned} \tag{34}$$

where $\mu = \rho_s^2 k_{0\perp}^2$. Equation (34) has complex solutions when the pump wave amplitude $|\psi_0^0|$ is larger than the critical value defined by the inequality

$$\frac{3}{\sqrt[3]{16}}[(1-\mu)\omega_d ab]^{2/3}\left(k_\perp \frac{e}{T_e}|\psi_0^0|\right)^{4/3} + \frac{1}{4}(1-\mu)\frac{2+\mu}{1+\mu}\omega_d^2\frac{e^2}{T_e^2}|\psi_0^0|^2 > a^2 k_\perp^4. \quad (35)$$

As in the case of the nonlinear Schrödinger equation, condition (35) for the onset of the instability serves as a relationship between the absolute value of the wavenumber and the wave amplitude.

Now, we consider particular cases of Eq. (34) with different values of the wavenumber. Note that resonance condition (33) determines only the propagation direction of the excited drift wave and does not impose any restrictions on the absolute value of its wave vector. For $a^2 k_\perp^4 \gg (\delta\omega)^2$, Eq. (34) has no complex solutions. For $\omega_d|\delta\omega|/\omega_0 \ll a k_\perp^2$, Eq. (34) reduces to the equation

$$\delta\omega[(\delta\omega)^2 - a^2 k_\perp^4] = \frac{1}{2}(1-\mu)\omega_d ab k_\perp^2 \frac{e^2}{T_e^2}|\psi_0^0|^2, \quad (36)$$

which has complex solutions under the condition

$$\rho_s^2 k_\perp^2 < \frac{\sqrt{3\sqrt{3}}}{2}\sqrt{|1-\mu^2|}\left(\frac{\omega_d}{\omega_0}\right)^{1/2}\frac{e}{T_e}|\psi_0^0|. \quad (37)$$

We introduce the dimensionless quantity ξ through the relationship

$$(a k_\perp^2)^2 = \frac{3\sqrt{3}}{4}|1-\mu|\omega_d b\frac{e^2}{T_e^2}|\psi_0^0|^2\xi^2. \quad (38)$$

Under condition (37), the quantity ξ lies within the unit interval, $0 < \xi < 1$. The instability growth rate as a function of ξ has the form

$$\gamma_{\rm mod}(\xi) = \frac{\sqrt{3\sqrt{3}}}{4}\sqrt{\frac{|1-\mu|}{1+\mu}\omega_d\omega_0}\frac{e}{T_e}|\psi_0^0| f(\xi), \quad (39)$$

where

$$f(\xi) = (\xi + \sqrt{\xi^2 - \xi^6})^{1/3} - (\xi - \sqrt{\xi^2 - \xi^6})^{1/3}. \quad (40)$$

The plot of function (40) is shown in the figure.

The maximum growth rate, $\gamma_{\rm mod}^{\max}$, is reached at $\xi = \xi_{\max} = 0.41$ and is equal to

$$\gamma_{\rm mod}^{\max} = 0.43\sqrt{\frac{|1-\mu|}{1+\mu}\omega_d\omega_0}\frac{e}{T_e}|\psi_0^0|. \quad (41)$$

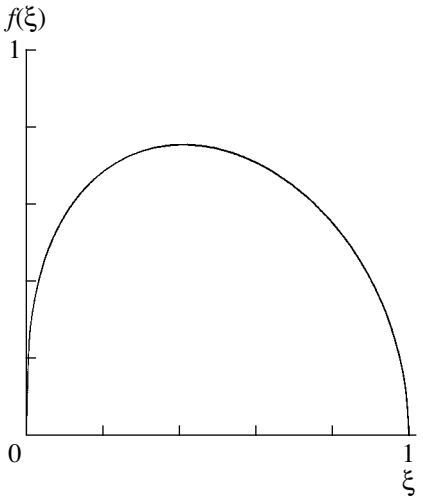

Plot of the function $f(\xi) = (\xi + \sqrt{\xi^2 - \xi^6})^{1/3} - (\xi - \sqrt{\xi^2 - \xi^6})^{1/3}$.

The solutions obtained are applicable under the condition

$$\frac{\xi}{f(\xi)} \gg \frac{\omega_d}{\omega_0}. \quad (42)$$

The smallness of the right-hand side of this condition permits it to be simplified to $\xi \gg (\omega_d/\omega_0)^{3/2}$.

For $a k_\perp^2 \ll |\delta\omega|\omega_d/\omega_0$, dispersion relation (34) reduces to the quadratic equation

$$(\delta\omega)^2 = -\frac{1}{4}(1-\mu)\frac{2+\mu}{1+\mu}\omega_d^2\frac{e^2}{T_e^2}|\psi_0^0|^2, \quad (43)$$

which has complex solutions only for $\mu < 1$. In this case, the instability growth rate is equal to

$$\gamma_{\rm mod} = \frac{1}{2}\omega_d\sqrt{\frac{1-\mu}{1+\mu}(2+\mu)}\frac{e}{T_e}|\psi_0^0|. \quad (44)$$

In terms of $\rho_s^2 k_\perp^2$, the condition for the applicability of this solution has the form

$$\rho_s^2 k_\perp^2 \ll \sqrt{1-\mu^2}\left(\frac{\omega_d}{\omega_0}\right)^2\frac{e}{T_e}|\psi_0^0|. \quad (45)$$

Since $\omega_d = v_0 k_y \approx v_0 k_\perp$, this condition imposes a lower limit on the pump wave amplitude,

$$\frac{e}{T_e}|\psi_0^0| \gg \left(\frac{\omega_0\rho_s}{v_0}\right)^2(1-\mu^2)^{-1/2}, \quad (46)$$

which determines the instability threshold for superlong drift waves.

Pursuing the analogy with beam instability, we can say that, under resonance condition (33), the above

solutions correspond to those describing the single-particle Cherenkov effect or, more correctly, the Thomson excitation mechanism. In addition, there also exists the collective Cherenkov effect or, in the general case, the Raman excitation mechanism. In order to consider the corresponding case in our problem, we introduce the detuning Δ of the wave frequency from the resonant frequency:

$$\omega_d = \mathbf{v}_{g\perp}\cdot\mathbf{k}_\perp + \Delta. \tag{47}$$

The case $|\delta\omega| \gg |\Delta|$ is not of great interest because it leads to the solutions that have been obtained above and contain a small correction on the order of $|\Delta/\delta\omega|$. That is why we consider only the case $|\delta\omega| \ll |\Delta|$, in which dispersion relation (47) becomes

$$\begin{aligned}&\delta\omega(2\Delta\delta\omega + \Delta^2 - a^2k_\perp^4)\\ &= -\frac{1}{2}(1-\mu)\omega_d\left[\frac{1}{2}\Delta\left(\omega_d\frac{2+\mu}{1+\mu}-\Delta\right) - abk_\perp^2\right]\frac{e^2}{T_e^2}\left|\psi_0^0\right|^2.\end{aligned} \tag{48}$$

The conditions under which the complex solutions exist have the form

$$\begin{aligned}&(\mu-1)\,\mathrm{sgn}\,\Delta > 0,\\ &\left|\Delta \mp ak_\perp^2\right| < \sqrt{\mp(1-\mu)\omega_d b}\frac{e}{T_e}\left|\psi_0^0\right|.\end{aligned} \tag{49}$$

The latter inequality indicates that the modulational instability develops only in narrow intervals of Δ around $\pm ak_\perp^2$. In other words, there exist resonance conditions on the detuning Δ.

The growth rate, which is the largest at $\Delta = -ak_\perp^2 < 0$ and $\mu < 1$ (or at $\Delta = ak_\perp^2 < 0$ and $\mu > 1$), is equal to

$$\gamma_{\mathrm{mod}}^{\max} = \frac{1}{2}\sqrt{\frac{|1-\mu|}{1+\mu}\omega_d\omega_0}\frac{e}{T_e}\left|\psi_0^0\right|. \tag{50}$$

In this case, the condition $|\Delta| \gg |\delta\omega|$ takes the form

$$\rho_s^2k_\perp^2 \gg \sqrt{|1-\mu^2|}\left(\frac{\omega_d}{\omega_0}\right)^{1/2}\frac{e}{T_e}\left|\psi_0^0\right|. \tag{51}$$

To conclude this section, we consider the very nonresonant case in which the drift wave branch $\omega_1 = \omega_d$ and the soliton mode branch $\omega_2 = \mathbf{v}_{g\perp}\cdot\mathbf{k}_\perp \pm ak_\perp^2$ are very different, $\omega_1 \neq \omega_2$. For drift waves, we represent the solutions to dispersion relation (31) as $\omega = \omega_d + \delta\omega$, whereas for soliton modes, we seek the solutions in the form $\omega = \omega_2 + \delta\omega$. As a result, we obtain the growth rate of the instability at the frequency of the drift wave,

$$\begin{aligned}\gamma_{\mathrm{drift}} &= -\omega_d\frac{\omega_0}{\omega_{Bi}}\rho_s^2[\mathbf{k}_{0\perp}\times\mathbf{k}_\perp]_z\\ &\times\frac{(\omega_d - \mathbf{v}_{g\perp}\cdot\mathbf{k}_\perp)[\mathbf{v}_{g\perp}\cdot\mathbf{k}_\perp + a\mathbf{k}_{0\perp}\cdot\mathbf{k}_\perp] - abk_\perp^2}{(\omega_d - \mathbf{v}_{g\perp}\cdot\mathbf{k}_\perp)^2 - a^2k_\perp^4}\frac{e^2}{T_e^2}\left|\psi_0^0\right|^2,\end{aligned} \tag{52}$$

and the instability growth rate for the soliton structures,

$$\gamma_{\mathrm{soliton}} = \pm\frac{b}{2}\frac{\omega_2}{\omega_2-\omega_1}\frac{\omega_0}{\omega_{Bi}}\rho_s^2[\mathbf{k}_{0\perp}\times\mathbf{k}_\perp]_z\frac{e^2}{T_e^2}\left|\psi_0^0\right|^2. \tag{53}$$

6. ONE-DIMENSIONAL SOLUTIONS

We begin by discussing the case $\partial_y \longrightarrow 0$, i.e., the generation of one-dimensional flows stretched along the *y* coordinate (the so-called zonal flows). The dispersion relation for long-wavelength ($\rho_s^2k_\perp^2 \ll 1$) perturbations reduces to

$$\begin{aligned}&(\omega - v_{gx}k_x)^2 - a^2k_x^4\\ &= \left[\frac{1}{2}(1-\mu)\rho_s^2k_x^2 - \frac{\omega_0}{\omega_{Bi}}\rho_s^2k_{0y}(\kappa - ik_x)\right]\\ &\times\left[\frac{1}{2}(\omega - v_{gx}k_x)v_{gx}k_x - abk_x^2\right]\frac{e^2}{T_e^2}\left|\psi_0^0\right|^2.\end{aligned} \tag{54}$$

We seek a solution in the form

$$\omega = v_{gx}k_x \pm ak_x^2 + \delta\omega. \tag{55}$$

With respect to $\delta\omega$, dispersion relation (54) can be rewritten as

$$\begin{aligned}&(\delta\omega)^2 \pm 2ak_x^2\delta\omega\\ &= \left[\frac{1}{2}(1-\mu)\rho_s^2k_x^2 - \frac{\omega_0}{\omega_{Bi}}\rho_s^2k_{0y}(\kappa - ik_x)\right]\\ &\times\left[\frac{1}{2}(\pm ak_x^2 + \delta\omega)v_{gx}k_x - abk_x^2\right]\frac{e^2}{T_e^2}\left|\psi_0^0\right|^2.\end{aligned} \tag{56}$$

In the case $|\delta\omega| \ll ak_x^2$, the correction to the frequency is equal to

$$\begin{aligned}\delta\omega &= \mp\frac{1}{2}\left[\frac{1}{2}(1-\mu)\rho_s^2k_x^2\right.\\ &\left.+\frac{\omega_0}{\omega_{Bi}}\rho_s^2k_{0y}(ik_x - \kappa)\right]b\frac{e^2}{T_e^2}\left|\psi_0^0\right|^2,\end{aligned} \tag{57}$$

and the instability growth rate is

$$\gamma_{\text{mod}} = \pm\frac{1}{2}\frac{\omega_0^3}{\omega_{Bi}^2}\frac{k_x}{\kappa}\frac{e^2}{T_e^2}\left|\psi_0^0\right|^2. \quad (58)$$

This indicates that only solitons propagating in the positive direction of the x axis are amplified. This situation is analogous to the pattern of waves on shallow water of varying depth. In the case at hand, the role of the water depth is played by the plasma density.

The condition $|\delta\omega| \ll ak_x^2$ is satisfied when

$$k_x \gg \frac{\omega_0}{\omega_{Bi}}k_{0y}\frac{e^2}{T_e^2}\left|\psi_0^0\right|^2. \quad (59)$$

We consider the case

$$ak_x^2 \ll |\delta\omega| \ll \frac{ak_x^2}{\rho_s^2 k_{0x}k_x}, \quad (60)$$

which can occur for small wavenumbers,

$$k_x \ll \left(\frac{\omega_0}{\omega_{Bi}}k_{0y};\ \frac{1}{\rho_s^2 k_{0x}}\right). \quad (61)$$

In this case, we obtain the dispersion relation

$$(\delta\omega)^2 = -\frac{\omega_0}{\omega_{Bi}}\rho_s^2 k_{0y}(ik_x - \kappa)abk_x^2\frac{e^2}{T_e^2}\left|\psi_0^0\right|^2 \quad (62)$$

and the instability growth rate

$$\gamma_{\text{mod}} = \frac{1}{\sqrt{2}}\left(\frac{\omega_0}{\omega_{Bi}}\frac{k_{0y}}{k_x}\right)^{1/2}ak_x^2\frac{e}{T_e}\left|\psi_0^0\right|, \quad (63)$$

so that condition (60) becomes

$$1 \ll \left(\frac{\omega_0}{\omega_{Bi}}\frac{k_{0y}}{k_0}\right)^{1/2}\frac{e}{T_e}\left|\psi_0^0\right| \ll \frac{1}{\rho_s^2 k_{0x}k_x}. \quad (64)$$

For $\left|\rho_s^2\partial_x^2\eta\right| \ll \eta$, we arrive at the dependence

$$\bar{\eta} = A|\psi|^2 + B\partial_x|\psi|^2 + C\partial_x^2|\psi|^2, \quad (65)$$

where

$$A = -\frac{1}{2}\frac{\omega_0}{\omega_{Bi}}\rho_s^2 k_{0y}\kappa\frac{e^2}{T_e^2}, \quad (66)$$

$$B = \frac{1}{2}\frac{\omega_0}{\omega_{Bi}}\rho_s^2 k_{0y}\frac{e^2}{T_e^2}, \quad (67)$$

$$C = -\frac{1}{4}(1-\mu)\rho_s^2\frac{e^2}{T_e^2}. \quad (68)$$

The modified nonlinear Schrödinger equation, which describes the evolution of the wave envelope amplitude, takes the form

$$\begin{aligned}&\partial_t\psi + v_{gx}(1 + A|\psi|^2 + B\partial_x|\psi|^2 + C\partial_x^2|\psi|^2)\partial_x\psi\\ &+ ia\partial_x^2\psi + \psi(\sigma_0 + \sigma_1\partial_x + \sigma_2\partial_x^2 + \sigma_3\partial_x^3)|\psi|^2 = 0,\end{aligned} \quad (69)$$

where

$$\begin{aligned}&\sigma_0 = iAb, \quad \sigma_1 = ibB + \frac{1}{2}v_{gx}A,\\ &\sigma_2 = i\left(bC + \frac{1}{2}v_{gx}B\right), \quad \sigma_3 = \frac{1}{2}v_{gx}C.\end{aligned} \quad (70)$$

Now, we discuss the case $\partial_x \longrightarrow 0$ and $k_x \longrightarrow 0$, i.e., the generation of flows stretched along the x axis (the so-called streamers). We define the frequency detuning from the resonant value through the relationship $\omega_d = v_{gy}k_y + \Delta$. Here, the frequency in the long-wavelength limit $\rho_s^2 k_\perp^2 \ll 1$ is equal to $\omega_d = v_0 k_y$. We insert the quantity v_{gy} into the definition of the detuning to obtain the frequency dependence of Δ:

$$\Delta = \left[2\left(\frac{\omega_0}{\kappa v_s}\right)^2 + \frac{\mu}{1+\mu}\right]\omega_d, \quad (71)$$

where the quantity μ was defined above. For brevity, we introduce the notation $\alpha = \Delta/\omega_d$. In order of magnitude, we have $\alpha \sim \rho_s^2 k_{0y}^2 \sim 1$; consequently, the resonance condition $\Delta = 0$ cannot be satisfied. Taking into account the above conditions, we write dispersion relation (31) in terms of the quantity $\delta\omega = \omega - \omega_d$:

$$\begin{aligned}\delta\omega[(\delta\omega + \Delta)^2 - a^2k_y^4] &= \left[\frac{1}{2}(1-\mu)(\omega\rho_s^2k_y^2 - \omega_d)\right.\\ &\left. - \rho_s^2\omega\frac{\omega_0}{\omega_{Bi}}(ik_{0x}k_y + \kappa k_{0y})\right]\\ &\times\left[(\delta\omega + \Delta)\omega_0 k_y\left(\frac{1}{k_y} - \frac{\omega_0\rho_s^2}{v_0}\right) - abk_y^2\right]\frac{e^2}{T_e^2}\left|\psi_0^0\right|^2.\end{aligned} \quad (72)$$

Note that, since $ak_y^2 = (\omega_0/\kappa v_s)^2\omega_d(k_y/k_{0y})$, the inequality $k_y \ll k_{0y}$ is always satisfied by virtue of $ak_y^2 \ll \Delta$. In the case $|\delta\omega| \ll \Delta$, which corresponds to the excitation of drift waves, dispersion relation (72) simplifies to

$$\begin{aligned}\delta\omega\Delta^2 &= \left[\frac{1}{2}(1-\mu)\omega_d + \rho_s^2\omega_d\frac{\omega_0}{\omega_{Bi}}(ik_{0x}k_y + \kappa k_{0y})\right]\\ &\times\left[abk_y^2 - \omega_0\Delta k_y\left(\frac{1}{k_{0y}} - \frac{\omega_0\rho_s^2}{v_0}\right)\right]\frac{e^2}{T_e^2}\left|\psi_0^0\right|^2,\end{aligned} \quad (73)$$

and the instability growth rate is equal to

$$\gamma_{\text{drift}} = \alpha^2 \frac{\omega_0}{\omega_{Bi}} \frac{k_{0x}}{k_{0y}} \frac{\omega_d^2}{v_0 k_{0y}} \times \left[\left(\frac{\omega_0}{\kappa v_s} \right)^2 \alpha \rho_s^2 k_{0y}^2 - \frac{\omega_0}{\kappa v_s} \alpha \rho_s k_{0y} + \left(\frac{\omega_0}{\kappa v_s} \right)^4 \right] \frac{e^2}{T_e^2} \left| \psi_0^0 \right|^2. \quad (74)$$

The expression in the square brackets is positive for any values of $\rho_s k_{0y}$ under the condition

$$\left(\frac{2\omega_0}{\kappa v_s} \right)^2 > 1 + \sqrt{1 + \frac{4\mu}{1+\mu}}. \quad (75)$$

Under the opposite condition, this expression is positive for

$$\rho_s k_{0y} > \frac{\kappa v_s}{2\omega_0} \left[1 + \sqrt{1 - \frac{4}{\alpha} \left(\frac{\omega_0}{\kappa v_s} \right)^4} \right]. \quad (76)$$

Therefore, there always exist wavenumbers $\mathbf{k}_0$ of the pump wave that lead to the excitation of LF drift waves propagating along the y axis.

In the plasma, there are also wave branches obeying the dispersion relation $\omega_\pm = v_{gy} k_y \pm a k_y^2$. Setting $\delta\omega_\pm = \omega - \omega_\pm \ll |\omega_\pm|$, we arrive at the following dispersion relation with respect to $\delta\omega_\pm$:

$$(\delta\omega_\pm)^2 \pm 2\delta\omega_\pm a k_y^2 = \left[\frac{1}{2}(1-\mu)\omega_d + \rho_s^2 \omega_\pm \frac{\omega_0}{\omega_{Bi}} (i k_{0x} k_y + \kappa k_{0y}) \right] \times \frac{a b k_y^2}{\omega_\pm - \omega_d} \frac{e^2}{T_e^2} \left| \psi_0^0 \right|^2. \quad (77)$$

For $|\delta\omega_\pm| \ll a k_y^2$, the instability growth rates are equal to

$$\gamma_\pm = \pm \frac{1}{2} \omega_\pm \frac{\omega_0}{\omega_{Bi}} \rho_s^2 k_{0x} k_y \frac{b}{\omega_\pm - \omega_d} \frac{e^2}{T_e^2} \left| \psi_0^0 \right|^2. \quad (78)$$

In the opposite case, $|\delta\omega_\pm| \gg a k_y^2$, the instability develops under the condition $\mu < 1$ (by virtue of $\omega_\pm - \omega_d < 0$) at the rate

$$\gamma_\pm = \sqrt{\frac{1}{2}(1-\mu) \frac{\omega_d}{\omega_d - \omega_\pm}} \omega_d \frac{\rho_s k_{0y}}{(1+\mu)^2} \frac{e}{T_e} \left| \psi_0^0 \right|. \quad (79)$$

Hence, the instability growth rate is equal in order of magnitude to the fastest growth rate under the resonance condition.

7. DISCUSSION OF THE RESULTS

Now, we discuss the theoretical results obtained above. We have shown that the linear stage of the modulational instability of a drift wave is described by a dispersion relation that is analogous to the dispersion relation for the Cherenkov instability. Note that drawing such an analogy between the dispersion relations for the modulational instability and stream instabilities is a conventional practice; this point has been discussed in a number of papers (see, e.g., [14, 15]). For a drift wave, the role of the stream velocity is played by the wave group velocity $\mathbf{v}_{g\perp}$, and the role of the density is taken over by the wave amplitude $\left| \psi_0^0 \right|$. Under resonance conditions, both types of instabilities have the largest growth rate. However, the maximum growth rate of the Cherenkov instability is proportional to $n_b^{2/3}$ (where n_b is the beam density), whereas the maximum growth rate of the modulational instability is proportional to $\left| \psi_0^0 \right|$.

The modulational instability of a drift wave plays a significant role as a source of long-wavelength low-frequency perturbations only when its maximum growth rate exceeds the growth rates of the other linear instabilities. There are at least two linear mechanisms for the excitation of drift waves. The first one is the mechanism for Cherenkov dissipation by thermal electrons, whose damping rate may change its sign in the drift frequency range, thus resulting in instability. Under conditions (1) and the condition $k_z \ll \{\omega/v_s, k_\perp\}$, the growth rate of this instability is described by the formula

$$\gamma_L = \sqrt{\frac{\pi}{2}} \frac{\omega_d^2}{|k_z| v_{Te}} (r_{De}^2 + \rho_s^2) k_\perp^2. \quad (80)$$

For the maximum growth rate (41) and the corresponding wavenumber, we see that the modulational instability is dominant under the condition $|k_z| v_s > (m_e/m_i)(\omega_d/\omega_0)\omega_d$.

The second mechanism is the beam instability with the growth rate

$$\gamma_L = \sqrt{\pi} \omega_d \frac{u}{v_{Te}} \quad (81)$$

under the conditions $\rho_s^2 k_\perp^2 \ll 1$ and $\omega_d \gg k_z v_s$. Here, u is the directed velocity of the electrons carrying an electric current. Setting $u \approx I_p/\pi n e R^2$ and considering an actual tokamak with the toroidal plasma current $I_p = 1.4$ MA, major radius $R = 0.77$ m, plasma density $n = 3.5 \times 10^{19}$ m^{-3}, and electron temperature $T_e \sim 100$ eV, we obtain an estimate according to which the modulational instability is dominant when the amplitude of the drift pump wave satisfies the inequality

$$\frac{e}{T_e} \left| \psi_0^0 \right| > 0.1 \left(\frac{\omega_d}{\omega_0} \right)^{1/2}. \quad (82)$$

We can see that, in the long-wavelength low-frequency limit, the drift waves are excited by the modulational

instability more efficiently than by other linear instabilities.

Real devices suffer anomalous transport of matter across the magnetic field in the wall plasma regions. Experimental investigations revealed that the genuine diffusion coefficient is larger than the theoretically predicted one. Thus, in the linear theory of drift instability, the diffusion coefficient is estimated as $D \sim D_B(\gamma_L/\omega_d) \ll D_B$, where $D_B = cT_e/eB_0$ is the Bohm diffusion coefficient and γ_L is the growth rate of the linear instability. From dimensionality considerations, it follows that the turbulent diffusion coefficient has the form [16]

$$D_\perp \sim \tau^{-1}\lambda_\perp^2, \tag{83}$$

where τ is the decorrelation time, which is equal in order of magnitude to $\tau \sim 1/\gamma_{mod}$, and $\lambda_\perp$ is the characteristic spatial scale of turbulent pulsations across the magnetic field. It is natural to estimate $\lambda_\perp$ as $\lambda_\perp \sim k_\perp^{-1}$. For γ_{mod} and $k_\perp$ given by expressions (39) and (38), respectively, the diffusion coefficient is estimated as

$$D_\perp \sim \frac{1}{1+\mu}\frac{\omega_0}{\omega_{Bi}}\frac{f(\xi)}{\xi}D_B. \tag{84}$$

For the maximum growth rate (41), the diffusion coefficient is approximately equal to $D_\perp \sim D_B\omega_0/\omega_{Bi}$, which is below the Bohm value. In the long-wavelength part of the spectrum, the diffusion coefficient increases with wavelength and, for

$$\rho_s^2 k_\perp^2 < \left(\frac{\omega_d}{\omega_{Bi}}\right)^{1/2}\left(\frac{\omega_0}{\omega_{Bi}}\right)^{3/2}\frac{e}{T_e}\left|\psi_0^0\right|, \tag{85}$$

becomes larger than the Bohm value. Consequently, under the condition $\omega_d/\omega_0 \ll \omega_0/\omega_{Bi}$, the diffusion coefficient can be on the order of the Bohm coefficient.

Assuming that there is a steady-state uniform energy flux in k space,

$$\gamma k^2 \varepsilon(\omega, \mathbf{k})|\psi|^2 = \text{const},$$

we can estimate the density perturbation amplitude $\bar{\eta}$ in a long-wavelength drift wave. In this case, the dielectric function has the form

$$\varepsilon(\omega, \mathbf{k}) \approx 1 + \frac{\omega_{Li}^2}{\omega_{Bi}^2} - \frac{[\mathbf{k}_\perp \times \nabla\omega_{Li}^2]_z}{k^2\omega\omega_{Bi}}. \tag{86}$$

Under resonance condition (33) and for the maximum growth rate (41), the estimate is

$$\bar{\eta}^2 \sim \mu\frac{\gamma_L}{\omega_d}. \tag{87}$$

In our study, we have considered a highly nonisothermal plasma with $T_i \ll T_e$. In this approximation, the gas-kinetic ion pressure $\langle n_{(2)}\rangle T_i$, which may have a stabilizing effect in the course of the modulational instability, has been neglected. In addition, in actual devices, the magnetic field and the field of the plasma velocities are both sheared. It is well known that the shear of the plasma velocity parallel to the magnetic field provides a new mechanism for the onset of drift instability. We can therefore expect that this shear will produce additional effects during the development of nonlinear processes such as the modulational instability.

We have also neglected collisions in the plasma, assuming that the collision frequency is much lower than the frequencies of all the processes under consideration. This neglect imposes an upper limit on the plasma density. Setting the effective collision frequency equal to $\nu_{eff} \approx 1.6 \times 10^{-5} n T_e^{-3/2}$ (where T_e is expressed in electronvolts and the plasma density is in particles per cubic centimeter), we obtain an upper estimate for the plasma density, $n < 10^9 T_e^{3/2}$, at which collisions can be ignored. In the opposite case, it is necessary to take into account electron collisions. Also, in an isothermal plasma ($T_i \sim T_e$), an important role is played by ion–ion collisions, which give rise to an aperiodic convective mode that is slowly damped by ion viscosity, $\mu_i = 0.3T_i\nu_i/(m_i\omega_{Bi}^2)$. The nonlinear energy transfer to these modes can reverse the sign of the damping rate, thereby resulting in the excitation of a convective mode.

The effect considered in this paper, namely, the modulational interaction between drift waves, can have a strong impact on the generation of streamers and zonal flows in a tokamak wall plasma. This has been illustrated above by one-dimensional solutions to the evolutionary equations and is to be studied in more detail in a subsequent paper.

ACKNOWLEDGMENTS

We are grateful to A.A. Rukhadze for discussing the results obtained.

REFERENCES

1. L. M. Gorbunov, Usp. Fiz. Nauk **109**, 631 (1973) [Sov. Phys. Usp. **16**, 217 (1973)].
2. A. F. Aleksandrov, A. A. Kuzovnikov, N. Nikolov, and A. A. Rukhadze, Nucl. Fusion **9**, 137 (1969).
3. G. J. Morales and Y. C. Lee, Phys. Rev. Lett. **35**, 930 (1975).
4. S. Benkadda, S. I. Popel, V. N. Tsytovich, *et al.*, Phys. Plasmas **3**, 571 (1996).
5. S. I. Popel, S. V. Vladimirov, and V. N. Tsytovich, Phys. Rep. C **259**, 327 (1995).
6. S. V. Vladimirov, V. N. Tsytovich, S. I. Popel, and F. Kh. Khakimov, *Modulational Interactions in Plasmas* (Kluwer, Dordrecht, 1995), p. 544.
7. A. F. Alexandrov, L. S. Bogdankevich, and A. A. Rukhadze, *Principles of Plasma Electrodynamics*

(Vysshaya Shkola, Moscow, 1978; Springer-Verlag, Berlin, 1984).

8. L. I. Rudakov and V. N. Tsytovich, Pis'ma Zh. Éksp. Teor. Fiz. **25**, 520 (1977) [JETP Lett. **25**, 489 (1977)].
9. L. I. Rudakov and V. N. Tsytovich, Zh. Éksp. Teor. Fiz. **75**, 1618 (1978) [Sov. Phys. JETP **48**, 816 (1978)].
10. A. V. Gaponov and M. A. Miller, Zh. Éksp. Teor. Fiz. **34**, 242 (1958) [Sov. Phys. JETP **7**, 168 (1958)].
11. A. A. Veryaev and V. N. Tsytovich, Kratk. Soobshch. Fiz., No. 5, 15 (1979).
12. S. I. Popel, I. E. Rumanov, and V. N. Tsytovich, Contrib. Plasma Phys. **34**, 5 (1994).
13. S. I. Popel and M. Y. Yu, Phys. Rev. E **50**, 3060 (1994).
14. A. Galeev and R. Sagdeev, in *Review of Plasma Physics*, Ed. by M. A. Leontovich (Atomizdat, Moscow, 1973), Vol. 7.
15. V. N. Tsytovich, *Lectures on Nonlinear Plasma Kinetics* (Springer-Verlag, Berlin, 1995), p. 376.
16. S. S. Moiseev and R. Z. Sagdeev, Zh. Éksp. Teor. Fiz. **44**, 763 (1963) [Sov. Phys. JETP **17**, 515 (1963)].

Translated by O.E. Khadin

Plasma Physics Reports, Vol. 29, No. 9, 2003, pp. 779–784. Translated from Fizika Plazmy, Vol. 29, No. 9, 2003, pp. 841–846.

PLASMA INSTABILITY

Drift Stabilization of Internal Resistive-Wall Modes in Tokamaks

S. V. Konovalov*, **, A. B. Mikhailovskii, ***, V. S. Tsypin****, R. M. O. Galvão****, and I. C. Nascimento******

**Naka Fusion Research Establishment, Japan Atomic Energy Research Institute, Ibaraki 3111–0193, Japan*

***Nuclear Fusion Institute, Russian Research Centre Kurchatov Institute, pl. Kurchatova 1, Moscow, 123182 Russia*

****Nonlinear Physics Laboratory, Moscow Institute for Physics and Technology, Institutskiĭ per. 9, Dolgoprudnyĭ, Moscow oblast, 141700 Russia*

*****Institute of Physics, University of São Paulo, Rua do Matão, Travessa R, 187, 05508–900 São Paulo, Brazil*

Received January 9, 2003; in final form, February 27, 2003

Abstract—The problem of drift stabilization of the internal resistive-wall modes (RWMs) in tokamaks is theoretically investigated. The basic assumption of the model is that, when the drift effects are neglected, these modes are unstable in the absence of a conducting wall and stable in the presence of a close-fitting perfectly conducting wall. In the former case, the instability condition is expressed as $\Delta'_\infty > 0$, where Δ'_∞ is the matching parameter calculated under the assumption that the wall is removed to infinity. In the latter case, one has $\Delta'_W < 0$, where Δ'_W is the external matching parameter of tearing modes calculated assuming a perfectly conducting wall at the plasma boundary. In the case with a resistive wall, the relevant parameter can be either Δ'_∞ or Δ'_W, depending on whether the value of the dimensionless parameter $\omega\tau_s/2m$ is small or large, respectively (here ω is the mode frequency, τ_s is the resistive time constant of the wall, and m is the poloidal mode number). In the presence of drift effects, the mode frequency ω is approximately equal to the electron drift frequency, $\omega \approx \omega_{*e}$. The value of the parameter $\omega_{*e}\tau_s/2m$, which therefore determines the behavior of internal RWMs, is estimated for several existing tokamaks, namely, AUG (ASDEX-Upgrade), DIII-D, JET, TFTR, and JT-60U, as well as for the projected ITER-FEAT. It is shown that, although drift effects do not stabilize internal RWMs in current devices, they should be efficient in suppressing these modes in reactor-grade tokamaks. © *2003 MAIK "Nauka/Interperiodica".*

1. INTRODUCTION

Resistive-wall modes (RWMs) are suggested as one of the possible reasons for the limitation of the maximum plasma pressure in fusion reactors of the tokamak type [1]. In the cylindrical approximation, RWMs are divided into external and internal ones, depending on whether their singular point lies outside or inside the plasma column, respectively.

In the simplest formulation of the problem, external RWMs have been studied in [2], where it was shown that, neglecting toroidicity, they do not lead to a limitation of the plasma pressure. However, according to numerical simulations [3], such a limitation arises in toroidal geometry. The mechanism of the toroidicity effect on external RWMs was discussed in [4, 5] (see also [6], chapter 27). This mechanism is related mainly to the appearance of side-band toroidicity-induced poloidal harmonics with singular points lying inside the plasma. The numerical simulation of [3] was used in [7] to explain experimental results obtained in the DIII-D tokamak. (Later DIII-D experiments relevant to the topic under consideration were overviewed in [8].)

Internal RWMs were first studied in [9]. Similar to external RWMs, they do not lead to a limitation of the plasma pressure when toroidicity is neglected. It was suggested in [9] that allowance for their toroidal coupling with side-band harmonics could yield such a limitation; however, to the best of our knowledge, this coupling has not yet been investigated.

In general, internal RWMs are conventional tearing modes [10] modified by the wall resistivity. In order to influence tearing modes, the perturbed field caused by the resistive wall currents should penetrate into the plasma resistive layer of these modes. The strength of the penetrating mechanism depends on the mode frequency [11]. In the case of a rotating plasma column, the tearing mode frequency is defined by the plasma rotation frequency [9]. In addition, according to Coppi [12] (see also [6], section 22.6), the mode frequency also depends on the diamagnetic drift effects. Internal RWMs in the presence of these effects were investigated by Finn [13].

The analysis carried out in [13] concerns the case where the perpendicular viscosity overcomes the per-

1063-780X/03/2909-0779$24.00 © 2003 MAIK "Nauka/Interperiodica"

pendicular inertia—a physical situation that is important in the presence of anomalous perpendicular viscosity. In this context, it is worth mentioning that the effect of anomalous perpendicular viscosity has recently been incorporated into the analysis of neoclassical tearing modes [14, 15]. One of the major goals of this work is to analyze the opposite case, namely, when inertia overcomes viscosity, which is relevant for high-temperature regimes in the absence of anomalous viscosity.

A further improvement of our analysis is to take into account the effect of nonzero ion temperature, extending the model of [13], in which the ion temperature was assumed to be vanishingly small in comparison with the electron one.

Another goal of our work is to extend the general discussion of the influence of drift diamagnetic effects on RWMs to the investigation of the relevance of these effects for the conditions of existing and future reactor-grade tokamaks.

External RWMs were the first ones to be used to interpret DIII-D experimental data [7]. The results of computer simulations of these modes (see [3]) were employed to explain both the beta limitation observed in [7] and the weakening of this limitation with increasing plasma rotation. Another important point is that the sensitivity of external RWMs to plasma rotation was predicted in [3] based on the introduction of an artificial Landau damping. It was assumed in [3] that the physical mechanism for such a damping is the resonant interaction between waves and particles. However, as was explained in [16, 17] (see also [6], chapter 28), this interaction can play a role only when toroidal effects are neglected. In the presence of toroidicity, most of the resonant particles become trapped, which leads to a negligibly weak effect of Landau damping. The results obtained in [16, 17] were confirmed in [18, 19].

On the whole, the recent theory of external RWMs is unable to predict the stabilizing effect of plasma rotation on these modes. In contrast, the main essence of the recent theory of internal RWMs is its ability to predict that such modes can be stabilized by plasma rotation. Actually, allowance for plasma rotation is a common element of many works addressed to internal RWMs, including [9, 13]. The procedure of including this effect is formally rather simple: the mode frequency in the expression for the internal matching parameter calculated neglecting the plasma rotation is substituted by the Doppler-shifted mode frequency, where the shift is due to plasma rotation. Although the study of the effect of plasma rotation on internal RWMs is not the main goal of our paper, we have included such a rotation in our exposition in order to relate our approach to the traditional one.

The starting equations that are necessary for our analysis, together with some preliminary comments, are presented in Section 2, and the analysis is carried out in Section 3. Estimations of the role of drift diamagnetic effects on internal RWMs (for both recent and projected tokamak experiments) are the subject of Section 4. Section 5 is devoted to a discussion of the results obtained.

2. STARTING EQUATIONS AND PRELIMINARY COMMENTS

2.1. Tearing Modes for a Perfectly Conducting Wall

The dispersion relation for the tearing modes, neglecting the wall resistivity, is given by [10]

$$\Delta^{\text{int}} = \Delta'_W, \tag{2.1}$$

where Δ'_W is the external matching parameter (i.e., the logarithmic jump in the radial component of the perturbed magnetic field) calculated from the solution of the ideal MHD equations in the presence of a perfectly conducting wall (the subscript W stands for the wall) and Δ^{int} is the corresponding matching parameter for the resistive layer around the singular point (the internal matching parameter), which in the absence of drift effects is given by (see [10] for details)

$$\Delta^{\text{int}} = k_y \hat{\gamma}^{5/4} \gamma_R^{-3/4} \omega_A^{-1/2} I. \tag{2.2}$$

Here, $k_y = m/r_s$, $m = 2, 3, \ldots$ is the poloidal mode number; r_s is the radius of the singular magnetic surface; $\hat{\gamma} = -i\omega$ (the time dependence of the perturbations is taken in the form $\exp(-i\omega t)$), $\gamma_R = k_y^2 c^2/(4\pi\sigma)$ is the plasma resistive decay rate; σ is the plasma electric conductivity; c is the speed of light; $\omega_A = v_A/L_s$ is the characteristic Alfvén frequency; v_A is the Alfvén velocity; L_s is the shear length; and $I = 4\pi\Gamma(3/4)/\Gamma(1/4)$ is a numerical factor, where Γ is the gamma function.

We note that, to a great extent, the value of Δ'_W depends mainly on the shape of the current profile [14]. For

$$\Delta'_W > 0 \tag{2.3}$$

it follows from Eqs. (2.1) and (2.2) that the tearing mode becomes absolutely unstable ($\mathrm{Re}\,\omega = 0$) with the growth rate

$$\mathrm{Im}\,\omega \equiv \gamma = \gamma_t, \tag{2.4}$$

where

$$\gamma_t \approx (\Delta'_W/k_y)^{4/5} \gamma_R^{3/5} \omega_A^{2/5} \tag{2.5}$$

is the classical growth rate of tearing modes [10].

2.2. Resistive-Wall Tearing Modes

According to [11], in the presence of a thin resistive wall placed at the plasma boundary, the external matching parameter Δ'_W is substituted by

$$\Delta'_W \longrightarrow \Delta'(\omega), \tag{2.6}$$

where

$$\Delta'(\omega) = \Delta'_\infty - \frac{\Delta'_\infty - \Delta'_W}{1 + 2im/(\omega\tau_s)}. \quad (2.7)$$

Here, Δ'_∞ is the external matching parameter in the absence of a wall (i.e., when the wall is removed to $r \longrightarrow \infty$),

$$\tau_s = 4\pi r_W d/\eta_W c^2 \quad (2.8)$$

is the resistive time constant, d is the wall thickness, r_W is the radial coordinate, and η_W is the resistivity of the wall.

If one substitutes Eqs. (2.6) and (2.7) into Eq. (2.1) (i.e., includes the resistive wall effects), the tearing mode becomes more unstable, so that it can be excited even for

$$\Delta'_W < 0. \quad (2.9)$$

Thus, if one takes

$$\omega\tau_s/2m \longrightarrow 0, \quad (2.10)$$

$$\Delta'_\infty > 0, \quad (2.11)$$

one finds, instead of Eqs. (2.4) and (2.5), $\mathrm{Re}\,\omega = 0$ and

$$\gamma = \gamma_{RWt}, \quad (2.12)$$

where γ_{RWt} is the growth rate of resistive-wall tearing modes given by [cf. (2.5)]

$$\gamma_{RWt} \approx (\Delta'_\infty/k_y)^{4/5}\gamma_R^{3/5}\omega_A^{2/5}. \quad (2.13)$$

Revealing the instability under conditions (2.9) and (2.11) is the key idea of the theory of internal RWMs [9, 13].

2.3. Allowance for Diamagnetic Drift Effects

With allowance for drift effects, expression (2.2) for the internal matching parameter is modified by the substitution [12]

$$\hat\gamma^5 \longrightarrow \hat\gamma^5 Q_e^3 Q_i, \quad (2.14)$$

where

$$Q_e = 1 - \omega_{*e}/\omega, \quad (2.15)$$

$$Q_i = 1 - \omega_{p*i}/\omega. \quad (2.16)$$

Here, ω_{*e} is the electron drift diamagnetic frequency defined by the density gradient and ω_{p*i} is the ion drift diamagnetic frequency defined by the pressure gradient. These values are given by

$$\omega_{*e} = cT_e m/eBr_s L_n, \quad (2.17)$$

$$\omega_{p*i} = -cT_i m/eBr_s L_{pi}. \quad (2.18)$$

Here, T_e and T_i are the electron and ion temperatures, B is the magnetic field, $L_n = (-N'/N)^{-1}$ is the density gradient scale length, N is the plasma density, $L_{pi} = (-p_i'/p_i)^{-1}$ is the ion pressure gradient scale length, p_i is the ion pressure, the prime stands for the radial derivative, and e is the ion charge.

As a result, one arrives at the following dispersion relation for the drift–tearing modes modified by the resistive-wall effects:

$$k_y\hat\gamma^{5/4}(Q_e^3 Q_i)^{1/4}\gamma_R^{-3/4}\omega_A^{-1/2} I = \Delta'(\omega), \quad (2.19)$$

where $\Delta'(\omega)$ is given by Eq. (2.7).

Let us now compare dispersion relation (2.19) with the dispersion relation given by Eq. (9) in [13]. Both the left- and the right-hand sides of our dispersion relation are standard: they correspond to the related expressions given in [12] and [11], respectively. The right-hand side of Eq. (9) in [13] is the same as that in Eq. (2.19), while the left-hand side, in dimensionless form, is $[\hat\gamma(\hat\gamma + i\omega_{*e})^5]^{1/6}$, which differs from [12]. This difference is due to the assumption made in [13] that, in the singular layer, viscosity is more important than inertia, while, according to the above explanations, our analysis concerns the alternative situation, when the viscosity is negligible compared with the inertia.

2.4. Allowance for Cross-Field Plasma Rotation

If there is a radial equilibrium electric field E_{r0} at the resonant point $r = r_s$, then the mode frequency on the left-hand side of Eq. (2.19) should be substituted as

$$\omega \longrightarrow \omega - \Omega, \quad (2.20)$$

where, as was already discussed in Section 1, Ω is the Doppler shift of the mode frequency. The frequency shift Ω is given by

$$\Omega = mV_0/r_s, \quad (2.21)$$

where $V_0 = -cE_{r0}/B$ is the cross-field velocity. Then, instead of Eq. (2.19), one has

$$k_y(\hat\gamma + i\Omega)^{5/4}\left(1 - \frac{\omega_{*e}}{\omega - \Omega}\right)^{3/4}\left(1 - \frac{\omega_{p*i}}{\omega - \Omega}\right)^{1/4} \times \gamma_R^{-3/4}\omega_A^{-1/2} I = \Delta'(\omega). \quad (2.22)$$

This dispersion relation describes the effect of plasma rotation on resistive-wall drift–tearing modes.

Note also that, when the ion diamagnetic drift effects are neglected, the frequency shift Ω is represented as

$$\Omega = -nV_\phi/R, \quad (2.23)$$

where V_ϕ is the toroidal plasma velocity, R is the torus major radius, and n is the toroidal mode number. It was assumed in deriving Eq. (2.23) that the poloidal plasma rotation vanishes due to the neoclassical viscosity, so

that the toroidal plasma velocity becomes determined by the cross-field velocity.

3. DRIFT–TEARING MODES IN THE PRESENCE OF THE WALL-RESISTIVITY EFFECT

3.1. Case of Vanishing Cross-Field Plasma Rotation

In recent tokamaks, operating at a rather high plasma temperature, the corresponding low value of the plasma resistivity makes growth rate (2.5) quite small, while the characteristic drift frequency becomes large. For this reason, the theory relevant to recent devices should be based on the condition

$$\gamma_t \ll (\omega_{*e}, \omega_{p*i}). \tag{3.1}$$

Within this approximation and in the case of a perfectly conducting wall, one finds, instead of Eq. (2.5), (cf., e.g., Eq. (22.29) in [6]),

$$\mathrm{Re}\,\omega \approx \omega_{*e}, \tag{3.2}$$

$$\mathrm{Im}\,\omega \equiv \gamma = c_*\left(\frac{\Delta'_W}{k_y}\right)^{4/3}, \tag{3.3}$$

where

$$c_* = \frac{1}{2I^{4/3}}\gamma_R\left(1 + \frac{T_i L_{pi}}{T_e L_n}\right)^{-1/3}\left(\frac{\omega_A}{\omega_{*e}}\right)^{2/3}. \tag{3.4}$$

We emphasize that, formally, if condition (3.1) is satisfied, then at $\Delta'(\omega) = \Delta'_W$, Eq. (2.19) has roots with $\omega \ll \omega_{*e}$. However, these roots should be rejected because they do not satisfy the rule of root selection (physically, these roots correspond to eigenfunctions divergent in the singular layer).

With allowance for the wall resistivity, instead of expression (3.3), one has

$$\gamma = c_*\,\mathrm{Re}\left\{\exp\left(-i\frac{\pi}{3}\right)\left[\frac{\Delta'(\omega_{*e})}{k_y}\right]^{4/3}\right\}. \tag{3.5}$$

According to Eqs. (2.6) and (2.7), it follows from expression (3.5) that the resistive-wall effects can be important only if [cf. (2.10)]

$$\omega_{*e}\tau_s/2m \le 1. \tag{3.6}$$

In the limiting case $\omega_{*e}\tau_s/2m \ll 1$, expression (3.5) reduces to

$$\gamma = c_*\left(\frac{\Delta'_\infty}{k_y}\right)^{4/3}. \tag{3.7}$$

In the opposite case, i.e., for

$$\omega_{*e}\tau_s/2m \gg 1, \tag{3.8}$$

the effect of the wall resistivity on the modes considered here is insignificant and one arrives at expression (3.3). (We emphasize that this statement does not concern nonlinear modes, such as magnetic islands, where the situation can be more complicated.)

Thus, the electron diamagnetic drift effect stabilizes resistive-wall tearing modes, which agrees with the conclusion of [13] when viscosity overcomes inertia. As can be inferred from Eq. (3.4), the ion diamagnetic drift effect results in an insignificant decrease in the growth rate of these modes.

3.2. Effect of Cross-Field Plasma Rotation on Resistive-Wall Drift–Tearing Modes

Let us assume that there is a sufficiently strong cross-field plasma rotation, so that, in addition to inequality (3.1), one has

$$\gamma_t \ll \Omega, \tag{3.9}$$

where Ω is given by Eq. (2.21). Then, instead of Eq. (3.2), the real part of the mode frequency is given by

$$\mathrm{Re}\,\omega \approx \omega_{*e} + \Omega. \tag{3.10}$$

As for the growth rate, it is given by Eq. (3.3) at [cf. (3.8)]

$$(\omega_{*e} + \Omega)\tau_s/2m \gg 1, \tag{3.11}$$

or by Eq. (3.7) at [cf. (3.6)]

$$(\omega_{*e} + \Omega)\tau_s/2m \ll 1. \tag{3.12}$$

Thus, the cross-field plasma rotation reinforces the stabilizing effect of the electron diamagnetic drift at $\Omega/\omega_{*e} > 0$ and weakens it at $\Omega/\omega_{*e} < 0$.

4. ESTIMATES FOR CURRENT AND PROJECTED TOKAMAKS

Let us analyze whether condition (3.6) is satisfied under the conditions of the current devices and estimate whether it will be relevant under the conditions of projected fusion reactors. Taking into account expression (2.17) for the electron drift diamagnetic frequency, we can rewrite condition (3.6) in the form

$$\frac{\omega_{*e}\tau_s}{2m} = 0.5\frac{\tau_s\ [\mathrm{ms}]\ T_e\ [\mathrm{keV}]}{B\ [\mathrm{T}]}\frac{1}{(r_s L_n)\ [\mathrm{m}^2]} \le 1. \tag{4.1}$$

One can see that, since ω_{*e} is proportional to m ($\omega_{*e} \sim m$), the poloidal mode number m drops out of condition (4.1). Nonetheless, condition (4.1) actually depends implicitly on the value of m for two reasons. First, the resistive time constant of the wall τ_s, in contrast to approximate expression (2.8), does depend on the poloidal harmonic number m. Second, the position of the singular magnetic surface $q(r_s) = m/n$ also depends on m, so that the local values of $T_e(r_s)$ and $r_s L_n(r_s)$ enter-

Estimates of the parameter $\omega_{*e}\tau_s/2m$ for several tokamaks

	AUG	DIII–D	JET	TFTR	JT-60U	ITER-FEAT
B, T	2.2	2.5	3.5	≤5.0	≤4.5	5.3
a, m	0.5	0.6	1.0	0.9	0.9	2.0
T_e, keV	0.5	1.0	1.0	1.0	2.0	≥3.0
$\omega_{*e}/2m$, ms^{-1}	0.46	0.56	0.16	≥0.12	≥0.27	≥0.07
τ_s, ms	7.0	5.0	2.5	5.0	10.0	150.0
$\omega_{*e}\tau_s/2m$	3.2	2.8	0.4	≥0.6	≥2.7	≥10.6

ing condition (4.1) vary with varying poloidal mode number.

To estimate the influence of the profiles of the equilibrium plasma parameters on the value of $r_sL_n(r_s)$, we assume that the singular surfaces r_s/a for the most unstable modes with low poloidal mode numbers $m = 2$ and 3 lie within the interval $0.5 < r_s/a < 0.75$, where a is the minor plasma radius. For simplicity, we consider the plasma density profile in the form

$$N(r) = N_0[1 - (r/a)^{\alpha}] \tag{4.2}$$

with $2 \le \alpha \le 4$. We then find that the values of r_sL_n lie in the range $0.25 \le r_sL_n/a^2 \le 0.94$. In the following estimates, we use the approximation

$$r_sL_n = a^2, \tag{4.3}$$

keeping in mind that, for flat density profiles, it gives an underestimated value of the electron drift frequency ω_{*e}.

In the table, we present the list of parameters entering condition (4.1), as well as the estimated values of $\omega_{*e}\tau_s/2m$ for several tokamaks contributing to the ITER database [1]. The data from the current tokamaks AUG (ASDEX-Upgrade), DIII-D, JET (Joint European Torus), TFTR (Tokamak Fusion Test Reactor), JT–60U, as well as those foreseen for the projected ITER-FEAT have been compiled.

It should be noted that, when collecting the parameters B, a, T_e, and τ_s in this table, it is difficult to find the full data set corresponding to a unique discharge in any of the listed devices. Besides, most of the available experimental data of concern do not contain all the necessary information for accurately estimating the value of ω_{*e}. An uncertainty factor of 2 is also imbedded in the listed values of the wall resistive time constant τ_s.

Therefore, the calculated values of the parameter $\omega_{*e}\tau_s/2m$ for existing devices presented in the table are rather rough. Nevertheless, from this table one can see that the wall resistivity can destabilize the drift–tearing modes in the present-day tokamaks, whereas ITER-FEAT has a "surplus" in the value of $\omega_{*e}\tau_s/2m$ that is sufficient to practically exclude the destabilizing effect of the wall resistivity. This surplus originates mostly from the extremely large wall resistive time constant τ_s in ITER due to the large thickness of its resistive wall.

5. DISCUSSION

We have shown that the resistive-wall effects play an important role in the stabilization of drift–tearing modes when condition (3.6) is satisfied. If condition (2.11) is also satisfied, then they lead to a growth of these modes with the growth rate given by Eq. (3.7) and to their rotation with the electron diamagnetic drift frequency ω_{*e} [see Eq. (3.2)]. The cross-field plasma rotation influences the penetration of the resistive-wall effects (reinforcing or weakening it, depending on the sign of the ratio Ω/ω_{*e}) and also the rotation frequency of the modes.

According to the table, the current experiments are performed under conditions where the inverse resistive time constant of the wall, $1/\tau_s$, is, roughly speaking, of the same order as $\omega_{*e}/2m$. This means that the above mechanism for the growth of drift–tearing modes is possible in the existing devices.

Unfortunately, there are practically no experimental papers related to the investigation of RWMs where the value of the electron drift frequency has been reported. Evidently, such information is necessary for the reliable interpretation of the experimental data. Moreover, it seems that special experimental studies elucidating the dependence of the observed modes on drift effects should be performed. Finding this dependence is important in order to determine whether the internal RWMs are actually relevant to the current devices. At the same time, according to the estimates presented in the table, the growth of the drift–tearing modes in the ITER-FEAT seems to be rather impossible. Therefore, it is not excluded that the general situation with MHD activity in reactor-grade tokamaks will be more favorable than that in the existing devices.

ACKNOWLEDGMENTS

We are grateful to the anonymous referee for valuable comments. This work was supported by the Russian Foundation for Basic Research (project no. 03-02-16294), the Russian Federal Program "Support of Lead-

ing Scientific Schools" (grant no. 2024.2003.2), the Department of Atomic Science and Technology of the Ministry of Atomic Industry of the Russian Federation, the U.S. Civilian Research and Development Foundation for the Independent States of the Former Soviet Union (CRDF) (grant no. BRHE REC–011), the Foundation for the Support of Research of the State of São Paulo (FAPESP), the National Council for Scientific and Technological Development (CNPq), the University of São Paulo, and the National Program of Support for Excellence Groups (PRONEX) of the Ministry of Science and Technology of the Federal Republic of Brazil (grant no. RMOG 050/70).

REFERENCES

1. ITER Physics Expert Group on Disruptions, Plasma Control, and MHD and ITER Physics Basis Editors, Nucl. Fusion **39**, 2251 (1999).
2. L. E. Zakharov and S. V. Putvinskiĭ, Fiz. Plazmy **13**, 118 (1987) [Sov. J. Plasma Phys. **13**, 68 (1987)].
3. A. Bondeson and D. J. Ward, Phys. Rev. Lett. **72**, 2709 (1994).
4. A. B. Mikhailovskii and B. N. Kuvshinov, Fiz. Plazmy **21**, 835 (1995) [Plasma Phys. Rep. **21**, 789 (1995)].
5. B. N. Kuvshinov and A. B. Mikhailovskii, Fiz. Plazmy **22**, 490 (1996) [Plasma Phys. Rep. **22**, 446 (1996)].
6. A. B. Mikhailovskii, *Instabilities in a Confined Plasma* (Institute of Physics, Bristol, 1998).
7. A. D. Turnbull, T. S. Tailor, E. J. Straight, *et al.*, Plasma Phys. Controlled Nucl. Fusion Res. **1**, 705 (1995).
8. V. D. Pustovitov, Fiz. Plazmy **29** (in press).
9. J. M. Finn, Phys. Plasmas **2**, 198 (1995).
10. H. P. Furth, J. Killeen, and M. N. Rosenbluth, Phys. Fluids **6**, 459 (1963).
11. P. H. Rutherford, in *Proceedings of the Course and Workshop on Basic Physical Processes of Toroidal Fusion Plasmas, Varenna, 1985*, Vol. 2, p. 531.
12. B. Coppi, Phys. Fluids **8**, 2273 (1965).
13. J. M. Finn, Phys. Plasmas **5**, 3595 (1998).
14. S. V. Konovalov, A. B. Mikhailovskii, M. S. Shirokov, and V. S. Tsypin, Plasma Phys. Controlled Fusion **44**, 51 (2002).
15. S. V. Konovalov, A. B. Mikhailovskii, M. S. Shirokov, and V. S. Tsypin, Phys. Plasmas **9**, 4596 (2002).
16. A. B. Mikhailovskii and B. N. Kuvshinov, Fiz. Plazmy **21**, 849 (1995) [Plasma Phys. Rep. **21**, 802 (1995)].
17. A. B. Mikhailovskii and B. N. Kuvshinov, Phys. Lett. A **209**, 83 (1995).
18. A. Bondeson and M. S. Chu, Phys. Plasmas **3**, 3013 (1996).
19. B. N. Kuvshinov and A. B. Mikhailovskii, Fiz. Plazmy **24**, 675 (1998) [Plasma Phys. Rep. **24**, 623 (1998)].

Translated by the authors

Plasma Physics Reports, Vol. 29, No. 9, 2003, pp. 785–788. Translated from Fizika Plazmy, Vol. 29, No. 9, 2003, pp. 847–850.

PLASMA KINETICS

Nonlocal Equation for the Symmetric Part of the Electron Distribution Function in an Inhomogeneous Plasma

O. G. Bakunin

Russian Research Centre Kurchatov Institute, pl. Kurchatova 1, Moscow, Russia

Received July 22, 2002; in final form, January 27, 2003

Abstract—A nonlocal kinetic equation is derived for the symmetric part of the distribution function of suprathermal electrons. It is shown that Albritton equations are merely local approximations to the total kinetic equation. Even in the simplest situation, the local approximations of the nonlocal effects are impossible to construct because of the interdependence of the variables. A self-similar solution to the equations under study is proposed. © *2003 MAIK "Nauka/Interperiodica".*

1. INTRODUCTION

An important but still unresolved problem in the kinetic theory of plasma is that of a theoretical description of the transport of particles whose mean free path λ is comparable with the spatial scale L on which the plasma parameters vary. Under these conditions, transport is nonlocal because the formation of particle fluxes in a certain region is influenced by the regions that are as far away as several mean free paths. That such problems are nontrivial was recognized long ago [1]; tackling them is of vital importance for the physics of space plasma, laser plasma, and wall plasma in tokamaks [2–9].

Here, a kinetic description will be developed for suprathermal electrons in a highly ionized inhomogeneous plasma. This problem is highly relevant because of the need to generalize the Spitzer–Härm classical theory [10–12]. The description will be formulated on the basis of the time-independent kinetic equation with a Fokker–Planck collision integral:

$$\mu v\frac{\partial f}{\partial x} - \frac{eE}{m}\left(\mu\frac{\partial f}{\partial v} + \frac{1-\mu^2}{v}\frac{\partial f}{\partial \mu}\right) = \frac{1}{v^2}\frac{\partial}{\partial v}\left[v^2\nu_e(v)\left(vf + \frac{T_e(x)}{m}\frac{\partial f}{\partial v}\right)\right] + \beta\nu_e(v)\frac{\partial}{\partial\mu}\left[(1-\mu^2)\frac{\partial f}{\partial\mu}\right], \quad (1)$$

$$\beta = (1+Z_{\text{eff}})/2, \quad Z_{\text{eff}} = \frac{1}{n_e}\sum Z_i^2 n_i,$$

$$\nu_e(v) = \frac{4\pi e^4\Lambda n_e(x)}{m^2 v^3}, \quad \mu = \cos\theta.$$

A series of papers by Gurevich [2, 13, 14] made this formulation of the problem for runaway electrons generally accepted. It is worth noting that the problem of nonlocal particle transport is also of interest from the standpoint of general physics. Kramers [15] was one of the first to point out that the development of a kinetic description of diffusion in an inhomogeneous medium is a nontrivial task. He noted the difficulties encountered in attempting to derive the diffusion equation in conventional coordinate space,

$$\frac{\partial n}{\partial t} = -\frac{\partial}{\partial x}(Un) + D\frac{\partial^2 n}{\partial x^2} \quad (2)$$

from the simplest kinetic equation that takes into account the spatial inhomogeneity of the medium,

$$\frac{\partial f}{\partial t} + v\frac{\partial f}{\partial x} + \frac{F(x)}{m}\frac{\partial f}{\partial v} = \frac{1}{\tau}\frac{\partial}{\partial v}\left(vf + \frac{kT}{m}\frac{\partial f}{\partial v}\right). \quad (3)$$

Even this derivation required a mathematical trick—switching from ordinary averaging to integration along trajectories. At that time, however, such difficulties were not considered to be a convincing reason to introduce heuristic corrections in the kinetic equation. In fact, Kramers pointed to the conditional character of the diffusion equation and its close connection with the behavior of correlation functions.

2. SIMPLE APPROXIMATIONS FOR NONLOCAL EFFECTS

In view of the difficulties arising in this way, a wide scope of simple approximations has been proposed for nonlocal effects. Thus, the heat flux is approximated by the formula [16, 17]

$$q = \frac{1}{2}\int_0^x q_{\text{SH}}\exp\left\{-\left|\int_x^{x'}\frac{dl}{\lambda_T(l)}\right|\right\}\frac{dx'}{\lambda_T(x')}, \quad (4)$$

1063-780X/03/2909-0785$24.00 © 2003 MAIK "Nauka/Interperiodica"

where q_{SH} is the Spitzer–Härm heat flux, $\lambda_T = v_T(x)/\nu_e(v_T)$ is the mean free path of suprathermal electrons, and $v_T = \sqrt{2T(x)/m}$.

An interesting formula for the electron distribution function was suggested by Krasheninnikov [18]:

$$f = \int_0^\varepsilon f_M \exp\left\{-\left(\frac{\varepsilon - \varepsilon'}{T}\right)\right\}\frac{d\varepsilon'}{T}, \quad (5)$$

where f_M is a Maxwellian function.

The kinetic equation is also modified to describe correlation effects associated with the non-Markovian character of the nonlocal transport [19–21]. Thus, Reshetnyak and Shelepin [21] proposed to supplement the kinetic equation with the terms

$$\frac{\partial^2 f}{\partial x^2}, \frac{\partial^3 f}{\partial x^2 \partial t}, \frac{\partial^3 f}{\partial x^3}. \quad (6)$$

In recent years, the kinetic equation is often treated with fractional derivatives of the form [22–24]

$$\frac{\partial^\alpha f}{\partial v^\alpha}, \frac{\partial^\alpha f}{\partial x^\alpha}, \frac{\partial^\alpha f}{\partial t^\alpha}. \quad (7)$$

It is clear that a deeper understanding of the kinetics of nonlocal transport can be derived from analytic solutions to the Fokker–Planck equations. The most simple and effective method was offered by Albritton [25, 26], who considered the following kinetic equation for the distribution function of suprathermal electrons, $f(x, v, \theta)$:

$$\mu v\frac{\partial f}{\partial x} = \frac{1}{v^2}\frac{\partial}{\partial v}\left[v^2\nu_e(v)\left(vf + \frac{T_e(x)}{m}\frac{\partial f}{\partial v}\right)\right] + \beta\nu_e(v)\frac{\partial}{\partial \mu}\left[(1-\mu^2)\frac{\partial f}{\partial \mu}\right]. \quad (8)$$

This equation is written in terms of the collision integral of the form proposed by Gurevich for a kinetic description of the runaway electrons [13, 14]. To simplify the problem, the term with the electric field in Eq. (8) is neglected in comparison with the term describing the effect of the spatial inhomogeneity, and the distribution function is assumed to be close to a spherically symmetric function,

$$f(\mathbf{v}, x) = F_0(v, x) + F_1(v, x)\cos\theta. \quad (9)$$

In this formulation, the problem was reduced to that of solving the kinetic equation for the symmetric part of the distribution function,

$$\frac{\partial^2 F_0}{\partial y^2} + \frac{1}{\varepsilon^3}\frac{\partial}{\partial \varepsilon}\left(F_0 + T_e(y)\frac{\partial F_0}{\partial \varepsilon}\right) = 0, \quad (10)$$

where $\varepsilon = \frac{mv^2}{2}$ and $dy \propto n(x)dx$.

An elegant and simple solution can be obtained through the simplifying replacement of the sought distribution function by a Maxwellian function, $\frac{\partial F_0}{\partial \varepsilon} \longrightarrow \frac{\partial F_M}{\partial \varepsilon}$. We can see from Eq. (10) that, in this case, the contribution of suprathermal electrons is underestimated. However, we can now derive a simple analytic solution for the electron distribution function from the diffusion equation

$$\frac{\partial^2 F_0}{\partial y^2} + \beta\frac{\partial F_0}{\partial \omega} = Q(\omega(\varepsilon), x) = -\frac{T_e(y)}{\varepsilon^3}\frac{\partial^2 F_M}{\partial \varepsilon^2}, \quad (11)$$

where the role of the time is played by the variable $\omega = \varepsilon^4/4$. The solution so obtained has the form

$$F_0(\varepsilon, y) = -\int G(y, y', \varepsilon, \varepsilon')\frac{T_e(y')}{\varepsilon'^3}\frac{\partial^2 F_M(\varepsilon')}{\partial \varepsilon'^2}. \quad (12)$$

Albritton's assumption of the symmetry of the distribution function can be justified by using the solution to the initial equation in terms of the self-similar variables [27]:

$$f(x, v, \mu) = \frac{f(\xi, \mu)}{T^\alpha(x)}, \quad (13)$$

where $\xi = \varepsilon/T(x)$.

The equation that was solved in [27] has the form

$$\gamma\mu\left(\alpha f + \xi\frac{\partial f}{\partial \xi}\right) - \gamma_E\left(\mu\frac{\partial f}{\partial \xi} + \frac{1-\mu^2}{2x}\frac{\partial f}{\partial \mu}\right) = \frac{1}{\xi}\frac{\partial}{\partial \xi}\left(f + \frac{\partial f}{\partial \xi}\right) + \frac{\beta}{2\xi^2}\frac{\partial}{\partial \mu}\left[(1-\mu^2)\frac{\partial f}{\partial \mu}\right], \quad (14)$$

where the following notation was introduced:

$$\gamma = -\frac{T_e^2}{2\pi e^4 \Lambda n_e}\frac{d\ln T_e}{dx} = \text{const}, \quad \gamma_E = \frac{eET_e(x)}{2\pi e^4 \Lambda n_e \gamma}. \quad (15)$$

Note that Aleksandrov *et al.* [28] proposed self-similar variables that are close to those in Eq. (14). From the solution to the self-similar kinetic equation [27], we can see that the distribution function is close to a spherically symmetric function for a plasma with a sufficiently large effective charge,

$$\beta = \frac{1 + Z_{\text{eff}}}{2} > \frac{1}{\gamma^{1/2}}. \quad (16)$$

It should also be noted that the tail of the self-similar distribution function behaves in accordance with a power law:

$$f(v) \propto \frac{1}{V^a}, \quad (17)$$

which indicates a limited range of applicability of the self-similar approach and perhaps of other approximations used in this way.

3. NONLOCAL KINETIC EQUATION

Here, we consider the problem of the kinetics of suprathermal electrons in an inhomogeneous plasma in Albritton's formulation [see Eq. (8)]. We will try to obtain closed equations for the symmetric part of the electron distribution function, but, in contrast to Albritton's approach, none of the terms will be omitted. We introduce the dimensionless variable $\xi = \varepsilon/T(x)$, in terms of which the initial equation for the electron distribution function takes the form

$$\lambda_T \mu\left(\xi\frac{\partial f}{\partial \xi}\right) = 2\frac{\partial}{\partial \xi}\left(f + \frac{\partial f}{\partial \xi}\right) + \frac{\beta}{\xi}\frac{\partial}{\partial \mu}\left[(1-\mu^2)\frac{\partial f}{\partial \mu}\right]. \quad (18)$$

We consider only those electron distribution functions that are almost spherically symmetric. To do this, we represent the electron distribution function as the sum of two components,

$$f(\xi, \mu) = F_0(\xi) + F_1(\xi)\mu. \quad (19)$$

Note that the parameter range in which these assumptions are valid is known from the self-similar solutions obtained in [27] by Gurevich and Lebedev's technique. The orthogonalization procedure yields the following set of two equations:

$$\frac{\lambda_T}{3}\xi\frac{\partial F_1}{\partial x} = \frac{\partial F_0}{\partial \xi} + \frac{\partial^2 F_0}{\partial \xi^2}, \quad (20)$$

$$\frac{\lambda_T}{3}\xi\frac{\partial F_0}{\partial x} = \frac{2}{3}\frac{\partial F_1}{\partial \xi} + \frac{2}{3}\frac{\partial^2 F_1}{\partial \xi} - F_1\frac{\beta}{\xi}. \quad (21)$$

It is particularly important here to take into account the quasi-symmetry of the electron distribution function. The situation at hand is close to that with the one-dimensional kinetic equation considered by Kramers. In order to achieve the Markovian character of the processes under the conditions of spatial inhomogeneity, he had to introduce additional independent variables. In the situation in question, a similar role is played by the assumptions that the electron scattering is strong and the distribution function of suprathermal electrons is almost spherically symmetric.

The symmetry of Eqs. (20) and (21) enables us to obtain the functional for the symmetric part of the electron distribution function. Using Eq. (21), we write the following equation for the Green's function:

$$\frac{\partial^2 G}{\partial \xi^2} + \frac{\partial G}{\partial \xi} - \frac{3\beta}{2\xi}G = \delta(\xi - \xi'). \quad (22)$$

Now, the asymmetric part of the electron distribution function can be written in the form

$$F_1 = \int_0^\infty \frac{\lambda_T}{2}\xi' G(\xi, \xi')\frac{\partial F_0}{\partial x}d\xi'. \quad (23)$$

The Green's function can be represented in terms of the Whittaker functions in a standard way. Then, the total equation for the symmetric part of the distribution function of suprathermal electrons becomes

$$\frac{\lambda_T}{6}\xi\frac{\partial}{\partial x}\left(\int_0^\infty \lambda_T \xi' G(\xi, \xi')\frac{\partial F_0}{\partial x}d\xi'\right) = \frac{\partial^2 F_0}{\partial \xi^2} + \frac{\partial F_0}{\partial \xi}, \quad (24)$$

where the right-hand side makes it possible to obtain a Maxwellian function on the basis of the competition between friction and diffusion in velocity space.

The results based on Albritton's approach correspond to the following equation without the integral term:

$$-\frac{\lambda_T}{6}\xi\frac{\partial}{\partial x}\left\{\frac{\lambda_T}{\beta}\xi^2\frac{\partial F_0}{\partial x}\right\} = \frac{\partial^2 F_0}{\partial \xi^2} + \frac{\partial F_0}{\partial \xi}. \quad (25)$$

Here, the kernel of the integral operator is considered to be in fact a delta function:

$$G(\xi, \xi') \longrightarrow -\frac{1}{\beta}\delta(\xi - \xi'). \quad (26)$$

From this, we can conclude that, although the solution to the Albritton equation is of integral form, it reflects the nonlocal properties of the particle transport only roughly. It should also be noted that the variables x and v in the integral part of the functional obtained are interdependent because $\xi = \xi(x, v) = mv^2/2T(x)$.

The integral equation derived above can only be solved by making additional simplifying assumptions. However, it has a simple solution in self-similar variables [27, 28]:

$$F_0(x, \xi) = \frac{g_0(\xi)}{T^\alpha(x)}, \quad F_1(x, \xi) = \frac{g_1(\xi)}{T^\alpha(x)}. \quad (27)$$

In these variables, we perform the necessary manipulations to obtain the set of equations

$$\gamma\left(\xi^{1-\alpha}\frac{\partial}{\partial \xi}(\xi^\alpha g_1)\right) = \frac{3}{\xi}\frac{\partial}{\partial \xi}\left(g_0 + \frac{\partial g_0}{\partial \xi}\right), \quad (28)$$

$$g_1 = -\gamma\frac{\xi^2}{\beta}\xi^{1-\alpha}\frac{\partial}{\partial \xi}(\xi^\alpha g_0). \quad (29)$$

In the particular case $\alpha = 2$, we arrive at the sought solution for the symmetric part of the distribution function of suprathermal electrons:

$$g_0(\xi) \propto \exp\left\{-\int_0^\xi d\xi' \frac{3\beta/\gamma^2 + 2\xi'^4}{3\beta/\gamma^2 + \xi'^5}\right\}. \quad (30)$$

Here, a few comments are in order regarding the character of the self-similar variables [27]. In our analysis, the quantity $\gamma = -\frac{T^2}{2\pi e^4 \Lambda n}\frac{d\ln T}{dx}$ serves as the self-similarity parameter. For γ = const, we actually deal with a differential equation. Since the self-similarity of the variables imposes an additional requirement on the density,

$$n(x) \propto T^{\frac{3}{2}-\alpha}, \tag{31}$$

we arrive at the following condition:

$$T^{\alpha-1/2}\frac{dT}{dx} = \text{const}. \tag{32}$$

Resolving this equation yields the model profiles of the plasma parameters:

$$T(x) \propto x^{\frac{1}{\alpha+1/2}}, \quad n(x) \propto x^{-\frac{\alpha-3/2}{\alpha+1/2}}. \tag{33}$$

The most interesting point is that, for $\alpha > 3/2$, the monotonic behavior of $T(x)$ differs from that of $n(x)$ [29–31]. For instance, in the direction chosen in our analysis, the profile $T(x)$ decreases, while the profile $n(x)$ increases. Hence, the problem of fast electrons in a divertor, which is of interest from both a theoretical and an experimental point of view, can be treated in self-similar variables.

4. CONCLUSIONS

(i) A nonlocal kinetic equation for the symmetric part of the distribution function of suprathermal electrons has been derived.

(ii) It has been shown that Albritton equations are merely local approximations of the total kinetic equation.

(iii) It has been established that, even in the simplest situation, it is difficult to obtain local approximations for nonlocal effects because of the interdependence of the variables x and v.

(iv) A self-similar solution to the kinetic equations under study has been proposed.

REFERENCES

1. G. Jaffe, Ann. Phys., Ser. 5 **6**, 55 (1930).
2. A. V. Gurevich and Ya. N. Istomin, Zh. Éksp. Teor. Fiz. **77**, 933 (1979) [Sov. Phys. JETP **50**, 470 (1979)].
3. E. M. Epperlein, Laser Part. Beams **12** (2), 257 (1994).
4. G. Murtazs, M. Mirza, and M. S. Qaisar, Plasma Phys. Controlled Fusion **33**, 215 (1991).
5. G. Murtazs and M. Mirza, Phys. Rev. A **41** (8), 4460 (1990).
6. J. R. Sanmartin, G. Murtazs, and M. Mirza, Phys. Fluids B **4**, 357 (1992).
7. L. M. Montierth, G. Murtazs, and M. Mirza, Phys. Fluids B **1**, 1911 (1989).
8. F. Minotti and C. P. Fontan, Phys. Fluids B **2**, 1725 (1990).
9. Y. Xu and X. T. He, Phys. Rev. E **50** (1), 443 (1994).
10. R. S. Cohen, L. Spitser, and P. M. Routly, Phys. Rev. **80**, 230 (1950).
11. L. Spitser, Astrophys. J. **116**, 299 (1952).
12. L. Spitser and R. Harm, Phys. Rev. **89**, 977 (1953).
13. A. V. Gurevich, Zh. Éksp. Teor. Fiz. **38**, 116 (1960) [Sov. Phys. JETP **11**, 85 (1960)].
14. A. V. Gurevich and Yu. N. Zhivlyuk, Zh. Éksp. Teor. Fiz. **49**, 214 (1965) [Sov. Phys. JETP **22**, 153 (1966)].
15. H. A. Kramers, Physica (Amsterdam) **7**, 84 (1940).
16. J. F. Luciani, P. Mora, and R. Pellat, Phys. Fluids **28**, 835 (1985).
17. J. F. Luciani, P. Mora, and J. Virmont, Phys. Rev. Lett. **51**, 1664 (1983).
18. S. I. Krasheninnikov, Phys. Fluids B **5**, 74 (1993).
19. Yu. L. Klimontovich, Usp. Fiz. Nauk **167**, 23 (1997) [Phys. Usp. **40**, 21 (1997)].
20. Yu. L. Klimontovich, *Statistical Physics of Open Systems* (Yanus, Moscow, 1995; Kluwer, Dordrecht, 1995), Vol. 1.
21. S. A. Reshetnyak and L. A. Shelepin, *Quasi-Steady Distributions in Kinetics* (IPO Avtor, Moscow, 1996).
22. G. M. Zaslavsky, Chaos **4**, 589 (1994).
23. A. V. Chechkin and V. Yu. Gonchar, Zh. Éksp. Teor. Fiz. **118** (3), 730 (2000) [JETP **91**, 635 (2000)].
24. K. V. Chukbar, Zh. Éksp. Teor. Fiz. **108** (5/11), 1875 (1996) [JETP **81**, 1025 (1996)].
25. J. R. Albritton, Phys. Rev. Lett. **50**, 2078 (1983).
26. J. R. Albritton, E. A. Williams, I. B. Bernstain, and K. P. Swartz, Phys. Rev. Lett. **57**, 1887 (1986).
27. O. G. Bakunin and S. I. Krasheninnikov, Fiz. Plazmy **21**, 532 (1995) [Plasma Phys. Rep. **21**, 502 (1995)].
28. N. L. Aleksandrov, A. M. Volchek, N. A. Dyatko, *et al.*, Fiz. Plazmy **14**, 334 (1988) [Sov. J. Plasma Phys. **14**, 196 (1988)].
29. S. I. Braginskii, in *Reviews of Plasma Physics*, Ed. by M. A. Leontovich (Gosatomizdat, Moscow, 1963; Consultants Bureau, New York, 1965), Vol. 1.
30. N. G. van Kampmen, *Stochastic Processes in Physics and Chemistry* (Vysshaya Shkola, Moscow, 1990).
31. V. P. Silin, *Introduction to Kinetic Gas Theory* (Nauka, Moscow, 1971).

Translated by I.A. Kalabalyk

Plasma Physics Reports, Vol. 29, No. 9, 2003, pp. 789–795. Translated from Fizika Plazmy, Vol. 29, No. 9, 2003, pp. 851–857.

LOW-TEMPERATURE PLASMA

Controlling Plasma Composition during Carbon Film Deposition in Microwave Discharges by Means of Optical-Emission Spectroscopy

V. V. Dvorkin, N. N. Dzbanovskiĭ, P. V. Minakov, N. V. Suetin, and A. Yu. Yur'ev

Skobeltsyn Institute of Nuclear Physics, Moscow State University, Vorob'evy gory, Moscow, 119899 Russia

Received January 23, 2002; in final form, February 13, 2003

Abstract—Optical emission spectra from the microwave discharge plasma that is used to activate gas-phase deposition of carbon films are systematically investigated under various deposition conditions. The line emission intensities from CH and C_2 radicals, which are responsible for the growth of the diamond and graphite phases, respectively, are studied as functions of the main macroparameters of the process. To find the relation between the features of the emission spectra and the composition of the films obtained, the films were examined using Raman spectroscopy and electron microscopy. It is shown that monitoring the relative intensities of the spectral lines can be used to obtain the desired type of film, in which case the state of the substrate surface and the presence of a catalyst on it also play an important role. Experiments on the deposition of carbon films in the pulsed regime of plasma excitation show the possibility of changing the phase composition of the film by varying both the pulse repetition rate and the off-duty factor. At the same average microwave power, the rate of film deposition in the pulsed regime of plasma excitation is lower than that in a continuous discharge; however, the growth rate of the graphite phase decreases insignificantly. *© 2003 MAIK "Nauka/Interperiodica"*.

1. INTRODUCTION

Microwave discharges are widely used to activate gas-phase deposition of various carbon films (poly- and monocrystalline diamond films, diamond-like films, and nanocarbon films) and carbon nanotubes [1, 2]. The structure and composition of these coatings depend on the macroparameters of the process, such as the microwave power, gas mixture composition, pressure in the working chamber, substrate temperature, etc. [3, 4]. According to the experimental data, even small variations in these parameters significantly affect the film properties. Moreover, the properties of the films obtained under identical conditions can depend on the initial transition processes. All this necessitates *in situ* monitoring of the gas-phase and surface processes. One of the most simple and efficient methods for such monitoring is the plasma optical-emission spectroscopy (OES), which consists in recording plasma emission in the spectral range of interest.

Under proper conditions, OES can be used to determine the electron, vibrational, and rotational temperatures of the gas mixture [5]. It is especially interesting to quantitatively determine the plasma composition (the concentrations of atoms and radicals involved in plasmochemical reactions) and to study the influence of various parameters on the characteristics of the carbon films obtained [6, 7].

In recent years, a new modification of the method of gas-phase deposition of carbon films—activation by a pulsed microwave discharge—has been developed [8, 9]. In the regime of pulsed plasma excitation, during the time intervals between the pulses, the radicals and ions recombine with a characteristic time on the order of a few milliseconds. The difference between the recombination rates for different plasma components responsible for the growth or etching of different carbon phases allows one to shift the deposition process toward the production of films with the desired characteristics by varying the pulse parameters (application of this method to depositing diamond films was studied in detail in [9]). Thus, varying the pulse repetition rate and off-duty factor gives an additional degree of freedom when finding optimal conditions for the deposition of the desired type of film. By using OES, one can monitor the concentrations of the plasma components, and, by varying the pulse parameters, it is possible to control the plasma composition and, accordingly, the film structure.

The aim of this study is to systematically investigate the optical spectra from microwave discharges operating over a wide range of powers, pressures, and concentrations during the deposition of amorphous, nanocrystalline, microcrystalline, and doped diamond films, as well as carbon nanotubes. The characteristic features of the plasma used for the pulsed deposition of these coatings at different pulse repetition rates are also examined.

1063-780X/03/2909-0789$24.00

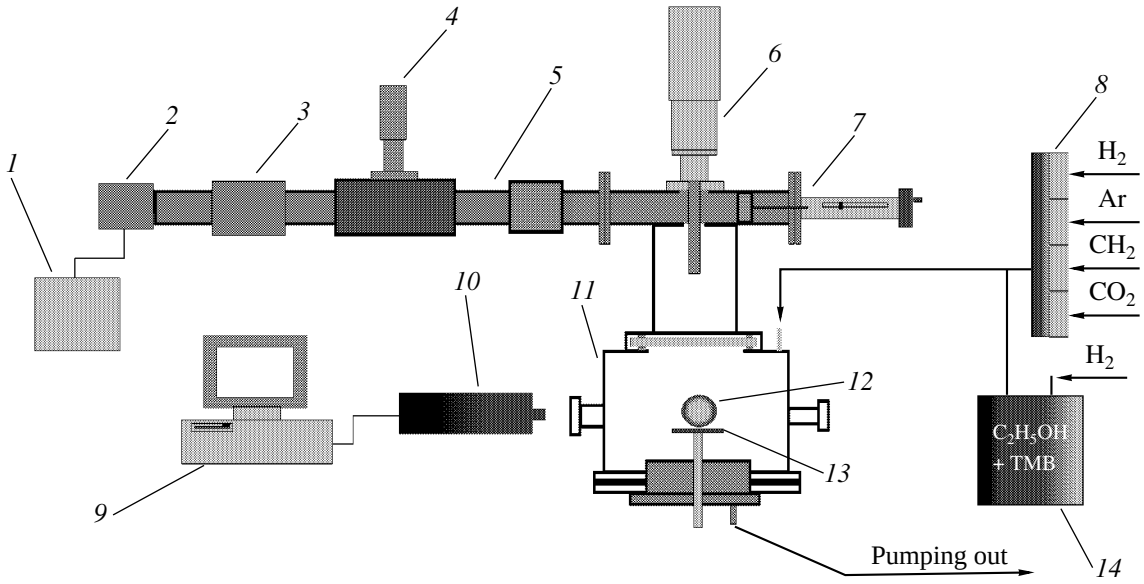

Fig. 1. Schematic of the experimental facility: (*1*) magnetron power supply, (*2*) magnetron (6 kW, 2.45 GHz), (*3*) ferrite circulator, (*4*) attenuator, (*5*) waveguide, (*6*) rod, (*7*) shorting plunger, (*8*) flowmeter unit, (*9*) PC, (*10*) monochromator with a recording device, (*11*) cavity, (*12*) plasma, (*13*) substrate holder, and (*14*) thermostabilized vapor source.

2. EXPERIMENT

2.1. Experimental Facility

The experiments were carried out at the microwave cavity device designed by the conventional scheme including a microwave section, gas channel, and discharge chamber (see Fig. 1).

A 6-kW microwave power generated by a magnetron operating at a frequency of 2.45 GHz was supplied through matching elements and a waveguide to the working chamber. The discharge was ignited in the working volume (cavity) of the chamber in the antinode of the microwave electric field. The cavity design ensured that the microwave energy was focused in the region above the substrate holder (made of molybdenum) so that the discharge plasma was in the immediate vicinity of the substrate. To carry out experiments in the pulsed regime of plasma excitation and film deposition, the magnetron output power could be modulated at a frequency from 100 Hz to 3 kHz with an off-duty factor of 2 or higher. Two viewing windows in the chamber sidewall allowed one to measure the substrate temperature and record the plasma emission spectra. The substrate temperature was measured with the help of a Williamson Pro 90 double-beam pyrometer.

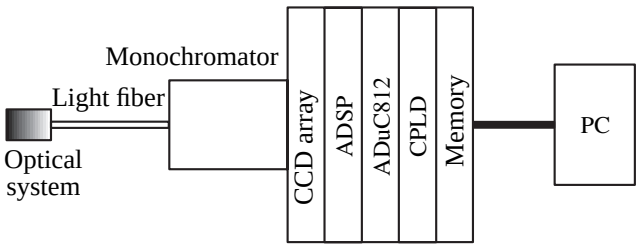

Fig. 2. Block scheme of OES system. The blocks located between the CCD array and the memory are the analog device signal processor (ADSP) of the CCD array, a 12-bit analog-to-digital converter (AduC812), and the controller of the programmable logic device (CPLD).

The working gas mixture was introduced directly into the discharge region through an inlet in the upper wall of the discharge chamber. When employing liquid sources of carbon (e.g., a mixture of ethanol with trimethylborate), we used a thermostabilized vaporizer, in which hydrogen was passed through the liquid; then, the mixture produced entered the reactor. By varying the temperature of the liquid, we could vary the vapor concentration in the working mixture. The required temperature of the liquid phase was sustained by a Peltier element; the system described allowed us to control the ethanol temperature in the range from –10 to +10°C with an accuracy of no worse than 0.1°C. When employing a gaseous source of carbon (methane, propane), the gas mixture composition was monitored with the help of flowmeters. The pumping-out of the gas mixture was performed near the removable part of the chamber bottom. The pressure p in the chamber was varied in the range 40–160 torr.

To diagnose the discharge plasma, we designed a spectroscopic system (Fig. 2) that enabled us to measure the plasma emission spectrum in the wavelength range from 350 to 800 nm with a resolution of 0.5 nm. The spectroscopic system, which was connected to the viewing window, consisted of an optical system with a light chopper, a quartz light fiber, a B&M Spektronik

BM-100 monochromator with a resolution of 0.83 nm/mm and a focal distance of 100 cm, a Toshiba TCD1201 CCD array with a digitizer board, a controller, and a PC with software for processing the spectral data.

2.2. Sample Preparation

The sample preparation procedure was determined by the desired film type. Specifically, to deposit a diamond film, a nanodiamond suspension in a photoresist was deposited onto a Si(100) surface. This technique enabled us to obtain a nucleation site density of 10^{10}–10^{11} cm^{-2}. To grow CNTs, a silicon surface was covered with a 100-nm titanium barrier diffusion layer and, over it, a 10- to 20-nm layer of Ni or Co catalyst.

We carried out experiments in hydrogen, in mixtures of H_2 with C_2H_5OH (the ethanol content was 6.4–13.6%), and in CH_4 : H_2 mixtures within the pressure range 40–80 torr. To obtain doped diamond films (DDFs), a trimethylborate was added to the mixture. The concentration of trimethylborate in the liquid mixture was 3%. In the experiments, the substrate temperature was within the range 700–800°C. The microwave power deposited into the discharge was varied from 500 to 1500 W. Under these conditions, the gas temperature of the plasma was typically no higher than 2500 K [10]. At a degree of ionization of 10^{-6}, the electron temperature was in the range 1.3–1.7 eV [10, 11]; in this case, the degree of dissociation of hydrogen could be as high as 15% [10].

2.3. Methods for Studying the Films Obtained

The morphology of the films obtained was studied by using a scanning electron microscope (SEM) with a resolution of 10 nm. Raman spectroscopy in the range 500–2000 cm^{-1} was used to study the phase composition of the films.

3. RESULTS OBTAINED

A typical emission spectrum from the plasma of a H_2 : C_2H_5OH : $(CH_3O)_3B$ gas mixture that was used to deposit a diamond film is shown in Fig. 3. Intense molecular bands corresponding to the C_2, $d^3\Pi_g \longrightarrow a^3\Pi_u$ (λ = 471.5, 473.7, 512.9, 516.5, 558.5, and 563.5 nm) and CH $A^2\Delta \longrightarrow X^2\Pi$ (λ = 431.4 nm) transitions are clearly seen in the spectrum. The spectral lines were identified using the data from [12, 13].

The intensity ratios of the characteristic lines of C_2 ($d^3\Pi_g \longrightarrow a^3\Pi_u$, 516.5 nm), CH ($A^2\Delta \longrightarrow X^2\Pi$ 431.4 nm), and H (H_β, H(n = 4) $\longrightarrow$ H(n = 2), 486.1 nm; H_α, H(n = 3) $\longrightarrow$ H(n = 2), 656.3 nm) are of especial interest because the C_2H_x and CH_x radicals take part in the formation of different carbon phases, whereas atomic hydrogen participates in their etching.

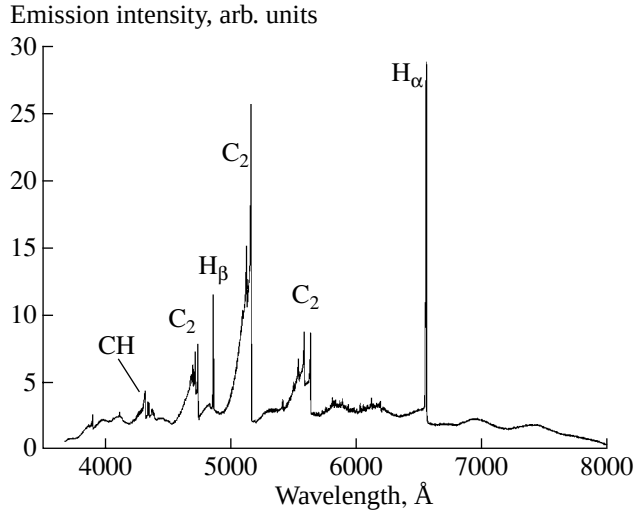

Fig. 3. Emission spectrum from the plasma of an H_2 : C_2H_5OH : $(CH_3O)_3B$ working gas mixture.

The ratio between the radical densities affects the morphology of the films obtained. The implementation of OES for determining the absolute or relative concentration of an individual ingredient in the discharge is rather complicated because the discharge properties in experiments on the deposition of carbon films are such that the requirements imposed by different measurement methods (e.g., that the plasma be optically transparent and be in an equilibrium state) are usually not met in practice. However, the measurements of the relative intensities of the lines of the radicals that are of most importance for the growth of carbon films can be used to determine the channels for film growth; namely, a change in the ratio of the line intensities $[C_2]/[CH]$ can reflect the change in the sp^2/sp^3 ratio in the film obtained. In this connection, we performed a series of experiments aimed at elucidating the dependence of the relative intensities of the above lines on the variations in the most important technological macroparameters. Concurrently, the films produced were analyzed by using Raman spectroscopy and an SEM.

3.1. Experiments on the Deposition of Doped Diamond Films

To determine the influence of the microwave power and the ethanol concentration on the film composition (provided that all the other deposition conditions are kept constant: p = 80 torr, the hydrogen gas flow rate is 10 l/h, and the substrate temperature T_{sub} = 800°C), the spectra were studied as functions of the deposited power varying in the range 700–1200 W and the ethanol concentration in the gas mixture varying from 7 to 13.6% (the regime of DDF deposition). When varying the power, the ethanol concentration was kept at a level of 13%, and when varying the ethanol concentration,

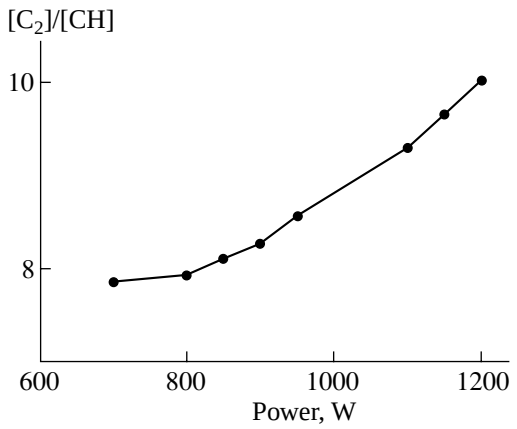

Fig. 4. Intensity ratio $[C_2]/[CH]$ vs. input microwave power.

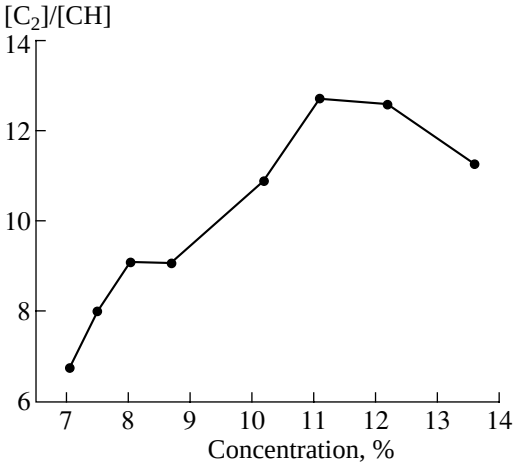

Fig. 5. Intensity ratio $[C_2]/[CH]$ vs. total concentration of C_2H_5OH and $(CH_3O)_3B$ in the working mixture.

the power was kept equal to 900 W. The dependences obtained are shown in Figs. 4 and 5.

It can be seen from Fig. 4 that the $[C_2]/[CH]$ ratio monotonically increases with increasing power. The content of the sp^2 phase in the films increases in the same manner. At high powers, there is a tendency toward the growth of cauliflower-like clusters on the sample surface. The best-quality diamond films were deposited at low powers. This fact can be explained by the increase in the degree of dissociation of hydrocarbons (and, consequently, the increase in the production rate of C_2 radicals acting as sites in which the sp^2 phase originates) with increasing microwave power.

As the ethanol concentration increases, the $[C_2]/[CH]$ ratio first increases and then, after reaching a maximum value of 11%, begins to decrease (Fig. 5). The best-quality diamond films were obtained at an ethanol concentration of 13.6%. Figure 6a presents an SEM photograph of such a film (the growth time is four hours). The film is a continuous polycrystalline structure with a typical size of crystalline grains of a few microns. The Raman spectrum of the film is shown in Fig. 7. It is seen that a diamond line is only present in the spectrum.

For a wide range of applications, the films must be deposited selectively [14, 15]. This can be ensured by employing a selective process of nucleation with the help of a nanodiamond-containing photoresist and a conventional lithography technique. An SEM photograph of a film thus obtained is shown in Fig. 6b. It is clearly seen that the film grows only at the points at which the initial nucleation sites occurred, whereas in all the other regions, no film was deposited although the concentrations of active radicals and chemical components were the same throughout the entire gas phase. Therefore, the presence of the required gas-phase composition is a necessary, but in sufficient, condition for the growth of diamond films; the structure and condition of the substrate surface are also of great importance.

Nevertheless, the experimental results show that the monitoring of the $[C_2]/[CH]$ ratio can be used to determine, e.g., the optimal power required to obtain a desired type of carbon film. Apparently, in order to use OES to determine the optimum ethanol concentration, it is also necessary to take into account oxygen lines when measuring the ratios of the spectral line intensities.

As a diamond film grows, the methane concentration in the $CH_4 : H_2$ gas mixture increases from 0.5 to 14%. In contrast to the case with ethanol, both the $[C_2]/[CH]$ ratio and the content of the diamond phase in the film monotonically increase. In the concentration range 0.5–2.5%, polycrystalline diamonds grow. At elevated concentrations (up to 10%), cauliflower-like coatings were produced. At even higher concentrations, nanocrystalline and amorphous carbon films were obtained.

3.2. Experiments on the Growth of Carbon Nanotubes

Preliminary studies showed that the composition and structure of the films produced from a $CH_4 : H_2$ mixture significantly depend on the methane concentration. However, without special treatment of the substrate surface on which the films grow, no nanocarbon tubes arise. To obtain carbon nanotubes, some amount of catalyst (iron, nickel, cobalt, etc.) should be deposited on the substrate surface. This was done either by magnetron sputtering with subsequent annealing (as a result, metal clusters with dimensions of 10–50 nm are formed) or by means of chemical (electrochemical) deposition of the catalyst nanoparticles. Typical conditions under which CNTs were deposited are as follows: a pressure of 80 torr, microwave power of 400 W, and

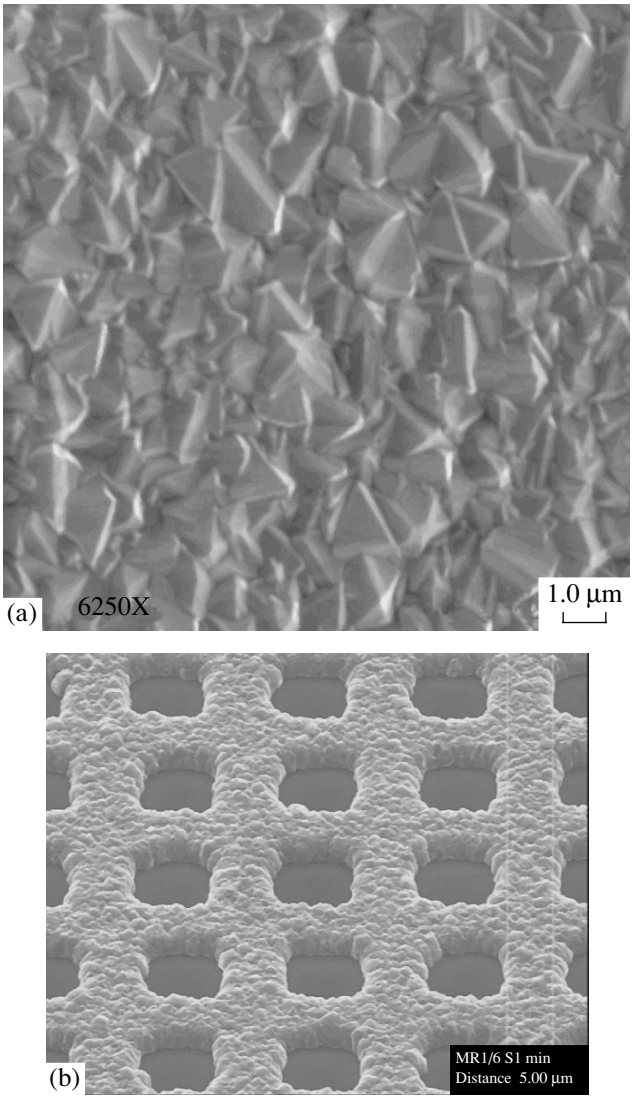

Fig. 6. SEM photographs of (a) a high-quality DDF on a silicon surface and (b) a selectively grown high-quality DDF.

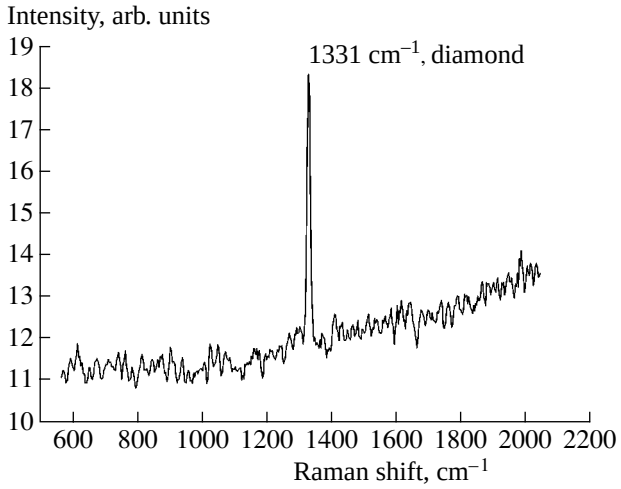

Fig.7. Raman spectrum of the high-quality DDF shown in Fig. 6a.

substrate temperature of 790°C. The measured dependences of the ratios of the spectral line intensities on the gas pressure and the methane concentration are shown in Figs. 8 and 9, respectively. The intensity of the CH line changes only slightly throughout the entire range in which the methane concentration and the gas pressure vary. In contrast, the intensity of the C_2 line significantly increases with increasing gas pressure or methane concentration. For example, as the methane concentration increases from 2.5 to 14%, the intensity of the C_2 line monotonically increases by nearly two orders of magnitude, which allows one to expect a significant increase in the content of the graphite phase in films at high methane concentrations in the mixture. The studies of the films obtained with the help of an SEM and Raman spectroscopy confirm this prediction: for substrates covered with a Ti–Ni layer, no film was deposited at CH_4 concentrations lower than 8%, whereas at concentrations of 8–14%, a growth of amorphous carbon was observed.

In this study, we did not work with higher concentrations of CH_4. To obtain nanotubes, we used an original deposition scheme with a graphite grid as an extra electrode placed near the substrate surface. This scheme allowed us to reduce the degree of film etching by atomic hydrogen and increase the carbon concentration in the plasma. A graphite grid with 1-mm-diameter holes and a grid pitch of 2 mm was installed close to the sample at a distance of 2 mm above it. It was supposed that, in the gap between the grid and the sample, the carbon concentration would significantly increase and the hydrogen concentration would decrease, which would stimulate the formation and growth of CNTs. In the methane concentration range 8–14%, the growth of nanotubes on the nickel surface was observed (Fig. 10). The use of an additional electrode allows one, if necessary, to vary the sample potential with respect to the plasma potential in order to provide, e.g., the aligned growth of nanotubes and additional nucleation. In these experiments, we did not applied OES to study emission from the gap; this is a subject for our further research.

3.3. Effect of the Pulsed Regime of Plasma Excitation on the Process of Carbon Film Deposition

The use of the pulsed regime of plasma excitation (with a pulse repetition rate of 500 Hz and an off-duty factor of 2) enabled us to widen the parameter range corresponding to the growth of high-quality diamond films, which agrees with the data of [9].

In the experiments on the growth of CNTs in the pulsed regime of plasma excitation (with a pulse repetition rate of 500–1500 Hz and an off-duty factor of 2), a series of CNT films were successfully grown. Figure 11 shows the Raman spectrum of a CNT film obtained

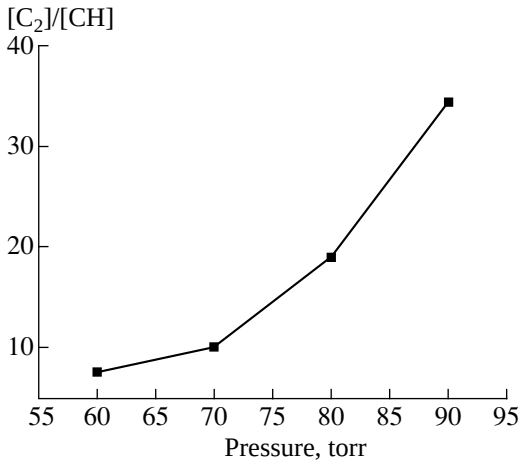

Fig. 8. Intensity ratio $[C_2]/[CH]$ vs. pressure.

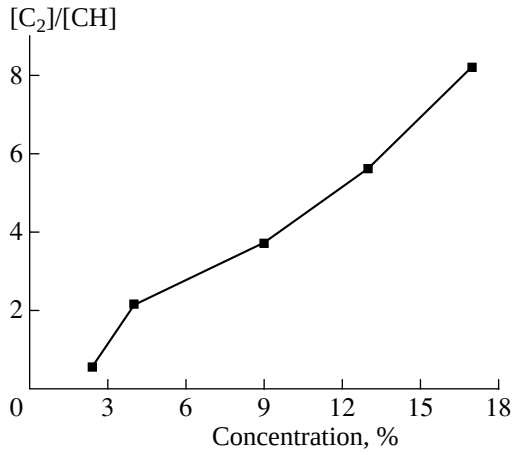

Fig. 9. Intensity ratio $[C_2]/[CH]$ vs. methane concentration.

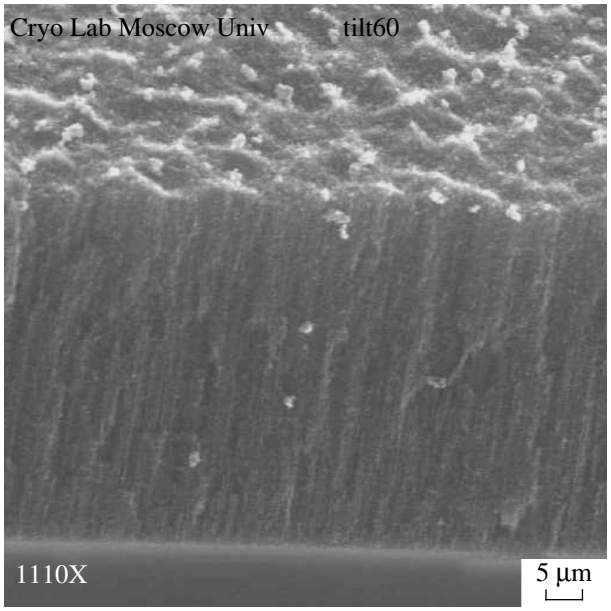

Fig. 10. SEM photograph of a CNT film.

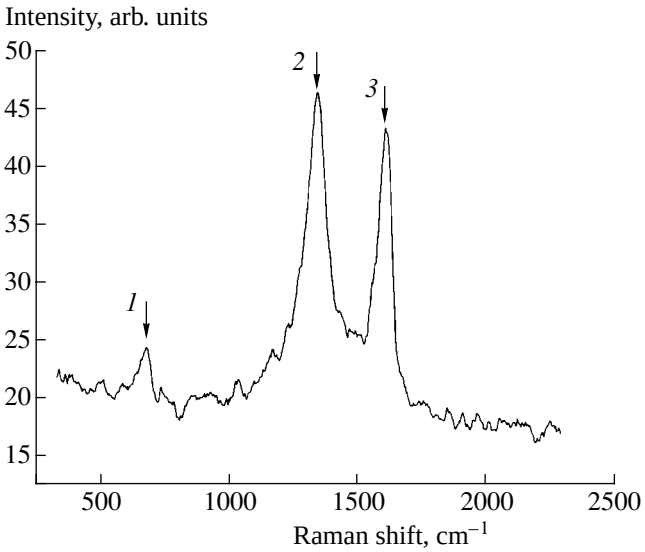

Fig. 11. Raman spectrum of a typical CNT film obtained in the pulsed regime of plasma excitation: (*1*) 697, (*2*) 1345, and (*3*) 1613 cm^{-1}.

in such a regime. The spectrum coincides with the spectrum of CNT films obtained in the continuous-wave regime. However, the experiments showed a significant decrease in the CNT growth rate as compared to the growth rates in the continuous-wave regime. The possible reason is the change of the kinetics of plasmochemical processes due to both the difference in the recombination rates of H and C_xH_y and the significant increase in the peak electric field in the pulsed regime as compared to that in the continuous-wave regime at the same average microwave power. When comparing the emission spectra obtained in the pulsed and continuous-wave regimes, it was revealed that, in the pulsed regime, the intensity of the C_2 line is significantly lower, which explains the sharp decrease in the CNT growth rate. We note that the modulation of the microwave power leads to an insignificant decrease in the intensities of the H and CH lines; this fact manifests itself in an insignificant decrease in the growth rate of the film. Another feature of the plasma emission spectrum in the pulsed regime is a strong increase in the intensity of the Fulcher band of the vibrational transitions of an H_2 molecule ($d^3\Pi_u \longrightarrow a^3\Sigma_g^+$, λ = 599–640 nm).

Later, we are going to use a time-resolved OES technique to measure the lifetimes of C_2 and CH radicals

and atomic hydrogen, which will allow us to controllably vary the $[C_2]/[CH]$ ratio by varying the parameters of the pulsed regime of plasma excitation.

4. CONCLUSION

Optical-emission spectra from a microwave discharge plasma during the gas-phase deposition of carbon films have been analyzed under various deposition conditions. The characteristic features of the pulsed regime of plasma excitation have been studied. The line emission intensities of CH and C_2 radicals, which are responsible for the growth of the diamond and graphite phases, respectively, have been studied as functions of the deposition conditions, such as the gas mixture composition, the microwave power, and the pressure in the discharge chamber. It is shown that the monitoring of the relative intensities of certain spectral lines allows one to control the morphological and phase characteristics of the films produced.

The presence of the required gas-phase composition is a necessary (but not sufficient) condition for the growth of diamond films and carbon nanotubes. The structure and state of the substrate surface, as well as the presence of a catalyst on it, are also of great importance.

ACKNOWLEDGMENTS

We are grateful to M.A. Timofeev and V.G. Pirogov for useful discussions and for their help in studying the samples obtained. This study was supported in part by the NATO Scientific Affairs Division (grant no. SfP-974354) and ISTC (project no. 2484).

REFERENCES

1. S.-P. Hong, H. Yoshikawa, K. Wazumi, *et al.*, Diamond Relat. Mater. **11**, 877 (2002).
2. U. Kim, R. Pcionek, D. M. Aslam, *et al.*, Diamond Relat. Mater. **10**, 1947 (2001).
3. P. K. Bachmann, D. Leers, and H. Lydtin, Diamond Relat. Mater. **1**, 1 (1991).
4. W. Ahmed, C. A. Rego, R. Cherry, *et al.*, Vacuum **56**, 153 (2000).
5. J. Ropcke, M. Kaning, and B. P. Lavrov, J. Phys. IV (France) **8** (7), 207 (1998).
6. D. M. Gruen, C. D. Zuiker, A. R. Krauss, *et al.*, J. Vac. Sci. Technol. A **13**, 1628 (1995).
7. Y. S. Woo, D. Y. Leon, I. T. Han, *et al.*, Diamond Relat. Mater. **11**, 59 (2002).
8. J. Khachan, B. W. James, and A. Marfoure, Appl. Phys. Lett. **77**, 2973 (2000).
9. L. de Poucques, J. Bougdira, R. Hugon, *et al.*, J. Phys. D **34**, 896 (2001).
10. A. Gicquel, K. Hassouni, F. Farhat, *et al.*, Diamond Relat. Mater. **3**, 581 (1994).
11. S. Narishige, S. Suzuki, M. D. Bowden, *et al.*, Jpn. J. Appl. Phys. **39**, 6732 (2000).
12. R. W. B. Pearse and D. V. Gaydon, *The Identification of Molecular Spectra* (Chapman and Hall, London, 1976).
13. G. Herzberg, *Molecular Spectra and Molecular Structure*, Vol. 1: *Spectra of Diatomic Molecules* (D. van Nostrand, New York, 1951).
14. V. V. Dvorkin, N. N. Dzbanovskiĭ, P. V. Minakov, *et al.*, in *Proceedings of the 3rd International Symposium on Theoretical and Applied Plasmochemistry, Ivanovo-Ples, 2002*, Vol. 2, p. 287.
15. E. A. Poltoratskiĭ, G. S. Rychkov, E. A. Il'ichev, *et al.*, in *Proceedings of the International Science and Technology Conference on Thin Films and Layered Structures, Moscow, 2002*, Part 2, p. 228.

Translated by N.N. Ustinovskiĭ

Plasma Physics Reports, Vol. 29, No. 9, 2003, pp. 796–801. Translated from Fizika Plazmy, Vol. 29, No. 9, 2003, pp. 858–864.

LOW-TEMPERATURE PLASMA

Glow Intensity Profile in a Spherically Stratified Gas Discharge

O. A. Nerushev, S. A. Novopashin, V. V. Radchenko, G. I. Sukhinin, and V. V. Sukhovskiĭ

Institute of Thermophysics, Siberian Division, Russian Academy of Sciences, pr. Akademika Lavrent'eva 1, Novosibirsk, 630090 Russia

Received January 23, 2003; in final form, March 20, 2003

Abstract—The glow intensity profile in a spherically stratified gas discharge is measured. It is shown that the boundaries of striations are thin spherical glowing shells, whose thickness is proportional to the striation radius. Based on the analysis of the optical-emission characteristics of spherical striations, the spatial distribution of the electric field in the stratified discharge region is estimated. © *2003 MAIK "Nauka/Interperiodica".*

1. INTRODUCTION

Stratification of the positive column of a dc gas discharge in a tube is a well-known and thoroughly investigated phenomenon [1–4]. A similar phenomenon was experimentally observed in a volume gas discharge [5–8]. In this case, the cathode is the metallic wall of the discharge chamber and the anode is a small electrode placed in the center of the chamber. Under certain conditions, the glow of the discharge region that corresponds to the positive column of a discharge in a tube has the form of nested spherical shells. By analogy with tube discharges, this phenomenon was called spherical stratification.

Because of the different geometries of the discharge gap, the plasma characteristics are also different. The main differences are as follows:

(i) In linear geometry, the current density is constant along the current lines, whereas in spherical discharges, it increases toward the central electrode.

(ii) In tube discharges, recombination occurs mainly on the tube wall [4], whereas in spherical discharges, only volume recombination is possible.

(iii) In spherical geometry, the voltage polarity is of importance. Stratification occurs only when a positive voltage is applied to the central electrode.

(iv) Because of the radial inhomogeneity of a spherical discharge, the local gradients of the current density vary by two orders of magnitude within the stratified region, and the relative contributions of the drift and diffusion components of the current can vary over a wide range.

(v) In a spherical discharge, the problem is strictly one-dimensional, in contrast to tube discharges, in which, due to charge accumulation on the tube wall, the electric field component normal to the direction of the average current arises.

Because of these differences, the nature of stratification in spherical discharges differs significantly from that in gas-discharge tubes. In particular, no spherical stratification was recorded in discharges in pure gases; it was observed only either after adding the high-molecular additives [7] or at a highly inhomogeneous distribution of the density of the working gas flowing out with a supersonic velocity from the anode [8]. In this study, which is based on the measurements of the striation glow intensity, we theoretically analyze the possible radial profile of the electric field in a spherical discharge and compare it with floating potential measurements.

2. EXPERIMENTAL SETUP

The experiments were carried out with a cylindrical steel chamber 60 cm in height and 50 cm in diameter. In the center of the chamber, a 0.5-cm-radius steel ball was placed. A positive voltage of U_0 = 0–2000 V was applied from a high-voltage power supply to the ball through a ballast resistance of 5–24 kΩ. The grounded chamber wall acted as a second electrode (cathode). The chamber was pumped out to a residual pressure of $p \sim 0.1$ Pa and then filled with a working gas mixture. The discharge current was varied by varying the output voltage U_0 of the power supply. The discharge was ignited after a positive dc voltage higher than the breakdown voltage was applied to the central electrode.

After the discharge ignition, from one to ten (or even more) striations were observed, depending on the gas mixture pressure p, acetone concentration η, and discharge current J. In the experiments reported in this paper, the discharge operated in nitrogen with a 15% admixture of acetone vapor at a total pressure of p = 25 Pa. In this case, from one to five striations were observed, depending on the discharge current.

1063-780X/03/2909-0796$24.00

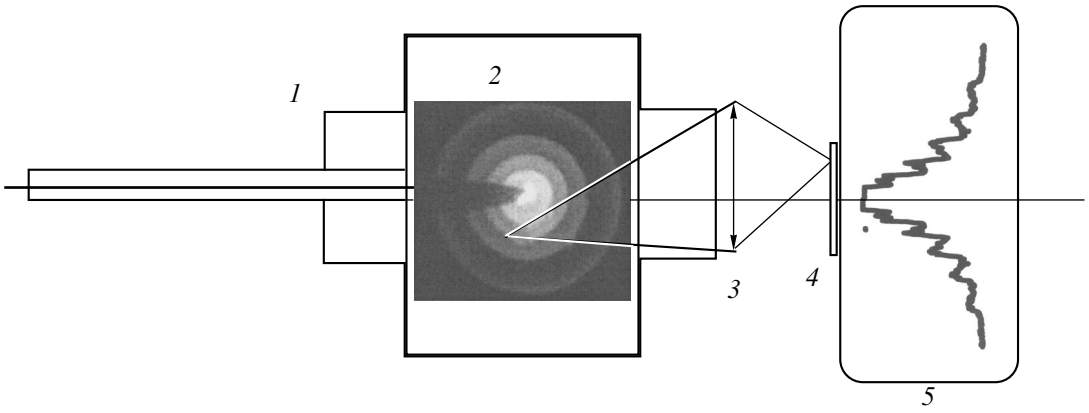

Fig. 1. Schematic of the experimental facility: (*1*) discharge chamber, (*2*) glow region, (*3*) focusing lens, (*4*) multichannel radiation analyzer, and (*5*) digitized image display.

The chamber was equipped with transparent windows for visual observations, photographing the discharge, and recording the spatial distribution of the glow intensity in the visible region by using a multichannel emission analyzer. The analyzer was a photodiode array composed of 1024 elements with a total length of 2.5 cm and height of 150 μm. The analyzer was equipped with a 12-digit analog-to-digital converter, a controller, and an interface through which the analyzer was connected to a PC. The minimum exposition time was 2 ms, and the data transfer time was about 10 ms. An optical system produced the discharge image on the surface of the photodiode array. The spatial resolution of the optical system in the object plane, which passed through the central electrode (Fig. 1), was 0.1–0.2 mm.

3. RESULTS AND DISCUSSION

The inset in Fig. 1 shows a photograph of a stratified discharge (with five striations) in air with a 15% admixture of acetone vapor at a discharge current of 50 mA and total pressure of 25 Pa. Figure 2 presents the results of measurements of the intensity of optical emission from a spherical discharge under the same conditions (curve *1*). The measured intensity profile corresponds to the signal recorded by the multichannel optical analyzer, onto which the discharge emission was projected. One can see that the discharge emission is modulated by striations; however, the modulation is somewhat smoothed by the optical system. The solid curves in Figs. 3 and 4 show the results of measurements of the emission intensity at the same pressure and composition of the gas mixture, but at different discharge currents (25 and 15 mA, respectively). It can be seen that the number of striations and their dimensions (radii) vary with varying discharge current. The total glow intensity is nearly proportional to the discharge current. In Fig. 4, the emission from the cathode sheath is also present (marked by arrow). It should be noted that the images obtained do not reproduce the actual distributions of the glow intensity over the discharge cross section but reflect the emission intensity integrated along the line of sight. In this context, let us consider in more detail the system for recording optical information and methods for its processing.

It is worth noting that, being averaged over a series of measurements at different discharge currents, the radial dependence of the glow intensity normalized to the discharge current can be well fitted by the exponential dependence

$$\bar{I}_m(\rho) = \frac{1}{K}\sum_k \frac{I_{m,k}(\rho)}{J_k} \approx \bar{I}_0 \exp(-\alpha\rho), \qquad (1)$$

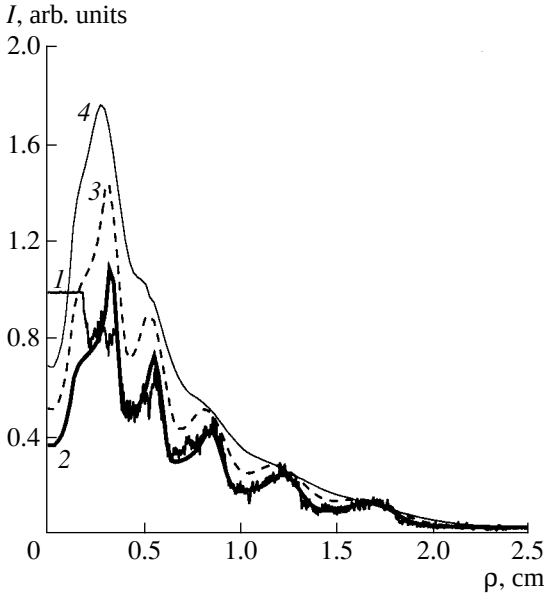

Fig. 2. Glow intensity profile in the image plane for p = 25 Pa and J = 35 mA. Curve *1* shows the experimental data, and the other curves show the simulation results for different relative striations widths: γ_k = (*2*) 0.035, (*3*) 0.07, and (*4*) 0.1. The abscissa is the distance in the image plane (the plane of the radiation detector).

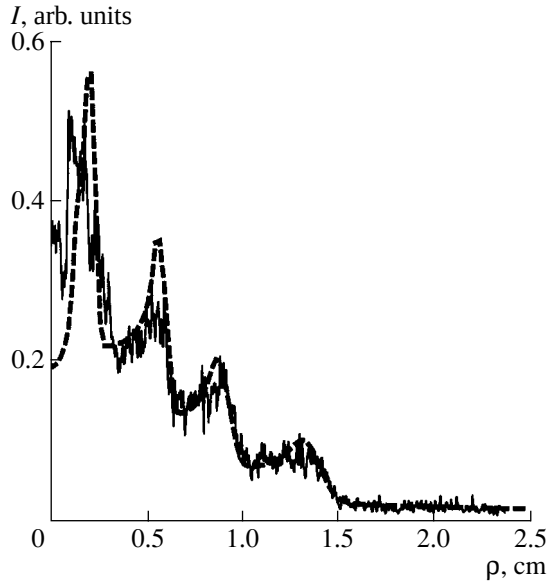

Fig. 3. Glow intensity profile in the image plane for p = 25 Pa and J = 25 mA. The solid curve shows the experimental data, and the dashed curve shows the simulation results for the relative striation width $\gamma_k = 0.035$. The abscissa is the same as in Fig. 2.

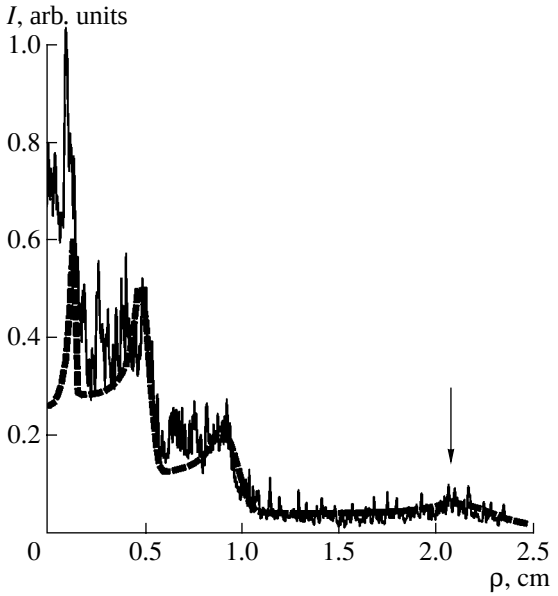

Fig. 4. Glow intensity profile in the image plane for p = 25 Pa and J = 15 mA. The solid curve shows the experimental data, and the dashed curve shows the simulation results for the relative striation width $\gamma_k = 0.035$. The abscissa is the same as in Fig. 2.

where $I_{m,k}(\rho)$ is the emission intensity at the point ρ in the image plane for the kth regime with the discharge current J_k, K is the number of regimes with different discharge currents at a given density and a given composition of the working mixture, and α is the empirical coefficient.

To interpret the distribution of the recorded optical signal, we developed a simple geometrical-optics model.

It was assumed that, in view of the spherical symmetry of the discharge, the radiation density $I_d(r)$ at a point with coordinates r, θ, and φ inside the discharge depends only on the radius r. The intensity of isotropic emission from the volume element surrounding this point is

$$dI = I_d(r)r^2 dr \sin\theta d\theta d\varphi. \quad (2)$$

This emission is projected by a lens onto the image plane, in which the radiation analyzer is placed (see Fig. 1). The radiation emitted from the plane that passes through the center of the discharge chamber is focused directly on the image plane. The radiation emitted from a certain point at the front hemisphere of the discharge is focused by the lens onto some point on the surface of an ellipsoid in front of the image plane; then, this radiation diverges and produces a blurred spot on the image plane. The radiation emitted from the rear hemisphere of the discharge is focused behind the image plane; therefore, it also produces a blurred spot on the image plane. Thus, when the emission from a spherical discharge is projected onto the image plane, the image obtained turns out to be smeared out. The signal recorded is an integral convolution of the emission intensity profile with the instrumental function of the optical system, which can be found either experimentally or by geometrical-optics modeling with allowance for the parameters of the optical system. In this case, the details of the radial structure of the discharge beyond the object plane are somewhat smoothed when projecting onto the image plane.

The distribution of the emission density along the photodiode array $I_m(\rho)$ can be represented in the form of the convolution of the radial profile of the emission intensity $I_d(r)$:

$$I_m(\rho) = \int_0^R K(\rho, r) I_d(r) r^2 dr, \quad (3)$$

where the transformation kernel $K(\rho, r)$ for the given optical system (Fig. 1) is determined by the formulas of geometrical optics by integrating over the angular variables θ and φ. Figure 5 shows the kernel $K(\rho, r)$ as a function of ρ for r = 6 cm. In fact, the function $K(\rho, r)$ is an image of an infinitely thin glowing sphere with a radius r. It can be seen that the projection of a thin glowing shell onto the image plane (in which a photodiode array is placed) has the shape of a circle that is somewhat blurred toward the inner region; however, the outer edge of the image is fairly sharp. We note that it is the point close to the maximum intensity in the image plane (rather than the outer edge of the image) that corresponds to the radius of the glowing sphere. Taking

into account the optical transformation for a given optical system allows one to adequately reconstruct the distribution of the emission intensity in the discharge using the measured intensity profile in the image plane.

By analogy with gas-discharge tubes, we assume that the spherical striations in a spherical discharge are related to the formation of regions with a nonuniform spatial distribution of the electric field (electric double layers) and other discharge parameters between a small-sized (point) central anode and a surrounding cathode. At a given composition of the working mixture, the number of striations decreases with decreasing current density. In [7], it was shown that, when the discharge operates long enough without circulation of the working mixture, the strata disappear due to a change in the chemical composition of the plasma.

The spatial distribution of the emission intensity is governed by the electron density and the local electron energy distribution function (EEDF). In subsequent estimates, we will assume that the emission from a spherical gas discharge is caused by direct electron impacts. This assumption agrees with the linear dependence of the integral emission on the discharge current [see Eq. (1)]. Hence, in a frequency range $\Delta\nu$, the spectral intensity for a given optical transition is proportional to the product of the electron current density $j_e(r) \sim 1/r^2$ and the effective excitation function $\varphi_{\Delta\nu}(r)$, which depends on the local EEDF:

$$I_d(r) = C|j_e(r)|\varphi_{\Delta\nu}(r), \quad (4)$$

where C = const is the instrumental constant. Further, we will assume that the EEDF and, consequently, the excitation rate $\varphi(r)$ are determined by the local reduced electric field $E(r)/N$ at the point r. Hence, $\varphi(r)$ can be represented by the formula

$$\varphi_{\Delta\nu}(r) = A_{\Delta\nu}\exp\left[-\frac{B_{\Delta\nu}}{E(r)/N}\right], \quad (5)$$

where N is the gas density and $A_{\Delta\nu}$ and $B_{\Delta\nu}$ are the empirical constants that depend on the gas species and the spectral interval. Note that expressions (4) and (5) correspond to the semiempirical dependences of the coefficients of ionization and electron-impact excitation that are widely used in gas discharge physics [4].

Let us prove now that the spherical striations are related to the formation of electric double layers in which the electric field is peaked due to a significant space charge separation. Without going into details of the double layer formation, which is related to the joined action of the nonlinear and nonlocal kinetic and hydrodynamic phenomena in an inhomogeneous low-temperature discharge plasma (a comprehensive theory of these processes has not yet been developed), we will make some assumptions whose validity can only be confirmed by comparing with the experimental data. In this context, it should be noted that, in contrast to the optical recording of striations, the probe measurements in the given discharge geometry cannot be performed simultaneously in the entire volume. To determine the potential profile throughout the entire discharge volume, we used a 3-mm-long and 0.26-mm-diameter cylindrical probe that was moved inside the discharge chamber [7]. The measurement error was composed of the errors in measuring the electrical parameters, errors related to the non-steady-state character of the discharge, and errors associated with the perturbations introduced into the plasma by the probe itself. The spatial resolution of the probe measurements did not allow us to study in detail the profile of the potential in striations. This is related to the specific discharge geometry: the small-size anode and the tendency of spherical striations to form around electrodes of any shape. Even when the probe potential only slightly exceeds the local floating potential (which is necessary to measure the electron part of the current–voltage characteristic), the probe causes a significant change in the geometry of striations with a subsequent formation of the second anode and a decrease in the current to the main anode. Thus, the probe measurements can only be used for an indirect comparison with the results obtained from an analysis of the optical signal.

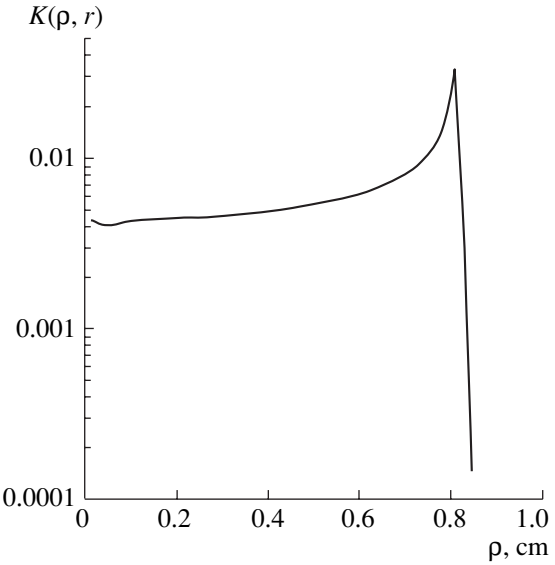

Fig. 5. Model kernel $K(\rho, r)$ of the integral transformation of the optical emission intensity as a function of ρ at r = 6 cm. The plotted curve corresponds to the distribution of the calculated emission intensity from a thin glowing sphere with radius r on the photodiode array.

To analytically describe the radial profile of the electric potential $U(r)$ in the "positive column" of a spherical discharge, we used the expression

$$U(r) = \frac{\Delta U_0}{2}\sum_{k=1}^{K}\left[\tanh\left(\frac{R_c - r_k}{\gamma_k r_k}\right) - \tanh\left(\frac{r - r_k}{\gamma_k r_k}\right)\right] + U_{\text{mon}}(r), \quad (6)$$

where r_k is the radius of the kth striation; $\Delta r_k = \gamma_k r_k$ is the width of the kth striation; ΔU_0 is the potential drop across the double layer (striation); and $U_{\text{mon}}(r)$ is a smooth monotonic function that describes the cathode fall and the slowly varying potential in the positive column, which are characteristic of a nonstratified discharge [7]. The coefficients γ_k, which are the relative widths of striations, will be determined below by comparing with the results of optical measurements. Potential profile (6) corresponds to the following radial profile of the electric field:

$$E(r) = -\frac{\partial U(r)}{\partial r} = \frac{\Delta U_0}{2}\sum_{k=1}^{K}\frac{1}{\gamma_k r_k}\cosh^{-2}\left(\frac{r-r_k}{\gamma_k r_k}\right) + E_{\text{mon}}(r), \quad (7)$$

where the first term describes the peaks of the electric field in the double layers and the second term, $E_{\text{mon}}(r)$, corresponds to the regular monotonic behavior of the electric field in the positive column and the cathode fall in the absence of striations. Note that, according to formula (7), the electric field in the kth striation is inversely proportional to its radius r_k,

$$E_k = E(r_k) \approx \frac{\Delta U_0}{2\gamma_k r_k}. \quad (8)$$

From Poisson's equation, one can find the space charge density, which is equal to the difference between the densities of the positive and negative charged particles,

$$\Delta n(r) = \frac{\varepsilon_0}{er^2}\frac{d}{dr}(r^2 E) = \frac{\varepsilon_0 \Delta U}{e}\sum_{k=1}^{K}\left[\gamma_k r_k \cosh^2\left(\frac{r-r_k}{\gamma_k r_k}\right)\right]^{-1}\left[\frac{1}{r} - \frac{1}{\gamma_k r_k}\tanh\left(\frac{r-r_k}{\gamma_k r_k}\right)\right] + \frac{\varepsilon_0}{er^2}\frac{d}{dr}[r^2 E_{\text{mon}}(r)]. \quad (9)$$

In this expression, the first term describes the space charge distribution in the double layers, which correspond to the peaks of the electric field (jumps in the potential), whereas the second term describes the space charge corresponding to the slowly varying electric field in the region between striations.

The striation radii r_k were determined by the above procedure from the experimental data presented in Figs. 2–4. A comparison of the model and experimental distributions of the emission intensity in the image plane showed that, within the measurement accuracy, the relative widths of striations γ_k can be considered equal, $\gamma \approx 0.03$–0.04. The increase in the parameter γ_k to 0.07 or higher leads to the smoothing of the calculated intensity distributions and the disappearance of the peaks in the calculated distribution (see Fig. 2). Similar dependences and similar relative widths were also found in other regimes. It is these peaks of the emission intensity profile that are responsible for the visually observed glow structure and that allow one to model the plasma of a stratified discharge with a set of concentric electric double layers [6, 8].

When estimating the energetic parameters, the potential drop ΔU_0 across a striation was set as constant and equal to 15 V, which corresponded to the measured (by the probe technique) voltage drop across a striation in the positive column of a stratified discharge in the mixture of nitrogen with acetone vapor. This qualitatively agrees with the observations of a similar spherically symmetric structure in the three-electrode scheme [9], where a spherical glow around an extra anode occurred only when the anode potential exceeded the plasma potential by no less than 20–30 V. The potential drop ΔU_0 is approximately equal to the gas ionization potential. This circumstance was previously used in the kinetic model to find the EEDF [6]. In the distributions measured in [7], the steplike structure of the floating potential in the striation region is feebly marked because of the large measurement errors and the influence of the probe. At the same time, the total voltage drop across the positive column is proportional to the total number of striations and the calculated potential drop across a striation coincides with the above estimate. In a nonstratified discharge, the total voltage drop between the anode and the boundary of the cathode sheath is negligibly small as compared to the voltage drop across a stratified layer.

According to formula (8), the maximum electric field in striations is about $E_k \approx 250(a/r_k)$ V/cm; i.e., it changes from 20 to 200 V/cm, depending on the striation number. At a gas pressure of $p = 30$ Pa, this corresponds to reduced electric fields from 300 to 3000 Td. At the same time, in the positive column of a spherical discharge, the field $E_{\text{mon}}(r)$ in the gaps between striations does not exceed 1–3 V/cm (15–50 Td). However, it is this field that sustains a constant electron current between the striations in a spherical discharge.

In the approximation adopted, the electron flux density can be written in the form

$$j_e(r) = -n_e(r)W_e[E(r)/N] - D_e\frac{dn_e(r)}{dr} = -\frac{J_d}{4\pi e r^2}, \quad (10)$$

where $W_e(E/N)$ is the electron drift velocity, which depends on the reduced electric field, and $D_e = kT_e W_e(E/N)/eE$ is the coefficient of the longitudinal electron diffusion (here, we assume that the Einstein formula that relates the mobility to the diffusion coefficient is applicable). We integrate expression (10) assuming that, beyond narrow double layers (beyond striations), the electric field and the electron tempera-

ture (and, accordingly, the drift velocity W_e and diffusion coefficient D_e) are constant. As a result, we obtain

$$n_e(r) = n_e(a)\exp\left(-\lambda\frac{r-a}{a}\right) + \frac{J_d\lambda}{4\pi eW_e a^2}\int_a^r \frac{dr'}{r'^2}\exp\left(-\lambda\frac{r-r'}{a}\right), \quad (11)$$

where $\lambda = aW_e/D_e = eEa/kT_e$ is the parameter characterizing the ratio between the drift and diffusion components of the electron current density. At $T_e \approx 0.5$–1 eV, we have λ = 1–5. Neglecting the diffusion current in Eq. (10), we obtain that, at distances from the anode larger than a/λ, the electron density varies nearly inversely proportionally to the distance squared:

$$n_e(r) \approx \frac{J_d}{4\pi eW_e r^2}. \quad (12)$$

The space charge density at the points where the electric field is maximum is at least one order of magnitude lower than the electron and ion densities at these points:

$$\Delta n(r_k) \approx \frac{\Delta U\varepsilon_0}{e}\frac{1}{\gamma_k^2 r_k^2}. \quad (13)$$

We introduce the running Debye length

$$\lambda_D(r) = \sqrt{\frac{kT_e}{4\pi e^2 n_e(r)}}, \quad (14)$$

where the electron temperature T_e is assumed to be constant. Taking into account formula (12), we find that the electron Debye length in a spherical discharge is proportional to the distance from the anode, $\lambda_D \sim r$. This fact indirectly indicates that the width of the electric field peaks in striations (the width of the regions with a significant space charge separation) is proportional to the striation radius. For $n_e(a) \sim 10^{10}$ cm^{-3} and $T_e \sim 1$ eV, we have $\lambda_D(r)/r \sim 0.01$, which agrees in terms of order of magnitude with the observed relative width of striations.

Exponential dependence (1) of the averaged emission intensity on the radius can also be explained within the approach proposed. The signal at each point is determined by the radiation peak residing in this region because the ratio of the intensities in the neighboring minima and maxima is large and their positions depend on the current as is shown in Figs. 2–4. After normalizing to the total current, we find from Eqs. (4), (5), and (8) that

$$\langle I_d(r)\rangle = A_{\Delta v}\exp\left(-\frac{B_{\Delta v}N\gamma r}{\Delta U_0}\right).$$

With allowance for the fact that r is proportional to ρ, this expressions agrees with Eq. (1). Therefore, the coefficient α in expression (1) is a combination of the parameters related to both the mechanism for the glow excitation ($B_{\Delta v}$) and the characteristic potential drop across a striation ΔU_0 in a gas with the density N. However, to implement this dependence in practice, it is necessary to carry out additional experiments.

To conclude, a comparison between the calculated and measured distributions of the optical signal intensity in the image plane (Figs. 2–4) has shown that striations are glowing layers that are thin compared with their radii. The thickness of these layers has been estimated. It is shown that the emission intensity from a spherically stratified discharge is proportional to the discharge current.

ACKNOWLEDGMENTS

This study was supported by the International Science and Technology Center (grant no. 1425) and the Russian Foundation for Basic Research (project no. 00-03-32428a)

REFERENCES

1. L. Pekarek, Usp. Fiz. Nauk **94**, 463 (1968) [Sov. Phys. Usp. **11**, 188 (1968)].
2. A. V. Nedospasov, Usp. Fiz. Nauk **94**, 439 (1968) [Sov. Phys. Usp. **11**, 174 (1968)].
3. P. S. Landa, N. A. Miskinova, and Yu. V. Ponomarev, Usp. Fiz. Nauk **132**, 601 (1980) [Sov. Phys. Usp. **132**, 439 (1980)].
4. Yu. P. Raizer, *Gas Discharge Physics* (Nauka, Moscow, 1987; Springer-Verlag, Berlin, 1991).
5. O. A. Nerushev, S. A. Novopashin, V. V. Radchenko, and G. I. Sukhinin, Pis'ma Zh. Éksp. Teor. Fiz. **66**, 679 (1997) [JETP Lett. **66**, 711 (1997)].
6. O. A. Nerushev, S. A. Novopashin, G. I. Sukhinin, and V. V. Radchenko, Phys. Rev. E **58**, 4897 (1998).
7. O. A. Nerushev, S. A. Novopashin, V. V. Radchenko, and G. I. Sukhinin, Fiz. Plazmy **26**, 81 (2000) [Plasma Phys. Rep. **26**, 78 (2000)].
8. L. Conde and L. Leon, IEEE Trans. Plasma Sci. **27**, 80 (1999).
9. M. Strat, G. Strat, and S. Gurlui, J. Phys. D: Appl. Phys. **32**, 34 (1999).

Translated by N.N. Ustinovskiĭ